Advanced strategies for the synthesis and application of Li_3InCl_6 in solid-state lithium-ion batteries

by

Hanxin Mei

Università degli Studi di Genova

Thesis submitted in partial fulfillment of the requirements for the Degree of Doctor of Science in

Department of Chemistry and Industrial Chemistry,
Chemical Sciences and Technologies, XXXVII Cycle,

Supervisor
Prof. Paolo Piccardo (University of Genoa)

Coordinator
Prof. Renata Riva (University of Genoa)

December, 2024

Acknowledgments

The past three years have been like a dream for me. When I first came to Genoa three years ago, I was attracted by its beauty and enthusiasm. During this period, I forgot how many days and nights I spent breathing fresh air in the mountains and enjoying the warm wind by the sea. The three-year doctoral career has not only improved my research ability, but also brought me into the door of a new world.

First of all, I would like to express my deep gratitude to my supervisor, Professor Paolo Piccardo, for his help during my doctoral studies. Your genius ideas have brought a lot of help to my research work, and you have tried your best to help me solve the difficulties in the experimental process, and you have done your best to help me when I got into a research dilemma. Next, I would like to thank Phase Motion Control S.p.A. for its trust in me and full support for my research project, giving me a high degree of freedom to freely explore the mysteries of solid-state electrolytes.

At the same time, I would like to thank Roberto Spotorno for his help in impedance and other tests. I would also like to thank all the current and past members of the Metallurgical Laboratory: Alessandro, Camilla, Flavia, Francesco, Francesca, Greta, etc. You brought me into the laboratory, helped me overcome many challenges in my work, and assisted me in completing many experiments together. I would also like to thank Locardi, Marco, Giovanni and others for their help in sample characterization such as XRD and XPS. I am also very grateful to all the administrative staff and technical personnel of DCCI for solving many trivial matters in my life and environment for me, so that I can focus on research.

In addition, I would like to express my special thanks to my other friends and teammates in the badminton club for accompanying me through countless days and nights in a foreign country.

Finally, I would like to express my sincere gratitude to my family for their understanding and support, which allowed me to pursue my dreams and do what I want to do with peace of mind. Of course, I also want to thank myself for not giving up on myself in the past 28 years.

Contents

Chapter Page

Abstract

Solid-state lithium-ion batteries (SSLBs) have the advantages of high energy density and safety and are considered to be one of the most promising energy storage devices, but their marketization still faces obstacles and their practicality has also been questioned. Because most of the solid-state electrolytes (SSEs) at the core of SSLBs are very hard and cannot form a good interface contact with components such as electrodes under traditional packaging conditions, additional high pressure needs to be applied for SSLB to work properly, which limits the application of SSLB at this stage. In addition, the synthesis of SSEs is also relatively difficult, and most of the time they need to be obtained through high-energy and time-consuming solid phase methods such as sintering or ball milling.

Halide solid electrolytes are an emerging class of SSEs, among which Li_3InCl_6 (LIC) has received the most attention due to its good comprehensive performance. First, we introduced a method for synthesizing LIC by a modified mechanochemical method, aiming to reduce the synthesis time and energy consumption, thereby improving the overall synthesis efficiency of LIC SSE powder. The new method successfully reduced the synthesis time from 20 h to 8 h, and the ball milling speed only needed to be increased from 500 rpm to 700 rpm. Although the particle size of the LIC powder obtained by the new method is larger than that of previous studies, it does not affect its performance. The obtained LIC has a higher ionic conductivity than the LIC synthesized by the traditional method, which increases from 1.21 mS cm^{-1} to 1.26 mS cm^{-1}. At the same time, it has a lower electronic conductivity, which can effectively slow down the occurrence of short circuit caused by lithium dendrite growth, which is also confirmed by its better performance in symmetrical Li-Li cells. Finally, considering the importance of mechanical properties in practical applications and the fact

that no one has done similar tests before, we measured the elastic modulus and hardness of LIC powder to fill the gap in research.

Next is the application of LIC in SSB. In previous studies, LIC was still used in SSB by pressing powder into pellets, and a pressure of more than 100 MPa was required to ensure good interlayer contact during operation. This means that both the large-scale preparation and use of LIC are very difficult. To get rid of the harsh process, we used LIC, ethyl cellulose, etc. as raw materials and acetonitrile as solvent to successfully batch synthesize a self-supporting and flexible LIC-ACE SSE film through the liquid phase method. The resulting film has good flexibility and can be easily bent without breaking, and has better moisture resistance than LIC pellets. The ion conductivity of LIC-ACE film at room temperature can reach 0.76 mS cm^{-1}, and it can be stably cycled for more than 900 h in symmetrical Li-Li cells without a buffer layer. Most importantly, after being assembled into SSB, it can be cycled at a pressure of less than 1 MPa, and the capacity retention rate is still 84.8% after 50 cycles at 0.2 C. This study innovatively synthesized a flexible LIC-ACE SSE film, which greatly reduced the pressure required during operation and the difficulty of synthesis, and reduced the proportion of powder tableting steps in the SSB production process, promoting the practical application of LIC SSE.

Considering that the pressure applied by LIC-ACE in the previous study still has room for improvement, and inspired by the great contribution of polymer components in traditional composite SSE to the normal pressure working of SSB, we further introduced different proportions of PEO and lithium salt into LIC, and prepared a series of flexible composite LIC-PEO SSE films that can be used in coin cells by slurry casting. Among them, the LIC-

PEO SSE film with the best performance has an ionic conductivity of 1.19 mS cm^{-1} at 35 °C and the Li^+ transference number of 0.405. The linear sweep voltammetry test shows that its electrochemical stability window exceeds 5 V. Moreover, it has stronger flexibility and ductility than LIC-ACE, so it can work directly in the coin cell. In the symmetrical Li-Li cells test, it can work stably for more than 620 h, far exceeding pure LIC. At 35 °C, its capacity retention rate is 84.2% after 300 cycles at 0.2 C. Under the same conditions, after 150 cycles at 1.2 C, the capacity retention rate was 80.6%, and it can also perform well at higher current density. LIC-PEO SSE film combines the advantages of polymers and halides, not only showing good performance, but also easy to prepare on a large scale, so it has great application potential.

List of tables

List of figures

List of Abbreviations

Abbreviations	Full name
LIB	Lithium-Ion Battery
SIB	Sodium-Ion Battery
LCO	$LiCoO_2$
LFP	Lithium Iron Phosphate
NCM	$LiNi_{1-xy}Co_xMn_yO_2$
PbAc	Lead-Acid Battery
NiMH	Nickel-Metal Hydride Battery
SSB	Solid-State Battery
SSLB	Solid-State Lithium-Ion Battery
SSE	Solid-State Electrolyte
MOF	Metal Organic Framework
SPE	Solid Polymer Electrolyte
ESW	Electrochemical Stability Window
HSSE	Halide Solid-State Electrolyte
LEC	Li_3ErCl_6
LYbC	Li_3YbCl_6
LSC	Li_3ScCl_6
LYC	Li_3YCl_6
LYB	Li_3YBr_6
LEB	Li_3ErBr_6
LAC	$LiAlCl_4$

LLZTO	$Li_{6.5}La_3Zr_{1.5}Ta_{0.5}O_{12}$
LIC	Li_3InCl_6
LGPS	$Li_{10}GeP_2S_{12}$
LYIC	$Li_3Y_{1-x}In_xCl_6$
LYBC	$Li_3YBr_3Cl_3$
LZC	Li_2ZrCl_6
LZFC	$Li_{2.25}Zr_{0.75}Fe_{0.25}Cl_6$
SSW	Stochastic Surface Walking
LHC	Li_2HfCl_6
ITO	Indium Tin Oxides
XRD	X-Ray Diffraction
TEM	Transmission Electron Microscopy
SEM	Scanning Electron Microscope
XPS	X-Ray Photoelectron Spectroscopy
DFT	Density Functional Theory
EC	Ethylene Carbonate ($C_3H_4O_3$)
EMC	Ethyl Methyl Carbonate ($C_4H_8O_3$)
PEO	Polyethylene oxide
LIC-ACE	Li_3InCl_6-Ethyl Cellulose
LIC-PEO	Li_3InCl_6- Polyoxyethylene
TGA	Thermogravimetric Analysis
PVDF	Polyvinylidene Fluoride ($(CH_2CF_2)_n$)
NMP	N-Methyl-2-Pyrrolidone (C_5H_9NO)

CE	Coulombic Efficiency
SS	Stainless Steel
LSV	linear sweep voltammetry
LLZO	$Li_7La_3Zr_2O_2$
LATP	$Li_{1.3}Al_{0.3}Ti_{1.7}(PO_4)_3$
LLTO	$Li_{0.33}La_{0.56}TiO_3$

Chapter I: Introduction

1.1 The Development of Lithium-ion Batteries

With the rapid development of society and the progress of science and technology, the energy problem has become a huge issue that cannot be circumvented in development. Traditional fossil sources have the advantages of easy availability, stable price, and complete industrial chain, but mining and use relating to pollution caused to the environment by the medium is also a problem that cannot be ignored, and the regeneration of fossil energy is very slow. In today's era of sharply increasing energy consumption, fossil fuels may not be able to fully meet human needs[1,2].

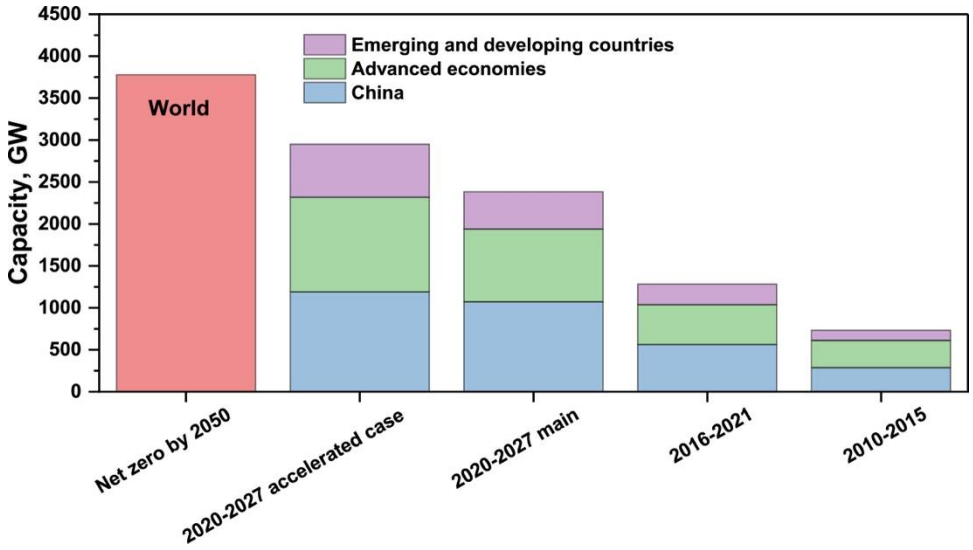

Fig. 1. 1 The renewable capacity growth in the main and accelerated cases, 2010–2050 (Reproduced with permission[3])

To protect the environment and achieve the goal of carbon neutrality, the use of clean energy is indispensable (Fig. 1.1)[4]. In addition to being produced by fossil fuels, electric energy can also be produced by renewable energy sources such as solar energy, wind energy, and tidal energy. Especially with the further market promotion of photovoltaics and wind turbines in recent years, electric energy can be regarded as clean energy[5-7]. Electricity is already an indispensable part of modern life and production. From the mobile phone, even the cars on

the highway and the ships in the ocean can gradually use electricity to drive. At this stage, new energy vehicles are undoubtedly the most attractive to ordinary people. At present, many countries have decided to stop selling fuel vehicles in the middle of the 21st century and switch to selling new energy vehicles powered by electricity[8]. At present, the most researched energy storage devices include lithium-ion batteries (LIBs), sodium-ion batteries (SIBs), etc.[9-13]. However, the performance of electrical energy storage devices is still unsatisfactory, so the research on higher performance energy storage devices has become a hot spot[14-16]. Countries in the world attach great importance to the research and development of new energy storage technologies. For example, the "DOE Project Plan" of the United States, the "NEDO Plan" of the Japanese Government, and the "Horizon Europe Framework Program" of the European Union all focus on energy storage technology.

As a chemical energy storage method, LIBs have been applied and developed relatively late (Fig. 1.2). They formally entered the commercial market in 1991, but they are regarded as the most competitive because of their lightweight, high energy power, and long life[17]. As early as 1980, John B. Goodenough's research team discovered the cathode material $LiCoO_2$ (LCO)[18]. However, due to the high cost of LCO and the problems of lithium dendrites and powdering of lithium metal used in the anode, there has been no large-scale commercialization. Next, Akira Yoshin used graphite instead of lithium metal as the anode in 1985, which fundamentally improved the cycle life problem of lithium batteries[19]. The lithium batteries at this time can be called true LIBs. With the discovery by John B. Goodenough's research team in 1996 that lithium $LiFePO_4$ (LFP) could also be used as a cathode, LIBs ushered in a stage of rapid development[9]. When nickel cobalt manganese ternary composite oxide (NCM) was discovered to be used as a cathode, which completed the last piece of the puzzle for today's commercial LIBs.

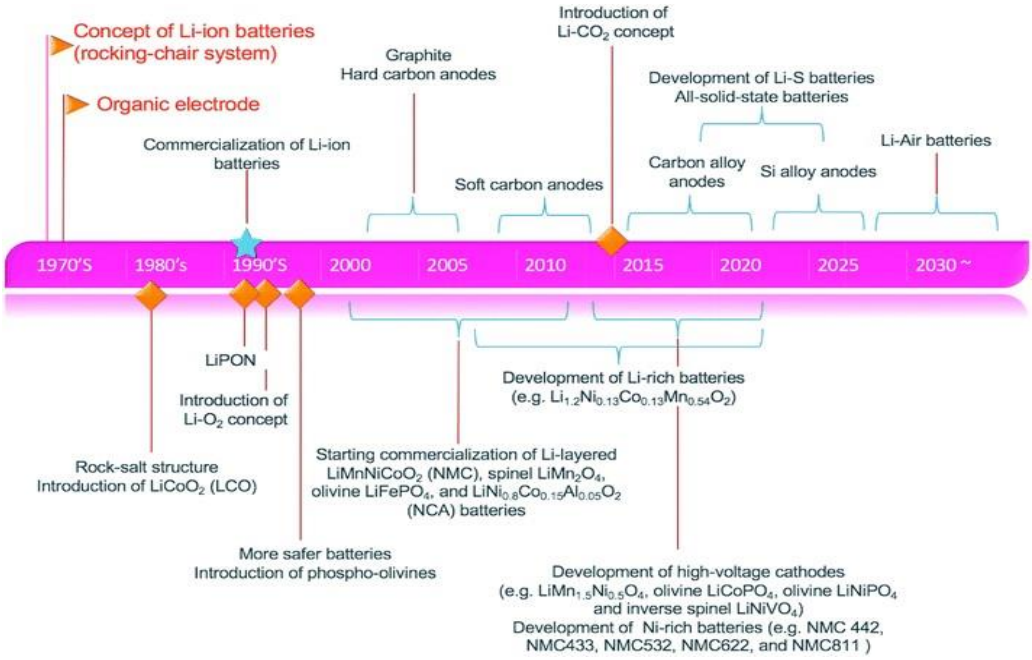

Fig. 1. 2 Historical evolution and advances of LIB technologies. (Reproduced with permission[20])

Today's commercial LIBs have developed relatively maturely. In 2023, the battery production for electric vehicles alone exceed 700GWh. However, there is still more market potential in emerging application scenarios such as energy storage power stations. Compared with traditional batteries such as lead-acid batteries (PbAc) and nickel-metal hydride batteries (NiMH), LIBs have higher energy density and environmental friendliness. Compared with fuel cells, LIBs have better universality and cost. This also means that LIBs will play a more important role in future society as the main energy storage carrier and have good development prospects.

1.2 Introduction to Solid-State Lithium-ion Batteries

1.2.1 Characteristics of Solid-State Lithium-ion Batteries

The energy density of traditional LIBs has reached a bottleneck and it is difficult to make major improvements. Therefore, it is no longer able to meet market demand under the premise of limiting costs[21]. Moreover, traditional LIBs are prone to leakage and burning of liquid electrolytes[22,23]. The porous separator is easily pierced by lithium dendrites during

the cycle and short-circuits, resulting in overheating or explosions and other safety issues[24]. This severely limits the development of LIB in terms of high safety, long cycle life, and environmentally friendly energy storage devices.

Therefore, higher energy density LIBs have become a research hotspot. As an emerging energy storage device, SSLBs using SSEs demonstrated to have an energy density far exceeding that of traditional LIB. The biggest difference between solid-state batteries (SSBs) and traditional LIBs is the use of SSEs instead of separators and liquid electrolytes.

Additionally, SSLBs also have the advantages of no electrolyte leakage, no separator, easy packaging, wide operating temperature range and electrochemical window, so they are characterized by improved safety and performance[25-27]. The mechanical strength of most SSEs exceeds the traditional separator, which avoids the use of such components and reduces production costs. Also, it can effectively inhibit the puncture of lithium dendrites during the battery operation, making it possible to use lithium metal as an anode, with high theoretical energy density. Therefore, the SSEs bring new hope for the development of high energy density and safe energy storage devices at the same time. However, the research on SSEs is still at a relatively preliminary stage. Many problems remain to be solved urgently, such as relatively low ionic conductivity, poor interface performance, and the scaling up of the production processes[28].

Since this study only focuses on LIB, all SSBs in the full text are SSLB by default.

1.2.2 Working principle and structure of Solid-State Batteries

The cathode, anode and electrolyte of SSBs are all made of solid materials and usually do not include the use of a separator, simplifying their structure compared to the traditional LIBs. In addition to conducting Li^+, the SSEs also act as a separator. So SSEs are the core components of SSBs.

The working principle of the SSB is similar to that of the traditional LIB. The structure comparison between traditional LIB and SSB is shown in Fig. 1.3[29]. When charging, the Li^+ in the cathode material is extracted from the crystal lattice and migrates to the anode through the SSEs with high ionic conductivity, while the electrons pass through the external circuit migrating towards the anode. Li^+ combines with electrons at the anode being reduced and embedded or alloyed in the electrode material. In this process, the uneven deposition of lithium could lead to the generation of lithium dendrites, which damage the structure of the battery causing capacity to reduce or short circuit. The discharge process is just the opposite, consisting of Li^+ extraction from the anode, followed by its migration to the cathode via the SSEs.

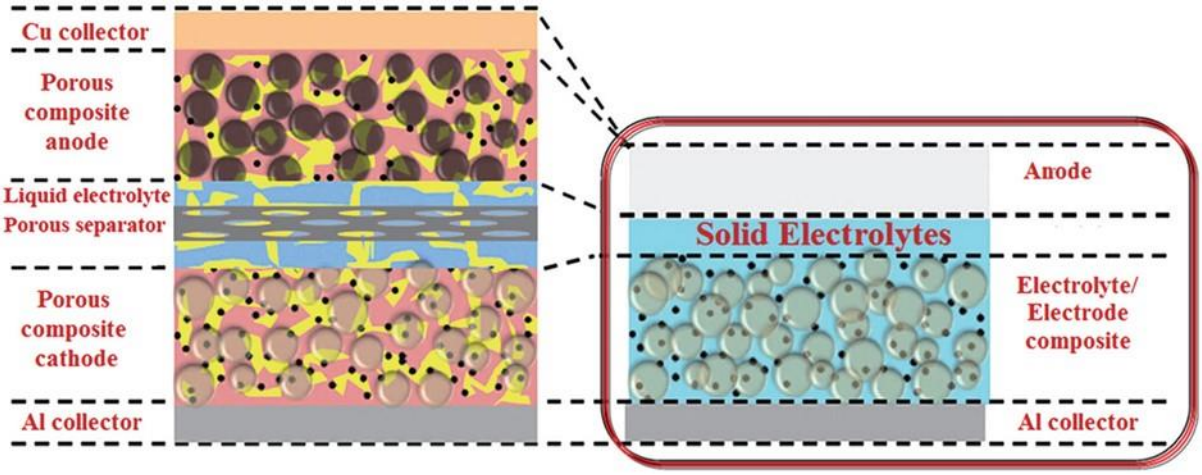

Fig. 1. 3 Schematic of the structure of SSB and traditional LIB. (Reproduced with permission[29])

1.3 Classification of Solid-State Electrolytes

SSEs can be traced back to the discovery of silver sulfide and lead fluoride by Faraday in the 19th century, which also laid the foundation for the establishment of solid-state ionics [30,31]. In the 1950s, silver-containing SSEs were already used in some special equipment, although their performance at this time was very poor, and the energy density and cycle performance could not meet commercial requirements.

Common SSEs materials are mainly divided into the following four categories: polymers, oxides, sulfides and halides, which are also materials that have received the most attention [32-39]. A lot of companies have conducted much research and investment in these materials. However, in recent years, further research on SSEs and the development of computational chemistry methods led to the discovery of many new SSEs. Among them, several compositions have attracted the attention of researchers, such as borohydride and fluorinated metal oxides [40-42]. These new SSEs are characterized by excellent properties such as high ionic conductivity and good processability. Halides and borohydrides can be prepared by simple mechanochemical methods and liquid phase methods, which enable mass production thereby making their manufacturing scalable to an industrial level. Innovative materials, such as MOF, have expanded new fields for the exploration of SSE compositions and inspired researchers to include more solutions that have been neglected in the past. It is worth discussing and studying in-depth their research potential.

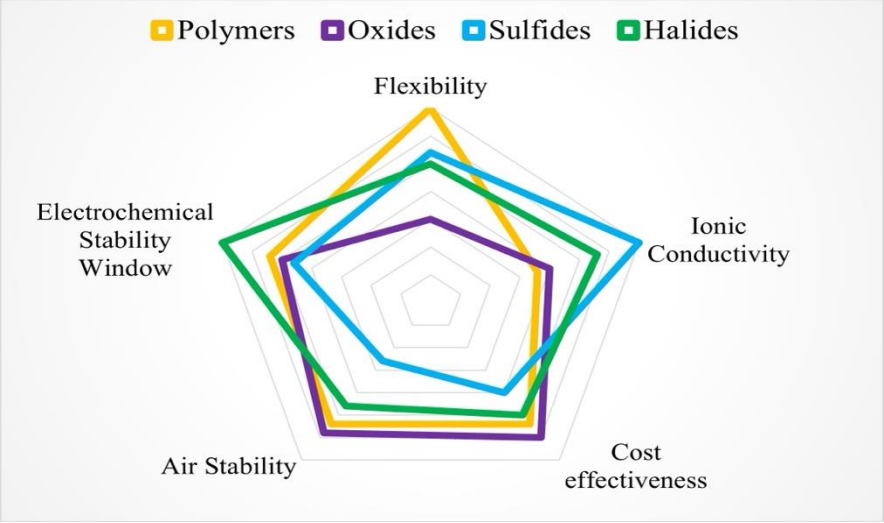

Fig. 1. 4 Radar plot comparing key properties of polymers, oxides, sulfides and halides. (Reproduced with permission[43])

Different types of SSEs also have different characteristics (Fig. 1.4). Among them, the polymer-based solid polymer electrolyte (SPE) consists of a polymer skeleton and a lithium salt that provides ionic conductivity. Since the polymer monomer contains atoms such as O and N, it can form a polymer salt with cations[44]. SPE usually has good flexibility, stable interface and easy operability. It can fit well with the electrode and operate stably without

external pressure. It can also be prepared on a large scale through solution casting method, and has the potential for industrialization. On the other hand, due to the high crystallinity of the polymer, the ionic conductivity at low temperatures is low, and it is usually necessary to work in a heated environment (over 60 °C). In addition, to improve the ionic conductivity, it is sometimes necessary to add plasticizers such as succinonitrile, which can cause side reactions, reduce the safety of the battery system, and even lead to accidents such as explosions and fires[45]. With the further progress of materials science, both SPE and composite SPE electrolytes have made great progress in the past few decades and are still the focus of research today[38].

Oxide SSEs are the most studied and have a relatively mature preparation process. Their ionic conductivity is usually higher than that of SPE, they have high chemical stability and can exist stably in the atmospheric environment, which is conducive to the large-scale production of SSB. However, its texture is hard and the interface contact with the electrode is poor. After being assembled into batteries, it needs to operate under high pressure. Current oxide SSBs usually require the addition of a small amount of liquid electrolyte to help improve interface contact and achieve better performance release. This situation is often called a quasi-solid electrolyte system[46]. The current research focus is on improving ionic conductivity and compatibility with electrodes. The main methods to improve conductivity are element substitution and heterovalent element doping. And some studies show that the ESW in the quasi-solid electrolyte system can be extended to more than 4.5V, and some can even reach 5.4V[47,48].

Sulfide SSEs have the highest conductivity, and some even exceed that of liquid electrolytes. Their texture is softer than oxides, and they can better fit the electrode materials. However, the electrochemical stability window (ESW) is narrow and cannot be matched with some electrode materials. On the other hand, it shows chemical instability to various components such as moisture and oxygen in the air, and easily produces toxic gases such as H_2S. Therefore, the entire preparation process needs to be carried out in an inert gas atmosphere, and the preparation process is relatively complicated. Moreover, the required raw materials such as Li_2S are very expensive, so the cost is relatively high. Although some shortcomings

urgently need to be improved at this stage, but sulfide, as the SSEs with the best overall performance, still attracts much attention.

It is worth mentioning that fluorinated metal oxides are also an important new type of SSE[49]. The research team led by Prof. Vito. Di Noto has made great contributions to this. Fluorinated metal oxides are mainly composed of lithium, fluorine, nitrogen, hydrogen, titanium, oxygen and other elements in a certain quantitative ratio. The principle of ionic conduction mainly comes from the efficient long-distance lithium ion migration process occurring at the interface of functionalized nanoparticles. And due to the presence of the fluorinated shell, it has good compatibility with the lithium metal anode. Sometimes fluorinated metal oxides can also be used with polymers and still maintain good electrochemical properties[50,51].

Halide solid-state electrolytes (HSSEs) are a relatively young type of SSEs that have attracted the interest of many researchers in recent years. It combines the properties of other SSEs, has balanced performance, and has a large space for cost reduction. It is also the main research object of this thesis, so a more detailed description will be presented later.

1.4 Introduction to Halide Solid-State Electrolytes

1.4.1 Synthesis of Halide Solid-State Electrolytes

Besides other SSEs, HSSEs are the most studied SSEs due to their outstanding properties. First of all, the halogen anion has only one unit of charge, which means that the ionic bond in the lithium halide molecule is weaker and the Li^+ can be dissociated and transported more easily. Most inorganic HSSEs remain stable in dry air even at high temperatures, and some of the improved HSSEs can still maintain good working conditions in atmospheric environments. At present, HSSEs can be synthesized by three methods: mechanochemical, liquid phase and solid phase. The mechanochemical method requires mixing the raw materials and then grinding them at low speed for a long time in a planetary ball milling. The strong mechanical force will create a large number of defects for ion conduction, so the HSSEs obtained by this method have the highest ionic conductivity. The liquid phase rule is

to dissolve the raw materials in a solvent, and then evaporate the solvent and dry it under vacuum to obtain HSSEs. The operation is relatively simple and the single synthesis amount is large. The solid-phase method is to obtain HSSEs by uniformly mixing the raw materials and placing them in sealed quartz ampoules and heating them to between 900-1100 °C. The ionic conductivity is low and the energy consumption is large. The conditions required by different methods and the properties of the obtained products are different (Table 1).

Table 1.1: Differences between different HSSEs synthesis methods.

Method classification	Mechanochemical	Liquid-phase	Solid-phase
Cost	High	Low	High
Performance	High	Relatively high	Low
Temperature	Medium	Medium	High
Time consuming	High	Medium	Medium
Complexity	Low	Low	Low
Production efficiency	Low	High	High
Universal applicability	High	Medium	Medium

1.4.2 Research progress of Halide Solid-State Electrolytes

Surprisingly, research on the temperature-dependent conductivity of lithium halide was conducted as early as 1930, which was also the first report on the electrical properties of this material[52]. In the 1970s, several types of emulsions with fluorite or spinel structures were discovered. However, due to the non-optimized solid-phase synthesis method, the lattice of the obtained material does not have enough defects for ion conduction, so the ionic conductivity is always lower than 10^{-4} mS cm^{-1} and these compounds did not receive much attention[53]. Although a large number of new halides with composition LiMX (M = Mg, Sc, Er, Yb, Y, In, Ga) (X = Cl, Br) and different crystal structures have been discovered since the 1990s. Li_3ErCl_6 (LEC), Li_3YbCl_6 (LYbC) and Li_3ScCl_6 (LsC) are the most typical, with

trigonal, orthorhombic, and monoclinic structure respectively (Fig. 1.5). Their ionic conductivity can reach 10^{-1}-10^{-2} mS cm^{-1} at 120 ℃, but only 10^{-5} mS cm^{-1} at room temperature, and the structure is be destroyed below to 0 ℃[54-60].

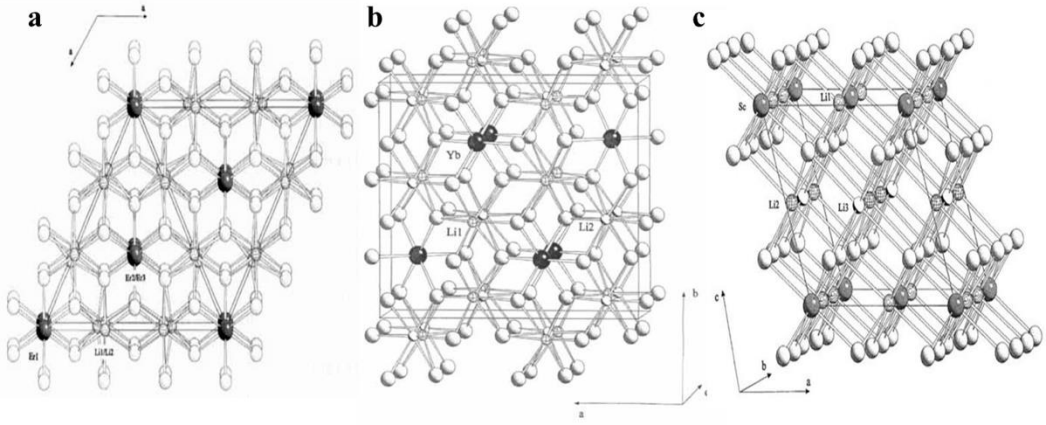

Fig. 1. 5 (a) Crystal structure of Li_3ErC1_6. (b) Crystal structure of Li_3YbC1_6. (c) Crystal structure of Li_3ScC1_6. (Reproduced with permission[57])

In recent years, Panasonic has introduced two improved halide Li_3YX_6 (X=Cl, Br) after repeated trials. The conductivity of these two materials at room temperature is higher than 0.51 and 0.72 mS cm^{-1}, The ionic conductivity of Li_3YBr_6 (LYB)after annealing can reach 1.7 mS cm^{-1}, which is significantly improved, close to the conductivity of most liquid electrolytes. And can be synthesized by a simple mechanochemical method using ball mills and then annealed at 550 ℃[61]. The final product is obtained, so the production technology requirements are low[62]. Using LCO as the cathode and In-Li alloy as the anode, the assembled battery has a discharge capacity of about 120 mAh g^{-1} after the initial cycle, the coulombic efficiency is higher than 99%, and the capacity retention rate is still 98% after 100 cycles, and ESW can be close to 4 V. This research result immediately aroused the interest of other researchers. And soon, some researchers optimized the annealing parameters and obtained LYB with an ionic conductivity of 3.31 mS cm^{-1}, which gradually pushed the properties of this material to peak[63]. Later, some researchers proved from the theoretical point of view that halides are not restricted by the design principles of solid fast ion conductors of traditional oxides, sulfides and intrinsically have a low ion migration energy barrier and good electrochemical stability (Fig. 1.6)[64,65]. It is a new research direction with great potential for the development of next-generation SSEs. Subsequently, Li_3ErBr_6 (LEB),

Li_3ErCl_6 (LEC), Li_3YbCl_6 (LYbC), and Li_xScCl_{3+x} (LSC) and other materials with similar compositions were also discovered and proved to have good ionic conductivity[66-69].

Inspired by the above research results, the metastable $LiAlCl_4$(LAC) synthesized by a simple mechanochemical method was found to have good ionic conductivity: 2.1×10^{-2} mS cm^{-1}[70]. After compressing the LAC powder, a simple symmetrical lithium battery can be directly prepared. When tested at a current density of 0.1 mA cm^{-2}, the performance remain stable for 70 cycles. Compared to the common SSEs LLZT, LAC pellets have a much higher relative density (94%) than LLZT pellets (63%). And the grain boundary resistance in LAC contributes very little to the total resistance, only 7.5% of LLZT green compacts are attributed to the grain boundary contribution. Therefore, the grain boundary resistance of LAC pellets with good contact between particles is almost negligible, which is one of the reasons for the ionic conductivity. In the study, a cheaper central metal, namely aluminum, was used, but it still has good performance, so an SSE comparable to LAC is a material worth discussing and exploring. More importantly, the LAC synthesized by this method has better performance than the conventional solid-state synthesis, which further illustrates the influence of the synthesis method and subsequent structure on the electrolyte performance.

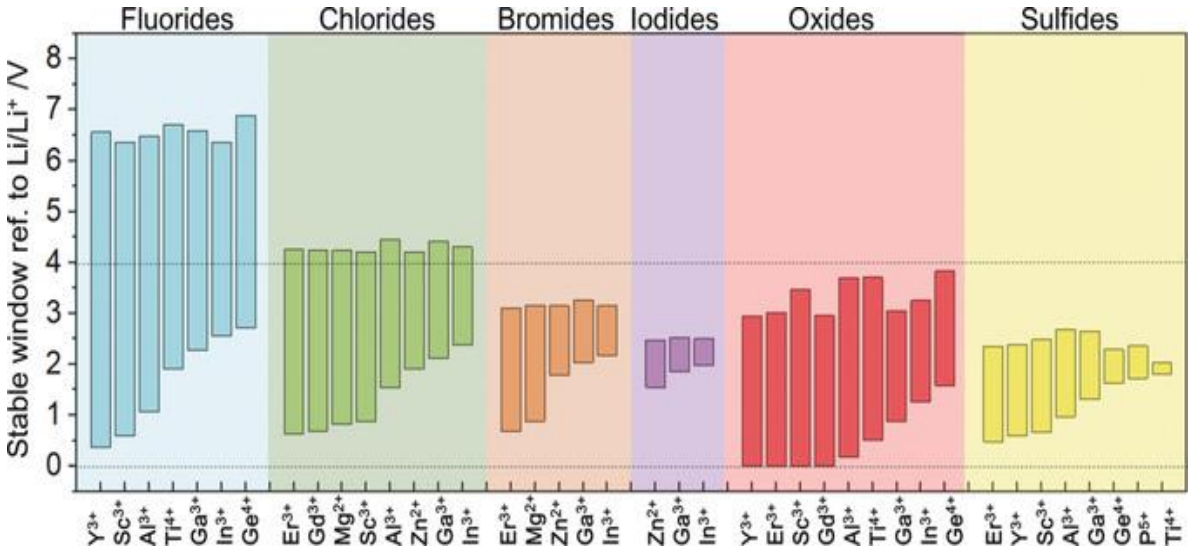

Fig. 1. 6 Calculated thermodynamics intrinsic electrochemical windows of Li–M–X ternary fluorides, chlorides, bromides, iodides, oxides, and sulfides**.** (Reproduced with permission[64])

Although the annealing temperature of 550 °C is a significant improvement compared with the annealing temperature of 1000 °C for solid oxide electrolytes, it is still relatively high[71-73]. Li et al. synthesized LIC through a mechanochemical method and an annealing process at 260 °C measuring an ionic conductivity of 0.84 mS cm^{-1} (before annealing) and 1.49 mS cm^{-1} (after annealing) at room temperature[74]. The annealed samples have clear characteristic peaks under XRD, which means that while ensuring high ionic conductivity and crystallinity, this study reduced the annealing temperature from the conventional 500 °C to 260 °C, further reducing the energy consumption. Reducing the LIC particle size to a few hundred nanometers, which is much smaller than other kinds of electrode materials, resulted in ineffective adapting to the expansion of electrode materials in the working process[75]. In addition, LIC was demonstrated to have good stability in the air, under long-term thermogravimetric analysis (TGA) measurements. The weight of LIC remained stable, and no exothermic or endothermic peaks were observed in the TGA curve. Even after being exposed to a humid environment, it can be heated to restore its performance, and the ionic conductivity of LIC after heating is in the range of 1.35-1.37 mS cm^{-1}, which is slightly lower than that of the original LIC. After that, In|LIC|LCO SSB (2.5-4.2 V vs. Li/Li^{+}) was assembled with commercial LCO and In, which showed an initial coulombic efficiency of 92% and an initial discharge capacity of 127 mAh g^{-1}. After 100 cycles, it has capacity retention of about 74.8% and has good electrochemical performance. This research further reduces the difficulty of industrial production.

On the other hand, the 50 h grinding time in the original experiment will also reduce production efficiency and increase production costs. Some researchers have prepared LYB by mechanochemical methods, reducing the grinding time to 10 h, but the ionic conductivity of the material obtained after grinding is still high, reaching 0.44 mS cm^{-1}. After annealing, it rises to 1.52 mS cm^{-1}, which is very close to the ion conductivity obtained after 50 h grinding[76]. The new grinding conditions effectively save time and reduce energy consumption.

Halides usually have strong hygroscopicity and are more sensitive to moisture, which directly increases battery packaging difficulty. In the previous studies, the relatively good stability of

LIC in air was considered one of the important properties compared with other HSSEs. Some researchers have accurately revealed that LIC first forms LIC•2H_2O in air, and then partially decomposes into $InCl_3$ and LiCl. Over time, it eventually form In_2O_3 in the air, and highly corrosive degradation products[77]. This can cause the corrosion of the aluminum current collector, which has higher requirements for the moisture control of the battery pack. The use of graphene-like carbon coated-modified aluminum foil eliminates the side reactions at the current collector interface by avoiding the direct contact between the aluminum and the LIC, SEM observations showed cracks in the bare aluminum foil, while the GLC-coated aluminum foil was still intact. Additionally, the improvement of the electrochemical performance at low temperatures of -10 °C, with enhanced Li^+ conductivity at the current collector interface was measured, thus demonstrating that interfacial modification of aluminum foil is an effective means to achieve high-performance ASSBs under all-climate conditions[78]. To improve the survival time of LIC in the atmospheric environment, some studies have shown that the powder atomic layer deposited on the surface of LIC can improve its stability in the air. For example, Al_2O_3 powder deposition can reduce the water absorption rate to 1/4 of the initial value and prolong the liquefaction time by 7 times[79].

In most research, halides are synthesized by mechanochemical methods. Although the process is relatively simple, the production efficiency is limited by the specifications of the equipment such as ball mills, and it takes a long time, requiring a long ball milling process, and consuming a lot of energy. In addition, grinding aids such as cyclohexane usually need to be added, so an additional solvent recovery step is required at the end. These shortcomings undoubtedly limit the application of mechanochemical methods in large-scale synthesis. However, the performance of the HSSEs prepared by the original solid-phase synthesis method is poor, and the performance obtained by the improved method is not up to standard and requires a very high reaction temperature, which is also not conducive to large-scale production. Therefore, the liquid phase synthesis method is widely used in other fields and has the greatest application potential. On the one hand, the structure and size of the obtained samples can be better controlled, and the performance is similar to that of mechanochemical methods. On the other hand, the scale of single synthesis is much larger than that of

mechanical synthesis, and the experimental conditions are also relatively simple, requiring only a simple inert gas or heating under vacuum conditions.

Therefore, other researchers have developed a method to synthesize LIC by a liquid phase method (Fig. 1.7). It has a high ionic conductivity of 2.04 mS cm^{-1} at 25 ℃ and has a good chemical/electrochemical stability to traditional oxide cathodes, which is of great help to actual production[80]. The SSB was prepared with In metal as the anode and $Li_{10}GeP_2S_{12}$ as the buffer layer: In|LYC+$Li_{10}GeP_2S_{12}$ (LGPS)|NCM811 (2.5-4.4 V vs Li/Li^+). In the following test, it showed 84.2% high initial coulombic efficiency, and then quickly stabilized near 100%, in addition to an initial discharge capacity of 154 mAh g^{-1}, and a capacity retention rate of 97.4% after 70 cycles. The reversible conversion between LIC and LIC·$2H_2O$ enables its intrinsic stability against air and humidity, thus ensuring high ionic conductivity is recovered after conversion[80].

Although the liquid phase method solves halide hygroscopicity, it is only suitable for LIC. The specific mechanism has not been clarified. So based on Li_3YCl_6 (LYC), some researchers have studied the relationship between the structure-ionic conductivity-humidity stability of the $Li_3Y_{1-x}In_xCl_6$ ($0 \leq x < 1$) (LYIC) SSE after the introduction of In^{3+}[81]. The research results show that with the increase of In^{3+}, LYC gradually changes from the initial hexagonal close-packed (hcp) structure to cubic close-packed (ccp) structure, and the ionic conductivity of LYIC with ccp structure can reach 1 mS cm^{-1}. Also, the moisture resistance of the LYIC can be improved by increasing the amount of In^{3+}. The higher In^{3+} content helps to form a hydrated intermediate after exposure to moisture, so that it can be dehydrated again under certain conditions to get the original[82]. The ionic conductivity of the LYIC SSE has also been restored.

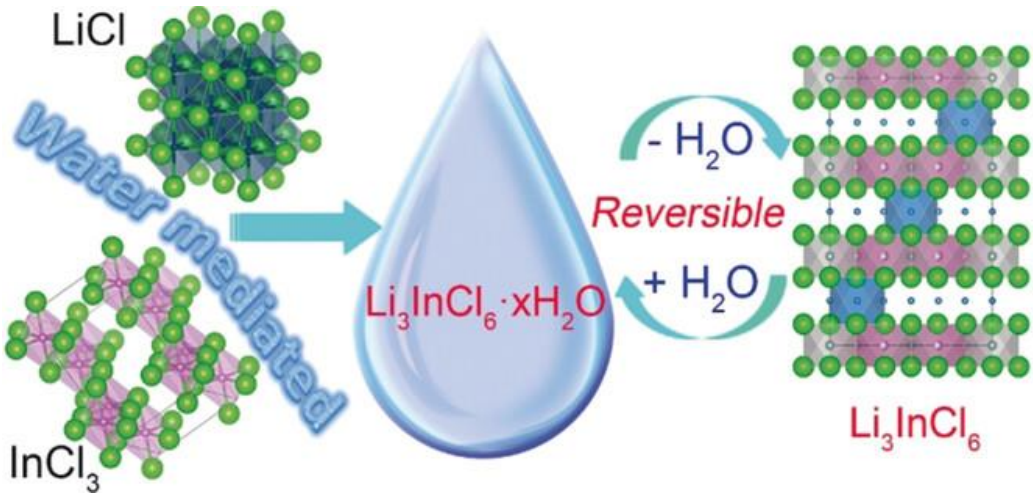

Fig. 1. 7 Process of water-mediated synthesis route for LIC SSE and the reversible interconversion between the hydrated a LIC · xH_2O and dehydrated LIC. Green Cl, purple In, blue Li. (Reproduced with permission[80])

However, initially only LIC could be synthesized by the liquid phase method, which greatly limited the application of HSSEs in research. MCl_3 (M = trivalent metal) in other HSSEs synthesis raw materials has strong hydrolysis and will react automatically to form impurities such as oxides and chlorine oxides when the solvent evaporates or even after dissolving in water. Since NH_4Cl is usually added to suppress the hydrolysis problem when synthesizing anhydrous MCl_3 in industry, the most common problem of MCl_3 hydrolysis in water is suppressed by the formation of $(NH_4)_3[MCl_6]$ intermediate. Inspired by this, NH_4Cl was also added as an auxiliary agent in the liquid phase synthesis of HSSEs. Li_3YCl_6, Li_3ScCl_6, Li_3YBr_6, and Li_3ErCl_6 can be synthesized by this method, but the temperature needs to be increased to 400 °C in the subsequent drying process to ensure the complete decomposition of $(NH_4)_3[MCl_6]$ intermediate to obtain the final product, which increases energy consumption to a certain extent. Moreover, the HSSEs synthesized by this method also change the mixed Li^+/e^- conductive interface into a pure Li^+ conductive interface, which effectively inhibits the occurrence of interfacial side reactions between HSSEs and lithium metal, and effectively alleviates the continuous reduction and degradation of halide electrolyte. But it is worth noting that this method is only applicable to most trivalent metal compounds, but is powerless for LZC, LAC, etc. This is the point that needs to be focused on next.

In the above research, the SSE material usually contains only one halogen element, so some researchers synthesized $Li_3YBr_3Cl_3$ (LYBC) with ccp structure through a combination of mechanochemistry and hot pressing (200 ℃, 44.1 MPa, 0.5 h) the ionic conductivity can reach 4.7 mS cm^{-1}[83]. After further increasing the synthesis pressure (294 MPa), its ionic conductivity is as high as 7.2 mS cm^{-1}, which is very close to the best sulfide conductivity. After that, LCO was used as the cathode and Li-In alloy was used as the anode to manufacture an SSB to verify the performance of the device. When cycled at a rate of 0.1 C at room temperature, it has an excellent discharge capacity of 124 mAh g^{-1} and coulomb efficiency of 99.7%, and still has a capacity retention rate of about 85% after 60 cycles. Although LYBC is thermodynamically unstable for high voltage cathodes[64]. However, the kinetics of LYBC oxidation seems to be quite slow, which is why it has good cycle stability.

The use of expensive center yttrium and other metals hinders their practical applicability. Although the abundance of yttrium in the crust is close to that of cobalt, since there is no large-scale industrialization, the price of the raw material YCl_3 at this stage is too high[84,85]. If the performance is not reduced too much, it is possible to use zirconium, iron, titanium, and other metal elements to replace the expensive metal, which will greatly increase the practicability of this research. Zr has a high abundance in the earth's crust and has many applications in industry[86]. Therefore, it has a complete production chain and can control the cost of raw materials at a low range.

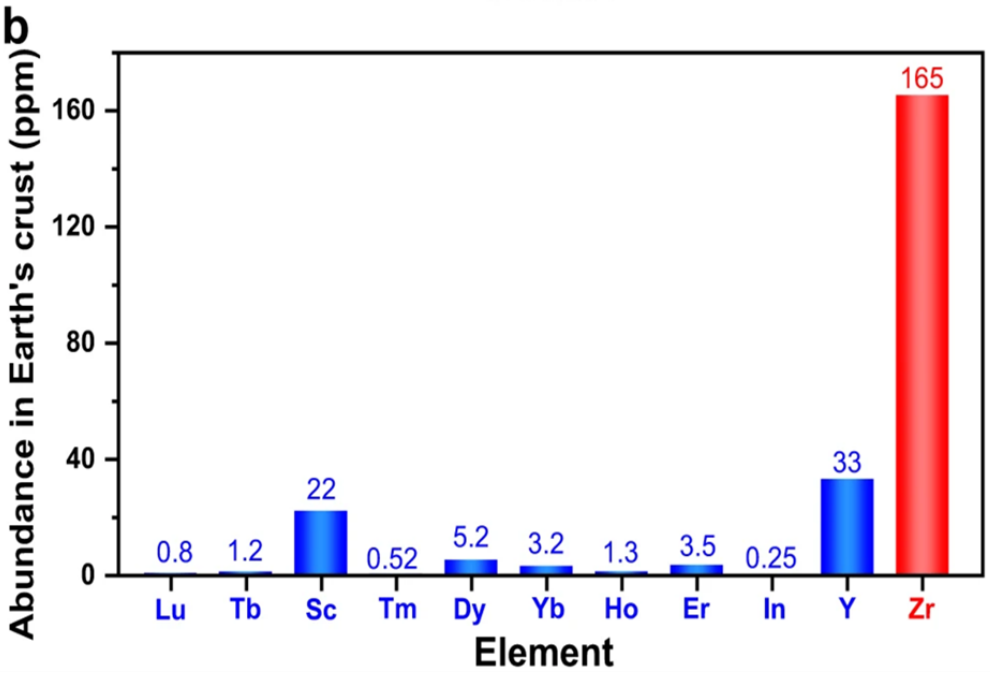

Fig. 1. 8 Abundance of the corresponding elements in Earth's crust. (Reproduced with permission[86])

The initial strategy was to prepare halides with bimetallic elements by doping cheap metals, reducing synthesis costs. $Li_{3-x}M_{1-x}Zr_xCl_6$ (M = Y, Er) is prepared, the ion conductivity is as high as 1.4 mS cm^{-1} at room temperature, and it has good stability and does not react with the cathode material[87]. In previous research, Zr was used as relatively cheap center metal in the halide, which effectively reduced the cost, but maintained high ionic conductivity and stability to the cathode material and has good performance in subsequent electrochemical tests. So, it resulted in a certain driving effect on the design and improvement of subsequent SSEs.

Subsequently, the strategy of using cheap metals has also been pursued. They did not use any rare earth and noble metals, and synthesized Li_2ZrCl_6 (LZC) HSSEs that only use Zr as the central metal[88]. The material has an hcp structure and showed ionic conductivity of 0.4 mS cm^{-1} at 30 °C and electronic conductivity of less than 5.8×10^{-7} mS cm^{-1} (Fig. 1.9a). It can be directly synthesized by mechanochemical methods, and there is no need for follow-up annealing, therefore the final SSE can be prepared only by cold pressing at 370 MPa. It is worth noting that if additional annealing is performed, the conductivity of LZC will decrease to 5.7×10^{-3} mS cm^{-1}. This may be due to its conversion to a ccp structure and higher

crystallinity after heat treatment, which enhance the strong Coulomb repulsive force between Zr^{4+} and Li^{+}, also decreasing mobile Li^{+} carrier amount or channel volume.

Due to the existence of the bimetallic synergistic effect and the increase in disorder, Fe^{3+} is introduced into LZC to form a stoichiometric composition of $Li_{2+x}Zr_{1-x}Fe_xCl_6$, It can be seen from the XRD results that as the amount of Fe increases to x = 0.25, a slight positive shift of the peak position can appear initially, but no obvious new characteristic peaks appear, which means the gradual formation of a solid solution phase (Fig. 1.9b). The slight positive shift of the peak after Fe^{3+} substitution may be because the ionic radius of Fe^{3+} (64.5 pm) is smaller than that of Zr^{4+} (72 pm). In contrast, when $x \geq 0.30$, it shows strong peaks at 30° and 32°, which is due to the presence of LiCl impurities. The $Li_{2.25}Zr_{0.75}Fe_{0.25}Cl_6$ (LZFC) showed the best performance, and ionic conductivity close to 1 mS cm^{-1}. The substitution of trivalent metals such as Cr^{3+} and V^{3+} can also improve ionic conductivity. Finally, the uncoated LCO was used as the cathode, and the In-Li alloy as the anode. The SSB was assembled using LZC and LZFC respectively achieving the electrochemical window of 4.3 V. At 0.1 C, coulombic efficiency is 90.5% and an initial discharge capacity of 162 mAh g^{-1}. Under the same conditions, the LZC battery has a coulombic efficiency of 91.4% and an initial discharge capacity of 156 mAh g^{-1}. Then, at a condition of 0.5 C, after 100 complete cycles, it still had 90.5% capacity retention, showing excellent cycle stability. After that, XPS test was used to detect the presence of some electrochemical behavior at the interface. No significant changes were observed in the spectra of Zr 3d and Cl 2p after 100 cycles, confirming that LZC was still intact. Electrochemical testing and XPS measurement together confirmed that LZC has excellent stability when combined with uncoated LCO (Fig. 1.9c). This research eliminates expensive metals and prepares halides with Zr or Zr plus Fe as the central metal, which still has high ionic conductivity and does not require annealing, but this also means that it does not have enough crystallinity. It only needs to be prepared by ball milling at 600 rpm for 10 h, effectively reducing energy consumption in the production process. In the subsequent tests of SSBs, it resulted perfectly adapted to LCO and more promising NCA materials. These tests showed that LZC and its derivatives have good practical application potential and are worthy of attention. Other groups also synthesized LZC through a mechanochemical method, but thanks to better control of reaction parameters

(500 rpm, 45 h), its ionic conductivity can reach about 0.8 mS cm^{-1} at room temperature and shows better moisture resistance[86]. After exposure to the atmosphere with a relative humidity of 5%, the properties of LZC did not change, and the conductivity did not decrease, even better than LIC which was considered the best moisture resistant material in previous reports (Fig. 1.9d)[89].

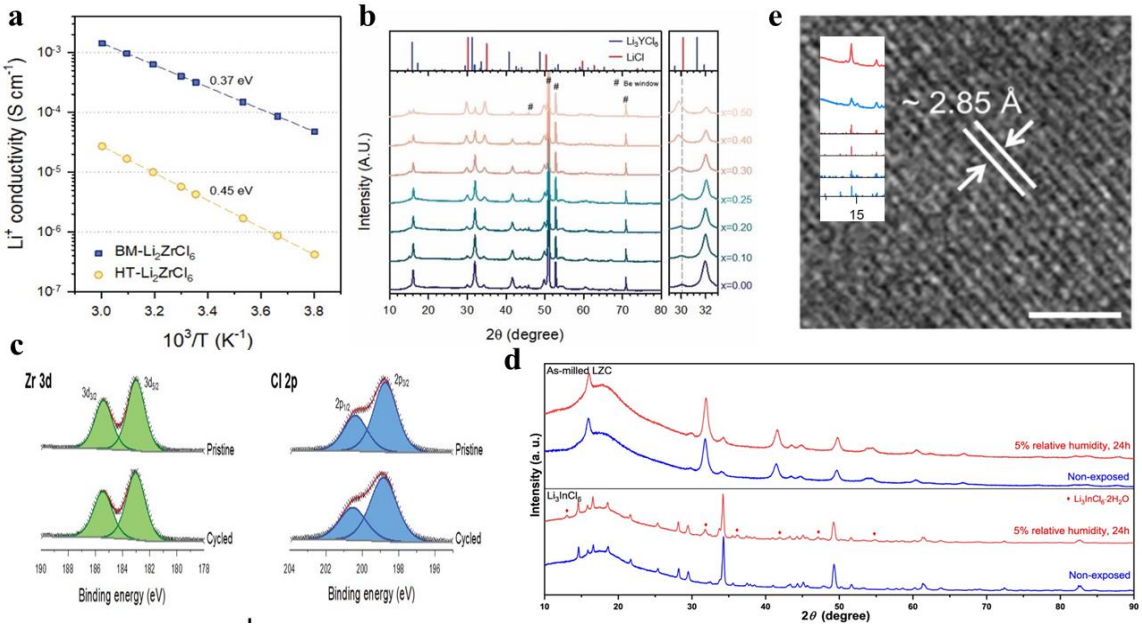

Fig. 1. 9 (a) Arrhenius plots of ionic conductivity. (b) XRD patterns for a series of $Li_{2+x}Zr_{1-x}FexCl_6$. Bragg indices for LYC and LiCl are shown at the top. (c) Zr 3d and Cl 2p for LCO electrodes using LZC for pristine powders and electrodes after 100 cycles. (Reproduced with permission[88]). (d) XRD patterns of the LZC and LIC before and after being exposed to the atmosphere with 5% relative humidity. (Reproduced with permission[86]). (e) TEM image and partial XRD pattern of LZC. (Reproduced with permission[90]) .

With the development and progress of machine learning and artificial intelligence, these technologies are gradually being used in the screening of electrolyte materials, which can significantly reduce the waste of research resources caused by conventional exhaustive methods[91,92]. Stochastic Surface Walking (SSW) global optimization combined with a global neural network potential function utilized by Li et al. simulates materials composed of Li, Zr/Hf, and Cl[90]. The potential candidates LZC and Li_2HfCl_6 (LHC) for stabilizing SSBs were synthesized, and LZC was again proved to be a suitable electrolyte. The TEM image of LZC particles shows a lattice spacing of 0.285 nm, corresponding to a crystal plane located at 14.15° in the XRD pattern, which also laterally proves the reliability of the HSSEs designed by SSW (Fig. 1.9e). The study shows that the predicted halide exhibits high ionic

conductivity and excellent compatibility with Li metal anodes without the need for an additional buffer layer to reduce side reactions at the interface. Lithium symmetric battery assembled on this basis can run for more than 4000 hours without short-circuiting. In the electrochemical test with NCM as the cathode and no additional protective layer, the capacity retention rate was still 87% after 70 cycles at 0.5 C, and the average Coulombic efficiency could reach 99.48%. It is undeniable that the newly developed machine learning strategies have shown surprising effects in the research of developing stable SSEs, especially in the rapid prediction of structures and mechanisms[93,94]. From a different perspective, similar research fields that converge and merge with this one will also play a crucial role in the future.

The halogen element in the solid halide electrolyte is usually chlorine or bromine, and there are relatively few studies on fluorine and iodine halides. However, studies have shown that SSE with fast cation conduction has two different sub-lattices. They are formed by a "rigid" sub-lattice with fixed cations and anions and a "quasi-liquid" sub-lattice with moving cations[95,96]. The concept of lattice can provide a good guide for the optimization of current electrolyte materials and the discovery of new high-performance ionic conductors[97,98]. Compounds with interstitial Li^+ or strong lithium-lithium interactions have low migration barriers, which facilitates the migration of lithium ions.

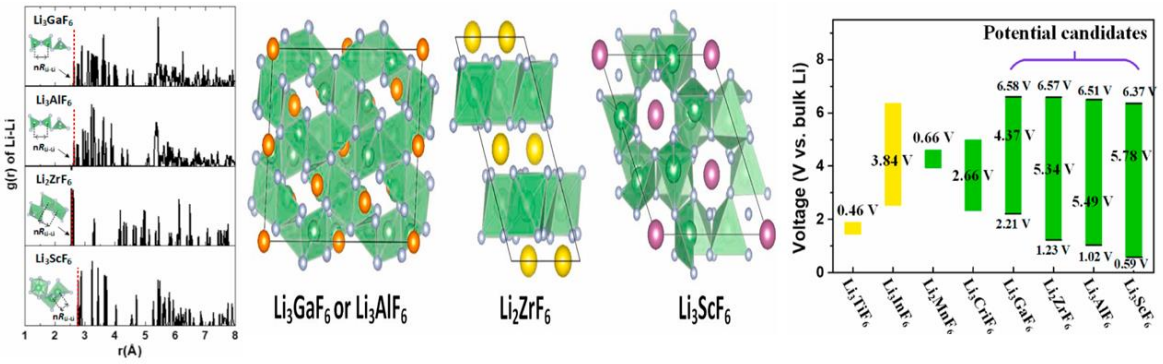

Fig. 1. 10 (a) The Li–Li RDFs in Li-ion sublattice of Li_xMF_6. (b) Crystal structure of Li_3AlF_6 or Li_3GaF_6, Li_2ZrF_6, and Li_3ScF_6 in polyhedral representation. (c) The electrochemical stability ranges of Li_xMF_6 fluoride electrolytes. (Reproduced with permission[99])

A type of fluorine-containing SSE material Li_xMF_6 (M=Al, Ga, Zr, Sc) was discovered[99]. The ion conductivity of the four fluoride electrolyte materials is around 1 mS cm^{-1}, and all have a wide electrochemical window; the smallest is Li_3GaF_6 (4.37 V), and the largest is Li_3ScF_6 (5.78 V). In addition, LiF exists in the intermediate phase of the reaction, and LiF is the best protective layer for the anode. Fluorine-based halides have also been proven to be better candidates for SSEs. Although the radius of iodine is relatively large among halogen elements, based on the results of DFT calculations, the researchers synthesized an octahedral structure Li_3MI_6 (M = La, Er) SSE material[100,101]. Its electrochemical window is wider than sulfide. The iodide crystal lattice is softer, which can improve ion transport performance, and its conductivity can reach 1.23-2.08 mS cm^{-1} and 0.39-0.65 mS cm^{-1}, which is close to most sulfides.

Some research added ionic liquids to fluorinated metal oxide SSEs and prepared composite SSEs by a simple ball milling method. Since the presence of ionic liquid components in the composite SSE ensures good interlayer contact, the assembled battery can run stably for more than 50 cycles, showing a capacity of more than 120 mAh g^{-1} when using LCO as the cathode, and also has good rate performance[102]. And Li_3AlF_6 could be synthesized by the liquid method. The ionic liquid also as an in-situ binder to bind the electrolyte particles, thereby retarding their pulverization and cracking during cycling, especially at the electrode contact interface, which is most affected by cycling. The liquid-phase synthesis of nano-scale microstructures is the biggest highlight of the research, which can ensure a sufficiently large specific surface area to achieve good grain contact, and it cannot be achieved by micro-scale structures in conventional synthesis[103]. But it is worth noticing that the test battery composed of this electrolyte needs to work at 60 °C, and a small amount of liquid electrolyte is required to improve the interfacial contact, which means that the electrolyte still has many preconditions in practical use. For the time being, it is not comparable to chlorides that work at room temperature.

Although the radius of iodine is relatively large among halogen elements, it may not be suitable as a candidate material for SSEs. Xu et al. reported some spinel-like Li_3MI_6 (M = Sc, Y and La) with a stable octahedral structure through DFT calculations[101]. Theoretical

calculation results show that Li_3LaI_6 has good performance and high ion content. The ion conductivity can reach 1.23-2.08 mS cm^{-1} at room temperature. The deformability and chemical stability are good too and electrochemical stability window indicates that Li_3MI_6 has an ionic conductivity close to that of LIC.

Previous reports have shown that Li_3ErI_6 was synthesized by combination of mechanochemical method and annealing. Only after ball milling, the ionic conductivity can reach 0.65 mS cm^{-1} at room temperature, and then annealed to improve the crystallinity, the ion conductivity decreased to 0.39 mS cm^{-1}[100]. After comparing the lattice softness of Li_3ErI_6 with the known Li_3ErCl_6, it is shown that the crystal lattice of Li_3ErI_6 is relatively soft, which can further reduce the ion migration barrier, which in turn leads to the improvement of ion transport. This study introduces a discussion range of introducing iodide into HSSEs and explains from a theoretical perspective why iodide has good ionic conductivity at room temperature. Later, more types of iodide SSEs can be synthesized by replacing the central metal and other methods, which may be a major research direction in the future. At this stage, the research on iodide and fluoride is mostly limited to theoretical calculations and preliminary synthesis stages. It is more to explore its performance through various characterizations and does not combine them with cathode materials, anode materials, etc. into ASSBs to further test its performance in actual work. So it belongs to the research blank in the field temporarily. Similar to the other halogen-doped fluorides mentioned earlier, the doped iodides may also bring surprises.

Plass et al. studied a $Li_3HoBr_{6-x}I_x$ obtained by traditional solid-phase heating[104]. During the initial doping process, higher ionic conductivity and lower activation energy were obtained as the iodine content increased because the lattice softness increased. However, the increase in cationic disorder counteracts the increase in ionic conductivity, so this is a competing process. At x = 2.93, it showed the highest ionic conductivity (2.7 mS cm^{-1} at 20 °C) and the lowest activation energy (0.21 eV). Although there are still few research on iodides and fluorides, it may be difficult to use them as practical HSSEs in pure form due to their inherent defects. They are added to other HSSEs in small amounts in the form of doping or modification, which may be a good research idea, exploiting the wide electrochemical

stability window of fluoride and the high ionic conductivity of iodide to improve the original HSSE.

Surprisingly, the solid halide electrolyte not only has good ionic conductivity, but also through experiments or theoretical calculations, it can be known that its electrochemical stability window can usually reach above 3.5 V, and some special materials can even reach the level of 5 V. Much higher than ordinary oxide or sulfide electrolytes such as LGPS (1.72-2.29 V), Li_3PS_4 (1.71-2.31 V), and LLTO (1.75-3.71 V)[64]. In addition, most of the halide SSEs can better display the theoretical capacity performance of commonly used cathode materials, such as LCO, NCM, etc., and usually have good stability and will not react with the cathode. Even if the combination of some HSSEs and the cathode is not stable, the overall performance can be improved by adding a buffer layer and other methods.

Previous studies have focused more on the electrochemical properties of HSSEs such as ionic conductivity and electrochemical stability windows. But if it is to be used in actual production, the mechanical properties of the electrolyte will also have an important impact on the overall performance of the SSB. Therefore, it is at least very important to explore the properties of the halide's shear modulus and Young's modulus through DFT calculations. Jiang et al. reported the mechanical properties of a series of SSEs and found that most chlorides and bromides have a greater shear modulus than sulfide electrolytes and a smaller Young's modulus than garnet-type SSEs (Fig. 1.10)[105-108]. This shows that it has high hardness, can effectively resist the growth of lithium dendrites, and adapt to the volume change of the electrode. At the same time, Poisson's ratio and Pugh's indicator further show that LYC and LSC have better ductility than other halide candidates, and are more conducive to forming a good interface contact with the electrode, reducing the grain boundary resistance and increasing the interaction force[109-111]. So, it has greater potential than other materials. Due to the higher thermal conductivity of bromide, this helps to reduce the occurrence of battery overheating and has higher safety.

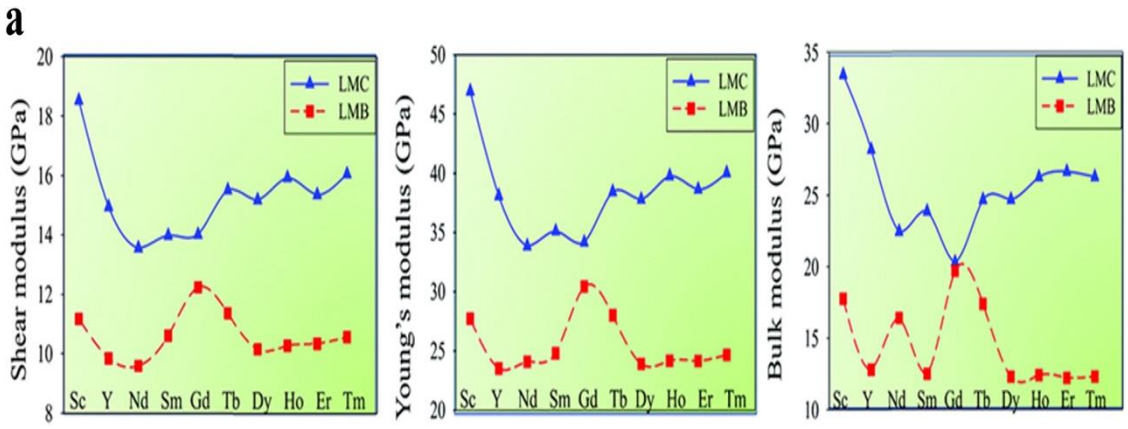

Fig. 1. 11 The shear moduli, Young's moduli and bulk of lithium chlorides and lithium bromides. (Reproduced with permission[105])

1.4.3 Application perspectives of Halide Solid-State Electrolytes

In experiments, researchers are always more concerned about the operating performance of the battery, while ignoring the impact of factors such as cost, preparation methods, and testing conditions on performance. For example, in the laboratory, the thickness of SSEs in most cases always exceeds 100 μm, while the separator thickness of commercial batteries is only 25 μm. The increase in volume and weight caused by the thickness will seriously reduce the energy density of the assembled SSBs. In subsequent tests, it is usually necessary to apply huge external pressure (exceeding MPa), which can be easily achieved in the laboratory, but is difficult to achieve in industrial mass production. Therefore, in practical applications, we always need to consider the impact of various constraints on SSBs.

Ionic conductivity is one of the core parameters of SSEs. In terms of ionic conductivity, although HSSEs cannot compete with the best-performing sulfides and liquid electrolytes, the ionic conductivity is acceptable enough due to the unique properties of SSBs. The performance indicators of some common electrolyte systems are shown in Table 2, and all data for liquid electrolytes are always based on EC:EMC=3:7 and Celgard separator.

Table 2.2: Performance and cost of SSEs compared with other types of electrolytes or electrolytes with separator.

SSE	Ionic Conductivity (mS cm^{-1}, 25 °C	Electrochemical Stability Window (V)	Estimated Cost ($ kg^{-1})
Li_3YCl_6 [64]	0.51	0.62-4.21	155.3
Li_3YBr_6 [64]	0.44-3.37	0.59-3.15	174.5
Li_3InCl_6 [112]	0.84-2.04	2.38-4.26	291.1
$Li_2Sc_{2/3}Cl_4$ [113]	1.98-3.02	0.91-4.25	535.1
Li_2ZrCl_6 [86]	0.4-0.8	1.75-4.25	21.4
$Li_3InCl_{4.8}F_{1.2}$ [114]	0.51	2.95-6.59	380.4
$Li_{0.128}[(NH_4)_{0.007}TiO_{1.98}F_{0.07}$ [49]	0.28	3.5-4.25	106.4
$Li_{0.128}[(NH_4)_{0.007}TiO_{1.98}F_{0.07}$/PEG400 [50]	0.011		
$Li_{10}GeP_2S_{12}$ [115]	10-12	1.72-2.42	755
Li_6PS_5Cl [116]	3.15-6.11	1.71-2.14	360
$Li_{0.33}La_{0.56}TiO_3$ [115]	0.2-0.63	1.75-3.71	113.6
PEO [117]	0.05-0.3	<4.0	62
$LiPF_6$	7.36-19.5	<5.1	16.5
LiFSI	9.26-18.22	<4.5	10.3
LiTFSI	7.11-18.46	<4.5	18.1

Although the SSEs relative to the liquid electrolyte conductivity is low so to reduce the internal resistance of the battery, and improve the battery's high current discharge capacity, it is necessary to make the SSE membrane as thin as possible.

The weight reduction of the battery itself is a key factor to effectively increase the energy density of SSBs. Since the density of SSEs usually exceeds that of commercial Celgard separators, to reduce the weight of the battery, requires the SSE to be as thin as possible, with the thickness controlled below 20 μm. Some research has shown that to prepare pouch cells with an energy density of 450 Wh kg^{-1}, the traditional composite cathode needs to be matched with a 10 μm SSE (oxide or sulfide) membrane to meet the requirements. And if an HSSE is used, a 50 μm SSE membrane can be used then based on the developed compact LCO cathode can achieve the same energy density (Fig 1.11)[118,119]. This means that when using HSSEs, the difficulty of the process can be effectively reduced. Lower process difficulty is also one of the advantages of HSSEs compared to oxides and sulfides, and 50 μm SSE film is expected to be achieved in the short term.

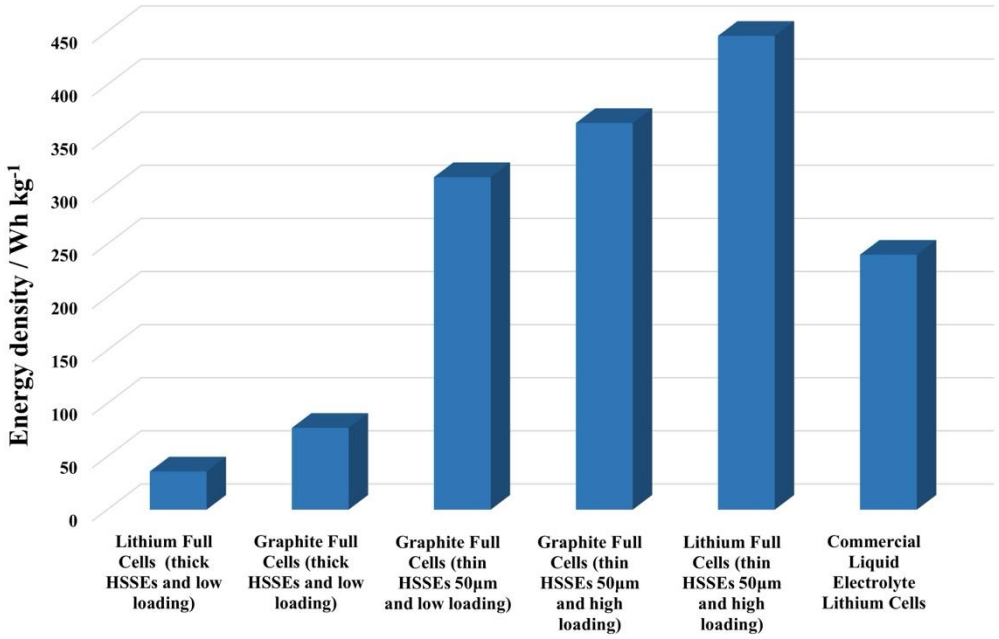

Fig. 1. 12 Calculated energy densities of SSBs and commercial battery. All half cells are under: N/P = 20. All full cells are under: N/P = 1.15, commercial LCO cathode (low loading = 3 mAh cm^{-2}, high loading = 5.5 mAh cm^{-2}), commercial graphite anode.

From the perspective of cost, we can divide halide SSEs into four types: (1) The system represented by In, Y, etc. (2) The system represented by In, Y and doped by Fe, Zr, etc. (3) The system represented by Al, Zr using only cheap metals. (4) The system represented by Eu, Ru, etc., obtained by theoretical calculation and prepared only as a verification. The first

three types are similar to the three periods of the general research process of HSSEs, and the third type is the ultimate goal. The first type usually has the best performance and most mature research but has the highest cost. The second type has medium performance and cost, and the third one is the cheapest due to the complete use of cheap metals, but their performances are comparable with those of the second type. From the industrial point of view, only the third type is suitable of application.

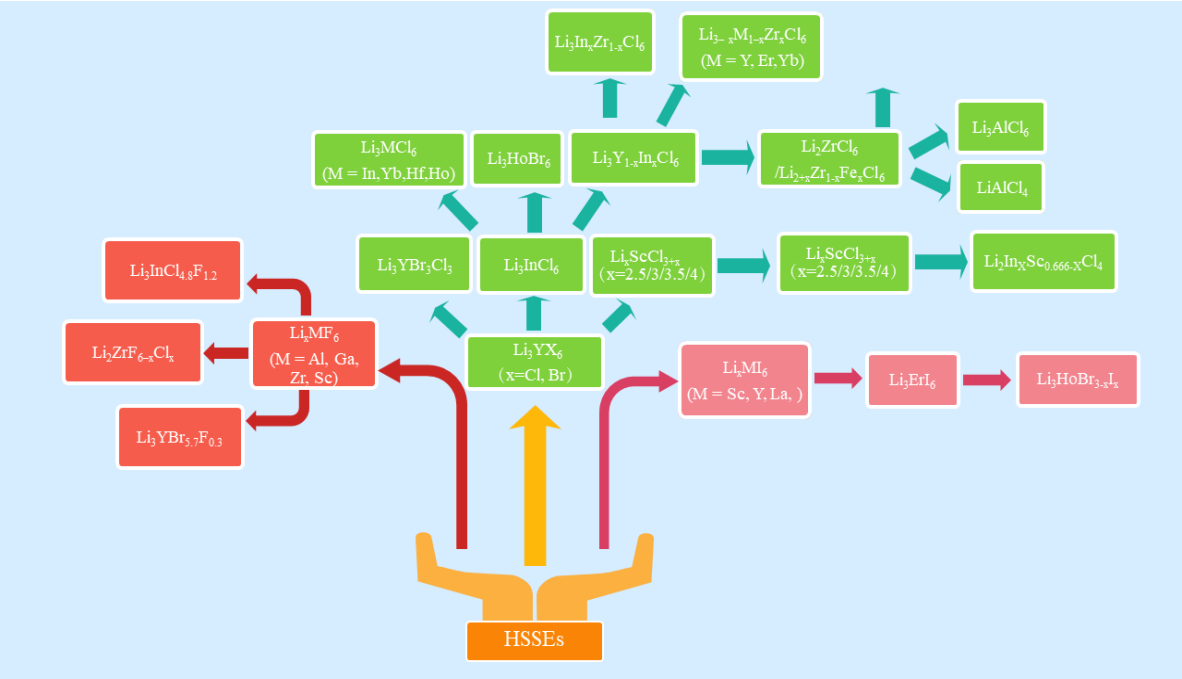

Fig. 1. 13 Dendrogram of the common HSSEs.

Taking the first type of In as an example, the abundance of In in the earth's crust is relatively low, and the current proven reserves are only about 20,000 tons[120]. Because of its light permeability and electrical conductivity, it is often used in the production of Indium Tin Oxides (ITO) and semiconductor chips, as well as in the medical field[121,122]. The price is stable at this stage, but in case it will be applied to electric vehicles, it is conceivable that the price will increase rapidly due to the scarcity of reserves. Moreover, the relative atomic mass of indium is large, which means that the mass of the battery using this element will be larger, thereby reducing the energy density. Therefore, LIC can only be used as a transitional product. The price of Zr is lower, and it is already widely used in industrial production[123,124]. The main raw material of $ZrCl_4$ can be easily prepared by widely distributed zircon. And another

major raw material of HSSEs, LiCl as a wide range of industrial products also has low price and stable supply.

The mechanochemical method has been applied to the synthesis of HSSEs. The raw materials are subjected to long-term high-speed grinding in a planetary ball mill. Due to the large number of lattice defects, the ionic conductivity has also been improved. The initial research started with high-cost Li_3YCl_6 and Li_3YBr_6, which are Li_3ErCl_6 and Li_3ErBr_6 isomorphs, but belong to the cubic crystal system, which may also be the reason for the high ionic conductivity. Subsequently, they were gradually extended to other elements such as Li_3ScCl_6 and LIC. Meanwhile, HSSEs with low-cost center metals such as Li_2ZrCl_6, $Li_3Fe_xZr_yCl_6$, and $LiAlCl_4$ have also received more attention. The cost problems caused by the use of expensive metals are gradually reduced. During this period, the experimental parameters of the mechanochemical method were further optimized, but it was still limited by the single synthesis scale and could not develop further. When the liquid-phase method was found to be capable of synthesizing some HSSEs such as LIC and achieving similar performance to the mechanochemical method, the possibility of mass production was realized. The higher the electronegativity of the contained halogen, the wider the electrochemical window and the lower the ionic conductivity. Therefore, achieving the ultimate performance of chloride HSSEs by high-cost metal systems represented by LIC and using low-cost metals represented by Li_2ZrCl_6 to promote industrialization are the most concerned research directions at this stage.

1.5 Motivation and Approaches of Current Thesis

Due to the unstable supply of fossil fuels caused by the war, the technology of using renewable energy sources such as solar energy to produce and store electricity has become the center of public attention. However, electricity cannot be stored in warehouses, and methods such as pumped storage power stations are limited by environmental factors. It cannot be used on a large scale, so batteries are the most suitable energy storage medium. On the other hand, the electrification trend of automobiles has further promoted the development of batteries. As the best choice at this stage, LIBs have naturally received the most attention.

However, the safety and energy density of traditional LIBs have been unable to meet demand. Therefore, solid-state LIBs with higher safety and energy density have become the most popular research direction nowadays.

HSSEs have good performance and cost-effectiveness, and because they are the latest type of SSE, there are still many blank areas waiting to be explored, with good market prospects and research potential. This study mainly focuses on the synthesis of HSSEs and their practical application in SSBs. The research content of this doctoral thesis can be divided into three chapters, which are briefly described as follows:

(1) Improvements in the mechanochemistry synthesis of LIC

In most cases, the mechanical synthesis of HSSEs always requires long-term ball milling (more than 20 h), and additionally requires time-consuming cooling during the ball milling process, as well as the process of separating the products and ball-milling balls. This reduces synthesis efficiency and significantly increases energy consumption. LIC synthesis is also lengthy, with the most common ball milling procedure taking 20 h. To improve the synthesis efficiency of LIC, we optimized the synthesis procedure of LIC by controlling parameters such as ball milling time and ball milling speed. We saved 60% of the time by slightly increasing the ball milling speed, and shortened the synthesis time of LIC to less than 10 h for the first time. The obtained LIC has high ionic conductivity, low electronic conductivity, relatively small average particle size, and the overall performance is still good, even exceeding the performance of the product after long-term ball milling in traditional procedures. This study successfully shortened the ball milling time in LIC synthesis, improved the synthesis efficiency, and maintained the high performance of the product, allowing researchers to focus more on exploring the properties of LIC instead of being limited to cumbersome synthesis, which greatly promoted the follow-up research of LIC.

(2) Preparation of flexible LIC-ACE SSE film by solution casting method

Since most SSEs test require the use of pellets, which must be prepared by at least three powder pressings, the process is lengthy and difficult to manage. Inspired by the electrode slurry and liquid phase deposition methods, we have improved the solution casting method by mixing LIC, binder, solvent and other components into a slurry and pouring it onto the surface of the filter membrane to produce LIC-ACE films. The resulting samples can be easily peeled from the filter membrane with tweezers, do not break when bent, and show good resistance to humidity. They also have a high lithium ion conductivity at room temperature and show good electrochemical performance in symmetrical cells and SSBs. It is worth noting that in addition to operating under high external pressure like traditional SSEs, LIC-ACE film can also operate in coin cells. In this study, high-performance LIC-ACE films were fabricated by an improved solution casting method that eliminates the need to press the LIC powder, greatly reducing the time-consuming manufacturing of pellets, eliminating the limitations imposed by the compressed surface, and further promoting the practical development of HSSEs.

(3) Application of LIC-PEO composite SSE film in SSB

Based on previous research on SPEs and HSSEs, we were inspired by the research on composite electrolytes and tried to combine LIC with PEO, successfully preparing a high-performance polymer HSSE. And it can be prepared by two methods: liquid phase method and solid phase method. The entire preparation process of the liquid phase method is based on the solution casting method, using acetonitrile as the solvent and $LiPF_6$ as an additional electrolyte additive, cast the mixed solution on a PTFE plate and dry it to obtain LIC-PEO film. The solid phase rule requires that PEO and other components are uniformly mixed and ground at about 50°C. Finally, LIC-PEO film is produced by hot-pressing or thermal-extrusion.

The obtained LIC-PEO film has good flexibility, can withstand repeated bending by tweezers, and has high ionic conductivity and shows good electrochemical performance in coin cells

at 35 °C. The moisture resistance is also significantly improved compared to LIC. The composite electrolyte of HSSEs and SPEs has never been mentioned by researchers, and it is a new research direction with good research prospects.

Chapter II: Advanced Strategies for High-Performance Halide Solid-State Electrolyte Synthesis using Improved Mechanochemical Methods

2.1 Introduction

HSSEs have attracted the attention of many researchers due to their high ionic conductivity and wide ESW. Theoretical analysis also proves that HSSEs have excellent interfacial stability for high-voltage cathode materials such as $LiCoPO_4$ (4.8 V). And there is no need to undergo high-temperature sintering like oxide SSEs to exhibit high ionic conductivity. In most cases, it can be applied through simple cold pressing. However, large-scale preparation of HSSEs is always difficult. Through a combination of experimental and theoretical analysis, it can be seen that the number of defects determines the ionic conductivity of HSSEs to a large extent[125]. Therefore, simply mixing raw materials and heating them in quartz ampoules cannot obtain the ideal product. This is why until 2018, high-performance HSSEs have only returned to the attention of researchers after they were synthesized through mechanochemical methods[125]. Continuous mechanical force can generate a large number of structural defects, so HSSEs are always synthesized in planetary ball mills via lengthy and energy-consuming mechanochemical methods, sometimes this process can also lead to the formation of core-shell nanoparticles, but this was not observed in this study or in previous research[126-129]. On the other hand, since most halides used as raw materials easily react with moisture in the air, the synthesis must be in a state of isolation from the air[77,130]. Moreover, in synergy with grinding aids, stainless steel jars will be corroded[131]. Therefore, zirconia jars and balls with good sealing function and can be filled with inert gas are indispensable, which also increases the production cost[132]. Therefore, although the synthesis principle of mechanochemistry is very simple, and no real-time monitoring is required during the synthesis process, the production efficiency is always questioned by researchers due to the extremely long synthesis time. Therefore, how to shorten the ball milling time is an urgent problem to be solved.

Compared with other HSSEs, LIC has relatively stable properties and can remain stable in dry air, and has good electrochemical properties, higher ionic conductivity, and relatively easy availability of synthetic raw materials. In addition, it has the strongest instability towards

metallic lithium anode, which also means that as long as the improved strategy can make LIC stable towards lithium, it can be easily extended to other HSSEs, so LIC is the most popular research object[112]. Although LIC can be synthesized by the liquid phase method, but the ionic conductivity is about 10% lower than that obtained by the mechanochemical method. Therefore, in some studies, to obtain the most extreme data, the mechanochemical method is usually used to prepare LIC. In this study, we mainly used LIC as the research object to measure the impact of different conditions on the synthesis.

In most reports, it is always necessary to place the raw materials and grinding aids in a planetary ball mill, add grinding balls that exceed the weight of the raw materials dozens of times, and finally grind at about 500 rpm for more than some days to obtain the final product. Although as the research progressed, the grinding time was reduced from the initial more than 40 h to about 20 h[61,63,76]. However, considering the additional time required to cool down for 5-10 minutes every 15 minutes of grinding. Moreover, it takes a long time to separate the tiny grinding balls from the product and collect the powder adhering to them, which is a tedious step[133]. The overall time-consuming is still too long. While this affects synthesis efficiency, it is also not conducive to energy saving. In this work, we take LIC as the research objects, and strive to ensure that the products have high performance while reducing ball milling time and improving synthesis efficiency, provides new ideas and support for large-scale preparation of HSSEs. Since many factors affect ball milling, such as ball milling time, ball milling speed, ball milling ball size, jar filling rate, grinding aids, etc. So this study based on our previous research, mainly considers the impact of ball milling time and speed on LIC synthesis. Finally, high-performance LIC was successfully synthesized at a ball milling speed of 700 rpm and a ball milling time of 8 h, which greatly shortened the synthesis time. Finally, consider the expansion of SSEs due to the repeated shuttling of lithium ions during the charge and discharge process and long-term cycling, as well as the possible penetration of SSEs after the formation of lithium dendrites[134-136]. Therefore, the mechanical properties of SSEs are very important, so we also tested the elastic modulus and hardness of LIC.

2.2 Experimental Section

2.2.1 Synthesis of Li_3InCl_6

To test the performance of LIC under different synthesis conditions, the raw materials were ball milled under different conditions. Stoichiometrically weigh anhydrous lithium chloride (LiCl, Innochem, 99.99%) and anhydrous indium chloride ($InCl_3$, Sigma-Aldrich, 98%) and grind in an agate mortar and pestle for 10 minutes. After grinding, the mixture was transferred to a grinding jar (50 ml) and sealed. Grinding aid is cyclohexane. The entire process was performed in an argon-filled glove box.

This was followed by ball milling for several hours using Retsch (Emax) planetary ball mill under different conditions of ball milling speed. To ensure that the temperature does not exceed the standard, every 15 minutes of ball milling, stop cooling for 10 minutes, this cycle until the end of ball milling. After the ball milling process is completed, open the ball milling jar in an inert atmosphere and heat it at 50 °C until the cyclohexane is completely volatilized. Then, sieve all the components and remove the grinding balls. Collect all the powder and grind it manually for 10 minutes and store it for later use. Different samples are named separately according to the time taken and ball milling speed.

2.2.2 Characterization methods

The microscopic morphology and structure of the samples were observed by scanning electron microscopy and the elemental distribution was determined by energy dispersive spectroscopy. Ion conductivity, Electrochemical Impedance Spectroscopy (EIS), Cyclic Voltammetry (CV), charge/discharge tests were performed on Biologic VSP Potentiostat (France, Grenoble) and NEWARE BT4008 (China, Shenzhen). The morphology is visualized with a scanning electron microscope (SEM) **(**Germany, Zeiss**)**. The crystal structure was determined by X-ray diffraction (XRD) using Rigaku MiniFlex X-ray diffractometer with Cu Kα radiation (λ = 1.54178 Å) (Japan, Tokyo). The elastic modulus and hardness were measured by the Nanotest Xtreme nanoindenter (UK, Wrexham) equipped

with a Berkovich tip under the low loads testing regime using continuous stiffness measurement. Particle size distribution was measured by Microtrac S3500 laser particle size analyzer (USA, Pennsylvania). Information such as binding energy was collected using Al Ka source X-ray photoelectron spectroscopy (XPS) at 15 kV and 20 mA by PHI 5800 workstation (USA, Minneapolis).

2.2.3 Electrochemical performance measurement

The ionic conductivity was measured by EIS using SSEs pellet by constructing SS (stainless steel)|LIC|SS test bench, and the pressure of 294 MPa was applied during measurement. Test frequency range between 100 mHz and 1 MHz with an amplitude of 20 mV. Electronic conductivity was measured by DC polarization method at room temperature at a constant voltage of 2 V for 2000 s. The thickness of the lithium metal anode used in Li-Li symmetric cell is 200 μm. If not mentioned specifically, all tests are performed at 25°C by default. The electronic conductivity and ionic conductivity of the electrolytes were calculated by the following equation:

$$\sigma = \frac{L}{R \times S}$$

where R, L and S represents the resistance, the thickness of electrolyte pellet and the area of blocking electrode, respectively.

The activation energy (Ea) was computed by fitting the calculated diffusion coefficients to the standard Arrhenius form using the following equation[137,138]:

$$D = D_0 \exp\left(-\frac{E_a}{RT}\right)$$

2.3 Results and Discussion

2.3.1 Effect of ball milling times on Li_3InCl_6 performance

Ball milling is a method of grinding and synthesizing materials through mechanical force. During the ball milling process, due to the action of mechanical force, the material undergoes varying degrees of deformation, fracture, and rearrangement, thereby affecting its crystal structure and physical properties. Past reports have proven that the grinding time, weight and rotation speed of the grinding balls have a great impact on the production and performance of the final product. To reduce grinding time and improve production efficiency, we improved the existing synthesis procedure through a series of experiments with controlled variables.

First, we synthesized sample through the most common standard grinding procedure (LiCl: $InCl_3$ is 3:1 in molar ratio) and named LIC-S. The synthesis conditions are ball milling for 20 h, rotation speed 500 rpm, mass ratio of the grinding balls to the raw material is 40:1. The optical photo of the product appears as a white solid powder, and the oxidized contamination products are usually light yellow (Fig 2.1a). SEM images show that its microscopic morphology is smooth spheres, and most of the particles are about 1-2 μm in size (Fig 2.1b). The particle size distribution test also supports this view, which means that the average particle size D_{50} is 1.32 μm, while D_{90} is 3.11 μm, which means that 90% of the particles are smaller than 3.11 μm, indicating that the sample does not contain too many large particles (Fig 2.1c). At the same time, there are also a small number of particles with a particle size smaller than 0.5 μm, accounting for no more than 6%. The XRD pattern shows its good purity and appears as a standard monoclinic rock-salt structure ($C_{2/m}$) (Figure Annex 2.1). Thanks to the precise weighing, almost no residues of $InCl_3$ and LiCl can be found in the LIC synthesized under these conditions. The crystal structure of LIC and the corresponding $InCl^{3-}$ octahedral coordination are shown in Figure A 2.2.

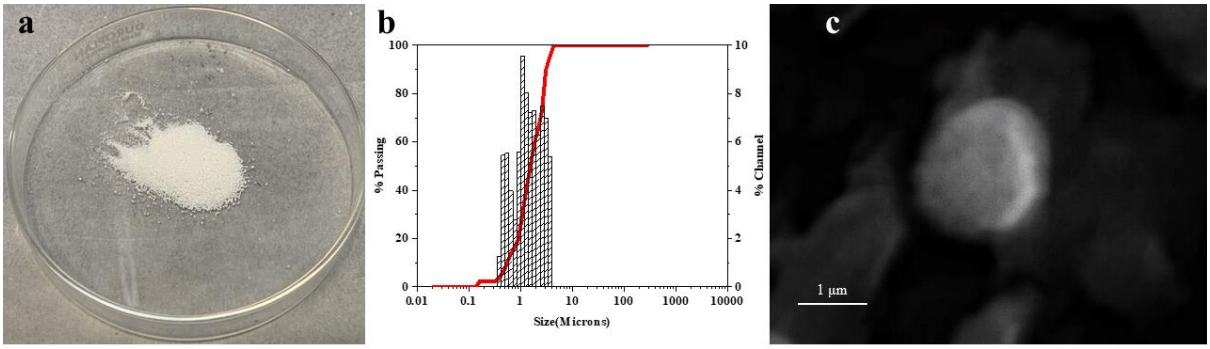

Fig. 2. 1 (a) Digital photos of LIC-S. (b) Particle size distribution plot of LIC-S. (c) SEM image of LIC-S.

The measured ionic conductivity after the pellet was made was 1.21 mS cm^{-1} (Fig. 2.2a) and exceeded the average level reported in the past (Table A2.1). The electronic conductivity is 2.9×10^{-6} mS cm^{-1} and the activation energy is 0.31 eV (Fig. 2.2b,c). SSEs need to be ionic insulators in theory, but in actual tests they still show very low electronic conductivity. If the electronic conductivity is high, short circuits will easily occur and the formation of lithium dendrites will be promoted. Low activation energy means that the migration barrier of ions is low, so it is easier for them to move between SSE and electrode. And improve performance at high current densities. Low activation energy also helps to improve the stability of SSE during temperature changes[139-141].

Since unmodified LIC has poor compatibility with lithium metal when current is applied, a buffer layer is usually required to delay the occurrence of side reactions in electrochemical tests. When LIC contains more impurities, side reactions are usually more severe. In this case, lithium symmetrical cell without a buffer layer can run for 50 h before short circuit at a current density of 0.1 mA cm^{-2} (Fig. 2.2d). The part circled in red represents a short circuit (Fig. 2.2e). Therefore, it can be considered that the performance of this sample is good, and used as a standard sample for comparison with the subsequently synthesized sample. Ionic conductivity is one of the most important parameters of SSEs and therefore serves as the main measure of product performance in subsequent experiments. SEM is used to explore the microstructure and size of the product. XRD is used to confirm the presence of impurities and changes in their LIC crystallinity. There is no consensus in the academic community on the impact of crystallinity on LIC performance, but generally speaking, as the crystallinity increases, the ionic conductivity will also increase.

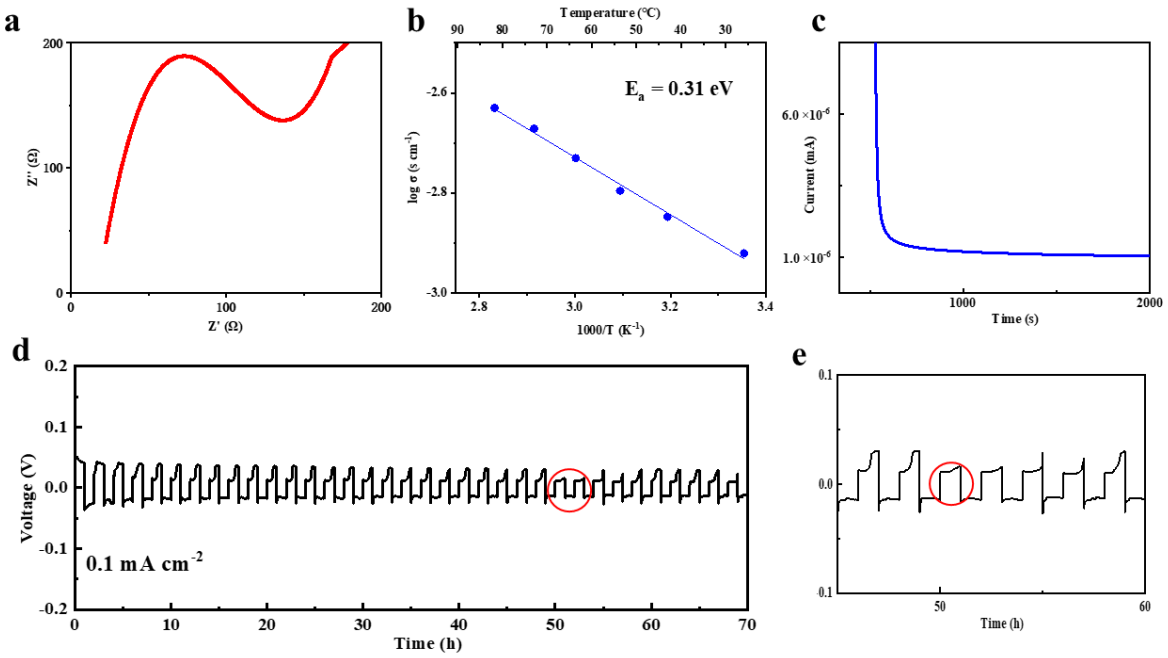

Fig. 2. 2 (a) EIS plots of LIC-S at 25℃. (b) Arrhenius plot of LIC-S. (c) Polarization current–time curve of LIC-S with an applied external voltage of 2 V. (d) Galvanostatic stripping/plating voltage profiles of symmetric Li |LIC-S| Li cell during cycling. (e) Amplified voltage profiles at 45-60 h.

The raw materials were manually ground for 1 h using a grinding pestle in an agate mortar, ensuring uniform stress on the raw materials during the entire process. After observing its microstructure in SEM, comparing the raw materials before grinding, it can be found that the particle size distribution range is very wide, there is no regularity, and there is a certain degree of agglomeration, which is consistent with the characteristics of low-energy grinding (Fig. 2.3a). This is understandable because the mechanical force exerted by hand grinding is not sufficient to rearrange the material. The XRD results can also prove this, no characteristic peaks belonging to LIC can be found in the pattern, but the characteristic peaks of $InCl_3$ and LiCl can be easily found, such as 21.4°, 24.4° and 31.9° etc (Fig. 2.3b).[142,143]. The standard pattern for $InCl_3$ and LiCl is shown in Figure A2.3. The ionic conductivity measured after the pellet was made was less than 1×10^{-3} mS cm^{-1} (Fig. 2.3c). These tests collectively demonstrated that LIC not be synthesized. At this time, the product is still a mixture of $InCl_3$ and LiCl.

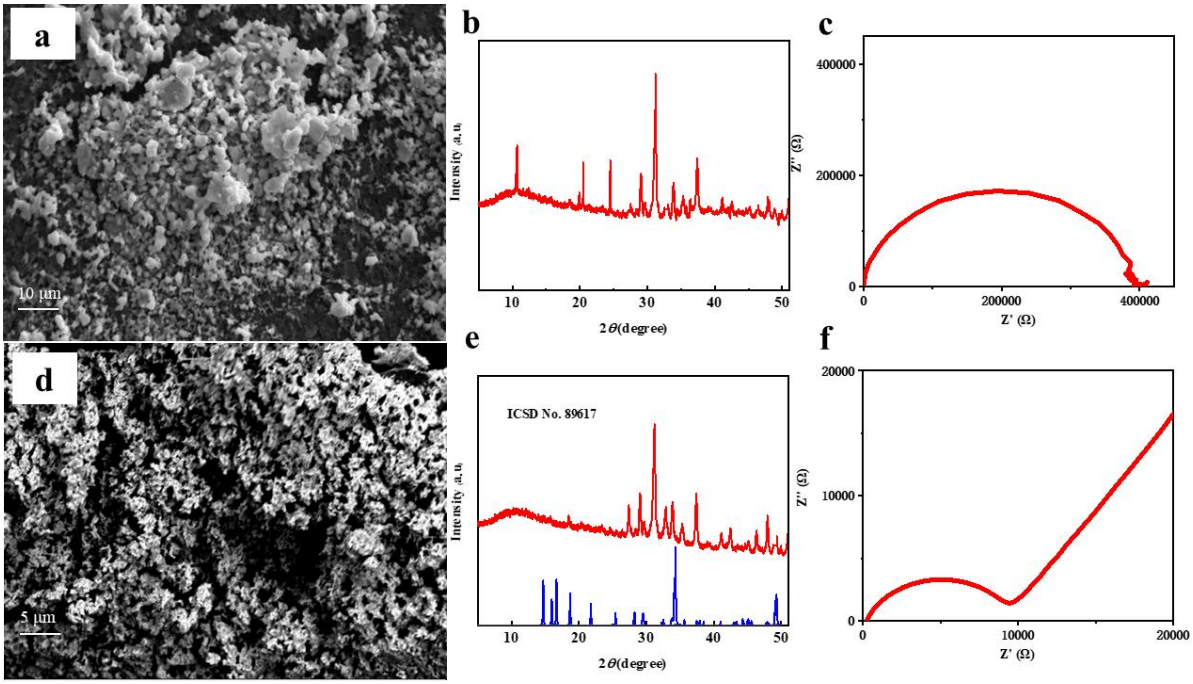

Fig. 2. 3 (a) SEM image of after manually grind. (b) XRD pattern of after manually grind. (c) EIS plots of after manually grind at 25 ℃. (d) SEM image of after 1 h ball milling. (e) XRD pattern of after 1 h ball milling. (f) EIS plots of after 1 h ball milling at 25 ℃.

Afterward, the same raw materials will be ball milled in a planetary ball mill using standard procedures for 1 h (500 rpm, 40:1) and then various tests will be conducted again. The SEM image has changed compared with the previous, the particle morphology becomes very complex, there is no obvious morphology, it is more like a transition phase existing in the phase change process. The XRD results also confirmed this, and the generation of some new characteristic peaks proves the changes brought about by the ball milling process (Fig. 2.3d). Compare with LIC standard pattern (ICSD No. 89167), the characteristic peaks of LIC can be found in the pattern, but the intensity is very weak, and $InCl_3$ and LiCl still occupy the main phases, also found some intermediate products such as $LiInCl_4$ (Fig. 2.3e)[144]. The ionic conductivity measured after making the pellets are around 1×10^{-2} mS cm^{-1} (Fig. 2.3f).

The raw materials were then ground under standard procedures for 4, 8, 12, and 16 h, respectively called LIC-4, 8, 12, and 16. From the results of the XRD pattern, they are very different from those after grinding for 1 h, and new characteristic peaks are being generated. There is a strong connection between the patterns of different products, the characteristic peaks have changed, and there is a gradual evolution process (Fig. 2.4a). Some typical

characteristic peaks are marked in yellow. As grinding time increases, the intensity of the characteristic peak representing LIC gradually increases, and its peak shape also becomes sharper. However, although the intensity of the characteristic peaks representing $InCl_3$ and LiCl has significantly weakened, they still exist in large amounts. This indicates that these samples still are a mixed phase of LIC, $InCl_3$ and LiCl, this can seriously reduce the electrochemical performance of the sample. The ionic conductivities of different samples are still very low, respectively 0.1, 0.16, 0.23 and 0.41 mS cm^{-1}, which further proves the existence of a large number of non-LIC components in the mixed phase (Fig. 2.4b).

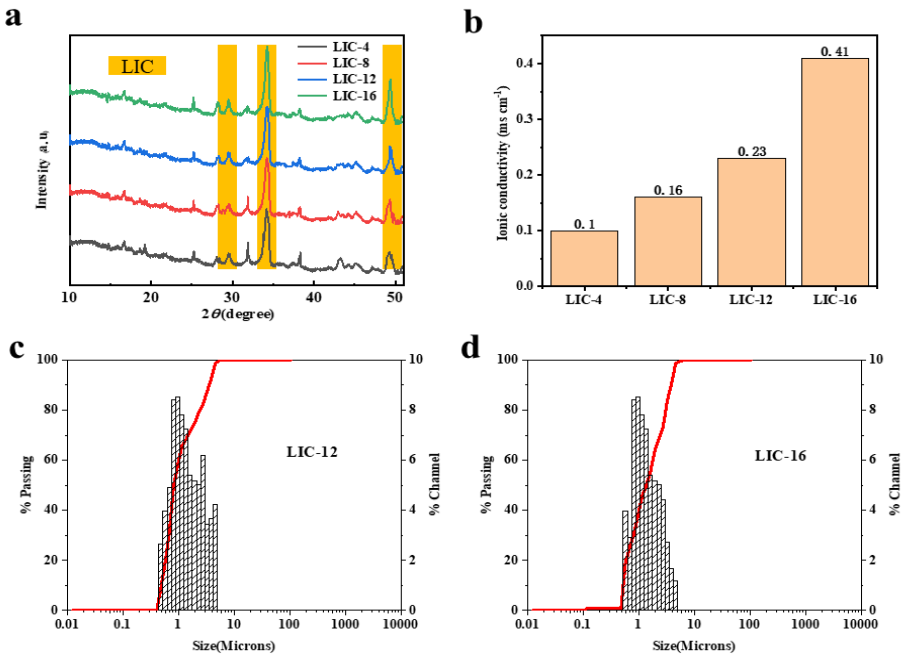

Fig. 2. 4 (a) XRD evolution pattern of the product as the ball milling time increases. (b) Ion conductivity at different ball milling times. (b) Particle size distribution plot of LIC-12. (b) Particle size distribution plot of LIC-16.

As the ball milling time gradually extends, the D_{50} of the product gradually decreases, the content of small particles gradually increases, and the size of the product shows a downward trend (Fig. A2.4). However, the particle size does not change when the grinding time exceeds 12 h. The particle size distribution of LIC-12 and LIC-16 is roughly the same, which is also consistent with LIC-S (Fig. 2.4c,d). The D_{50} of LIC-12 and LIC-16 is almost the same, which means that their average particle sizes are close, both around 1.5 μm. And shows that the size of the grinding balls and the ball milling speed does not change, the size of the product will

not continue to decrease. In fact, for SSEs, in most cases, as the size decreases, the ionic conductivity increases. This is because the larger specific surface area brings more ions channels, which can help ion transfer[145]. But there are also critical size, when below this size, SSEs are prone to agglomeration, causing the ionic conductivity to not continue to increase or even decrease[146]. And the smaller size also means a higher SSE volume density after compaction. Sometimes this will also lead to an increase in the tortuosity during ion transfer, which is directly reflected in a longer ion transfer distance, means lower ionic conductivity[147]. Previously, we also used ball milling balls with smaller diameters to synthesize LIC with diameters of tens to hundreds of nanometers, and its ionic conductivity did not change significantly compare with before. Therefore, for LIC, a particle size of 1 μm is sufficient[112].

2.3.2 Effect of ball milling speeds on Li_3InCl_6 performance

In the standard procedure, LIC-S is synthesized by ball milling for 20 h. In previous experiments, we have tried a grinding time of up to 16 h, so it is no sense to continue to increase the ball milling time. Considering that the ball milling speed is also an important parameter, we tried to increase the ball milling speed to obtain high-purity LIC faster. However, it is worth noting that when the ball mill speed is too high, on the one hand, because the mechanical energy input increases, the collision and friction energy generated also increases. The grinding balls move close to the inner wall of the jar and will not always fall into contact with materials[148,149]. This greatly weakens the collision and extrusion effect of the grinding balls on the raw materials, which is not conducive to the structural transformation of the material. On the other hand, due to the strong effect of mechanical dissipation energy and friction energy, insufficient cooling will cause the temperature in local areas to be too high, which will also affect the transformation of the material into the expected structure[150]. Therefore, in our previous experiments, when the speed exceeds 1000 rpm, pure LIC cannot be obtained no matter how the grinding time changes. There are always intermediate phases and impurities, and the ionic conductivity is always lower than 0.1 mS cm^{-1}. Among them, the most typical microstructure appears as two-dimensional flakes reconstituted after high-energy ball milling (Fig. A2.5).

Considering the above reasons and the increase in energy consumption caused by high rotation speed, in subsequent experiments, the ball milling speed is always between 500-800. When the ball milling speed is 600 rpm, pure phase LIC can be obtained after ball milling for 16 h and named 600-LIC-16. The ionic conductivity at this time is 1.16 mS cm^{-1}, slightly lower than LIC-S (Fig. 2.5a). The electronic conductivity is 4.8×10^{-6} mS cm^{-1} and the activation energy is 0.36 eV, which is close to LIC-S (Fig. 2.5b,c). It shows that appropriately increasing the ball milling speed can reduce the ball milling time while maintaining performance. The particle diameter at this time is also around 1-2 μm, which shows that a small increase in speed will not change the product size.

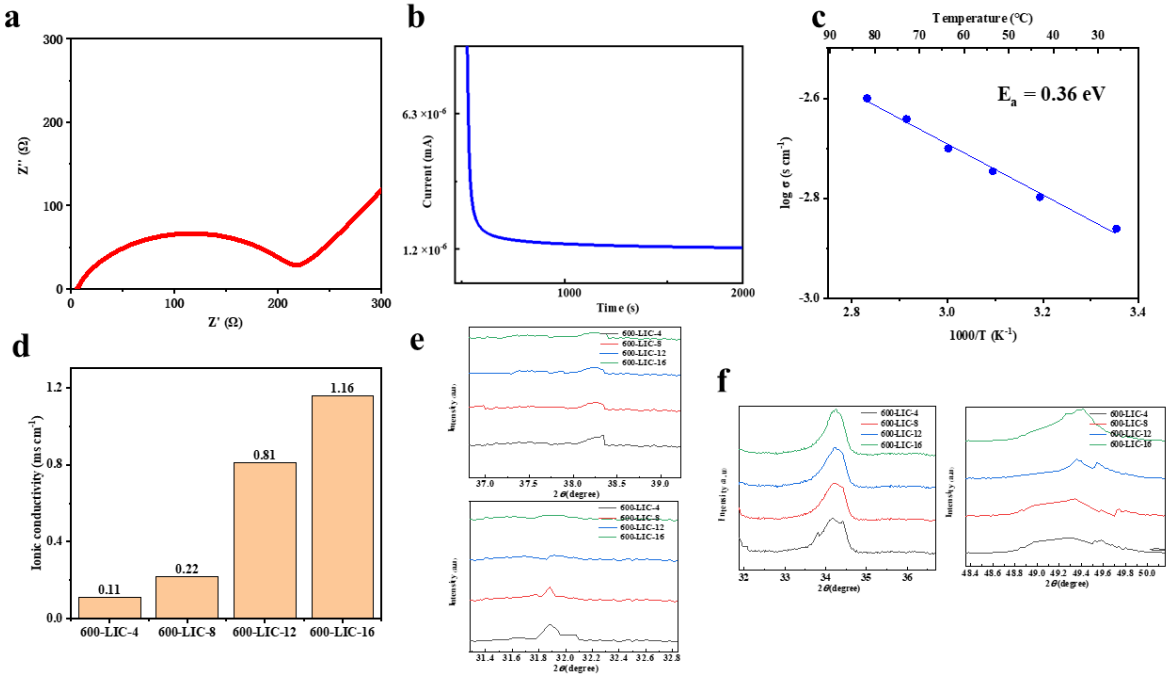

Fig. 2. 5 (a) EIS plots of 600-LIC-16 at 25 ℃. (b) Polarization current–time curve of 600-LIC-16 with an applied external voltage of 2 V. (c) Arrhenius plot of 600-LIC-16. (d) Ion conductivity at different ball milling times. (e) (f) Partially amplified XRD Pattern.

When ball milling for 4, 8, and 12 h, the ionic conductivities were 0.11, 0.22 and 0.81 mS cm^{-1} respectively (Fig. 2.5d). And named 600-LIC-4, 600-LIC-8, 600-LIC-12. Compared with 500 rpm, the ion conductivity of 600-LIC-4 did not significantly increase, it was only 0.01 mS cm^{-1} higher than LIC-4. It is difficult to define whether this is an actual increase or whether it is accuracy during the experiment. The ionic conductivity of 600-LIC-8 is significantly higher than that of LIC-8, close to LIC-12. This means that at 600 rpm, when

the ball milling time exceeds 4 h, the formation rate of LIC will be significantly improved, which can be attributed to the higher energy input. Even though the above product composition was not verified under XRD, the low ionic conductivity also shows that there are still many impurities in the LIC at this time. The ionic conductivity of 600-LIC-12 is 350% higher than that of 600-LIC-8, and also far exceeds the LIC-12 at 500 rpm, even reached the performance of pure LIC in some reports, which means that the large-scale formation of the LIC phase occurred after 8 h of ball milling at 600 rpm. Most of the raw materials have been converted into the transition phase that is easier to phase change. Therefore, LIC is rapidly transformed from the transition phase during the subsequent ball milling process, showing a substantial increase in ionic conductivity. The local amplified XRD pattern verified this. The characteristic peaks of LiCl and $InCl_3$ almost disappeared. The peak intensity at 31.9° and 38.3° gradually decreased with the increase of ball milling time, were almost invisible in 600-LIC-12 and completely disappeared in 600-LIC-16 (Fig. 2.5e). The intensity of the characteristic peaks of the transition phase and LIC increases rapidly, such as 34.2 and 49.4° (Fig. 2.5f). During ball milling for 12-16 h, on the one hand, the remaining LiCl and InCl3 are consumed. On the other hand, the transition phase continues to transform into LIC, so the 600-LIC-16 does not contain other impurities, and the ionic conductivity is approximately 35% higher than 600-LIC-12. The particle size of the product gradually decreases with the prolongation of the ball milling time, but after the ball milling time exceeds 12 h, the particle size no longer changes significantly, and a small amount of difference may be due to the accuracy of the measurement (Table A2.2).

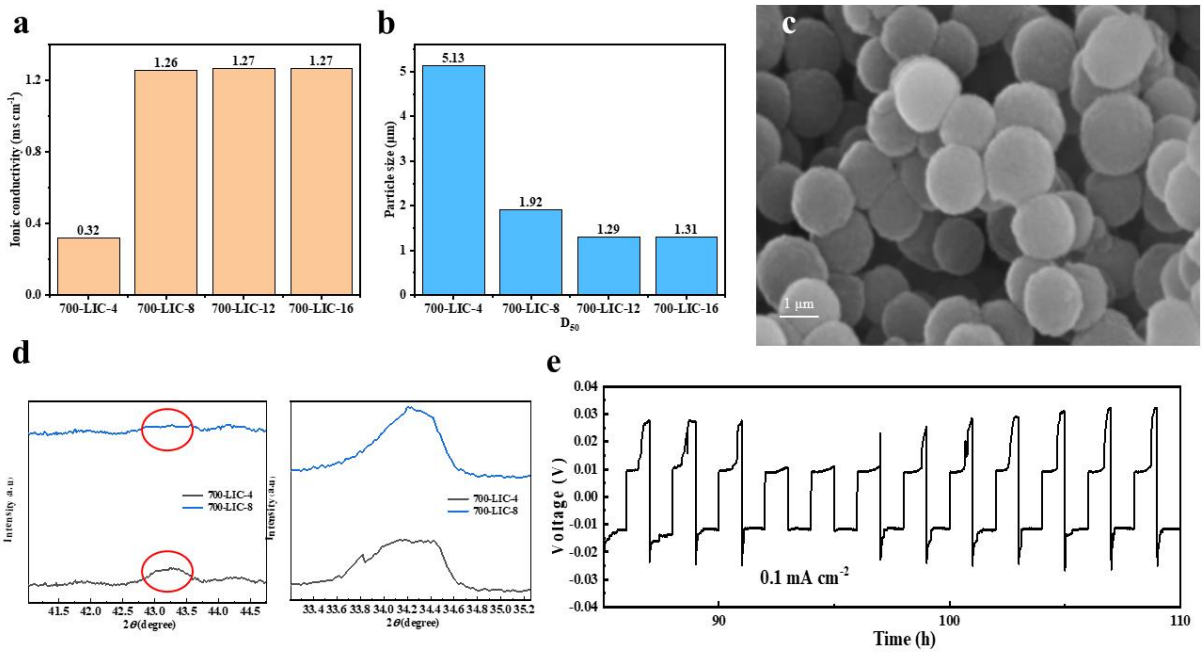

Fig. 2. 6 (a) Ion conductivity at different ball milling times. (b) D_{50} at different ball milling times. (c) SEM image of 700-LIC-8. (d) Partially amplified XRD Pattern. (e) Galvanostatic stripping/plating voltage profiles of symmetric Li |700-LIC-8| Li cell during cycling.

When the ball milling speed was 700 rpm, synthesis experiments were also conducted at different usage times of 4, 8, 12, and 16 h. And named 700-LIC-4, 700-LIC-8, 700-LIC-12, 700-LIC-16. The results show that the D_{50} of 700-LIC-4 is 5.13 μm, the ionic conductivity is 0.32 mS cm^{-1}, and it still contains many impurities (Fig. 2.6a). 700-LIC-8 is pure LIC with an ionic conductivity of 1.26 mS cm^{-1}(Fig. 2.6b). The electronic conductivity is 1.1×10^{-6} mS cm^{-1} and the activation energy is 0.30 eV, so the electrochemical performance is even better than LIC-S (Fig. A2.6). 700-LIC-8 appears as spherical or ellipsoidal structure in SEM, its size is slightly larger than LIC-S, and the particle size is 1.5-3 μm (Fig. 2.6c). Particle size distribution testing also confirmed that D_{50} is 1.92 μm. This is due to the shorter ball milling time. Although the faster ball milling speed makes the LIC phase formed faster, but the shorter ball milling time is not enough to shear the product to the minimum size under this condition. Although the size is slightly larger at this time, there will be some difficulties during powder compaction, but in subsequent research, LIC pellet is rarely used as the research object, and the liquid phase method is always used to apply LIC, so the slightly larger size will not impact on practical applications. The change from 700-LIC-4 to 700-LIC-8 can be clearly seen from the partially amplified XRD pattern. The impurity peaks

represented by LiCl and $InCl_3$ completely disappear, and the intensity of the LIC peak rises rapidly (Fig. 2.6d). This also proves the strong phase transformation tendency under this ball milling condition from another perspective. The sharp characteristic peaks indicate that the crystallinity of LIC does not changed with the shortening of ball milling time. This is because the additional mechanical energy brought by higher speed promotes the crystallization of LIC. Symmetrical cell tests were also performed, running at a current density of 0.1 mA cm^{-2} for more than 90 h before short circuit occurred, even better than LIC-S, which may be due to the larger particle size (Fig. 2.6e). Logically, the ionic conductivities of 700-LIC-12 and 700-LIC-16 are both 1.27 mS cm^{-1}. The minimum D_{50} at 700 rpm is 1.29 μm, which is smaller than that at 600 and 500 rpm. This is due to the greater shear force given by the faster ball milling speed. Considering that mechanical properties are also important parameters for SSEs, we also measured the elastic modulus and hardness of 700-LIC-8. Both the elastic modulus and hardness decrease with increasing indentation load and appear to gradually stabilize at higher loads, with the elastic modulus and hardness measured at 50 mN load being 33.6 ± 3.17 GPa and 3.17 ± 0.21 GPa (Fig. 2.7), respectively. Lower than most oxide SSEs and similar in performance to sulfide SSEs, this helps enable ASSB operation at low or no external pressure[151-153]

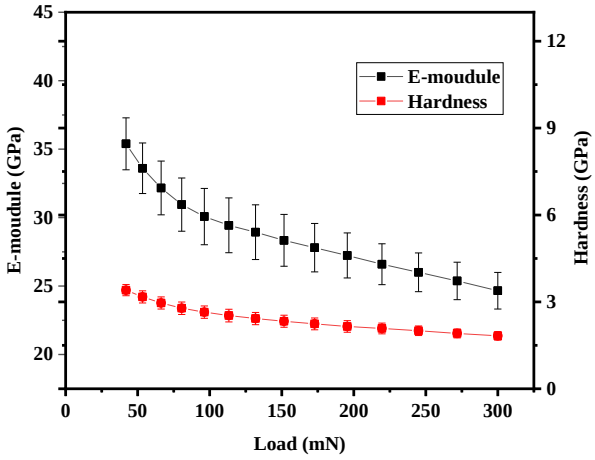

Fig. 2. 7 Elastic modulus and hardness of 700-LIC-8 determined from indentation as function of load. The average of 20 experiments is shown with error bars representing one standard deviation.

To verify the impact of higher speed on LIC synthesis efficiency, the ball milling speed was further increased to 800 rpm. The results show that when the ball milling time is 4 h, the ionic conductivity of the product is about 0.34 mS cm^{-1}, no significant difference compared to 700 rpm. Set a single time gradient to 1 h (such as 5 h, 6 h, 7 h, etc.) and continue the experiment. As the ball milling time increases, the ion conductivity also increases (Fig. 2.8a). However, the ball milling time still needs to be extended to about 8 h to obtain an ionic conductivity (1.24 mS cm^{-1}) close to LIC-S, which means that pure LIC can only be obtained at this time. This further confirms that the rapid LIC generation process exists after 4 h and the transition phase occupies the main component before 4 h[154]. The microstructure and dimensions of LIC at this moment have not changed significantly compared to those at 700 rpm, but the surface roughness is slightly improved (Fig. 2.8b,c). In symmetrical cell testing, the 800-LIC-8 short-circuited after operating at a current density of 0.1 mA cm^{-2} for more than 68 h (Fig. 2.8d). Although the speed continued to increase to 800 rpm, the time required to synthesize LIC was not shortened, and it did not show better performance.

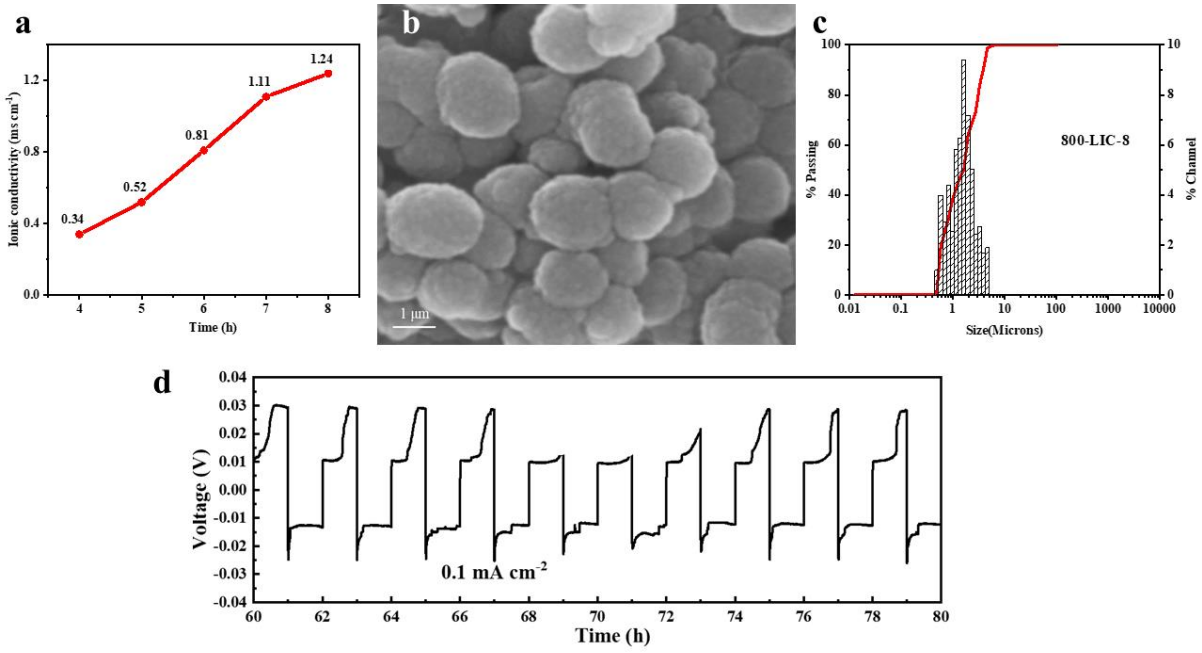

Fig. 2. 8 (a) Ion conductivity at different ball milling times. (b) SEM image of 800-LIC-8. (c) Particle size distribution plot of 800-LIC-8. (d) Galvanostatic stripping/plating voltage profiles of symmetric Li |800-LIC-8| Li cell during cycling.

Based on the previous experimental results, it can be considered that when the ball milling speed is 700 rpm and the ball milling time is 8 h, it is the best condition for synthesizing LIC. Compared with the previous 20 h, the new strategy saves 60% of the time. Moreover, the resulting LIC has higher ionic conductivity and lower electronic conductivity, and shows better stability in the lithium symmetrical cell. Although the average particle size increases slightly, it does not affect subsequent applications. The ball milling speed is increased from 500 rpm to 700 rpm, but it is still at a low level and will not significantly increase the energy consumption of the planetary ball mill. This study successfully improved the strategy of mechanochemical synthesis of LIC. By increasing the ball milling speed, the synthesis time was greatly reduced while maintaining the high performance of the product.

2.4 Conclusions

In summary, this study successfully synthesized high-performance LIC SSE powder through an improved rapid mechanochemical method, and for the first time achieved LIC synthesis with a ball milling time of less than 10 h. First, the impact of reducing the synthesis time at 500 rpm on the purity of LIC was verified. After it was found that pure LIC could not be obtained after the time was lower than the standard time. Therefore, in the subsequent experiments, the rapid synthesis of LIC was mainly achieved by increasing the ball milling speed. When the ball milling speed was increased from the initial 500 rpm to 700 rpm, the ball milling time could be reduced to 8 h. It saves 60% of the time compared to the standard procedure. The average particle size of the LIC powder obtained under this condition is 1.92 μm, and the microstructure is rough spherical or ellipsoidal. After the powder is pressed into pellets, it has a maximum ionic conductivity of 1.26 mS cm^{-1} at 25 °C, the electronic conductivity is as low as 1.1×10^{-6} mS cm^{-1}, and has a low activation energy of 0.3 eV. In the lithium symmetrical cell without buffer layer, short circuit occurred after working for more than 90 h. When the ball milling speed was increased to 800 rpm, the synthesis time of LIC was not shortened and the performance was not further improved. Although the liquid phase method to synthesize LIC is simpler it has shortcomings in performance and the mechanochemistry is favored by researchers in precise research. Therefore, the improved mechanochemical method of synthesizing LIC in this study has great practical significance,

and can greatly improve the production efficiency of LIC to promote the development of HSSEs.

Annex II

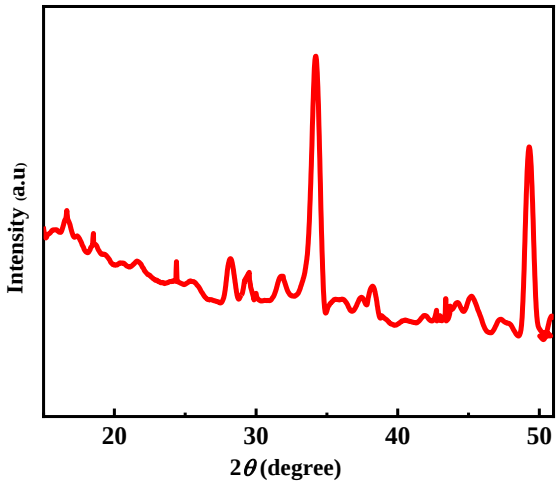

Fig. A2. 1 XRD pattern of LIC-S

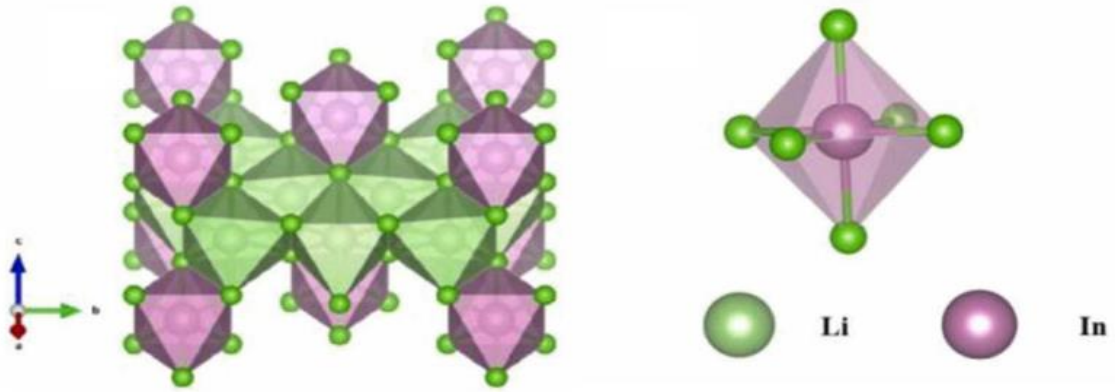

Fig. A2. 2 Crystal structure of Li_3InCl_6 and $InCl^{3-}$octahedra

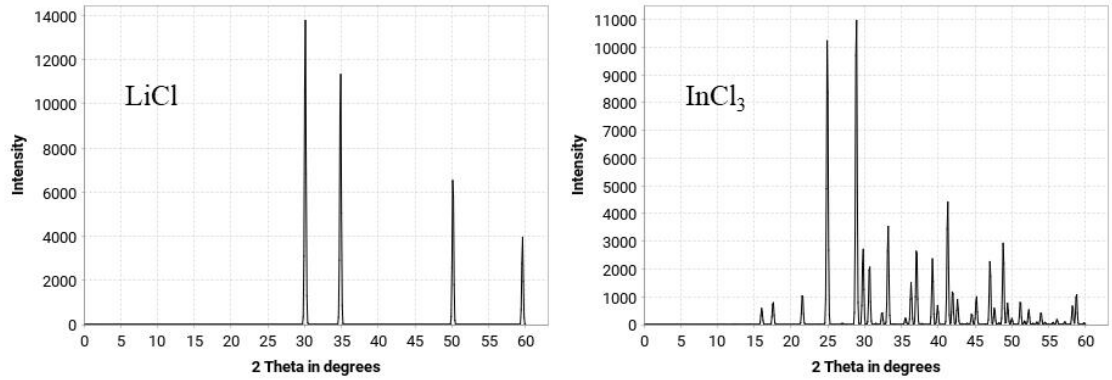

Fig. A2. 3 Standard XRD pattern for $InCl_3$ and LiCl

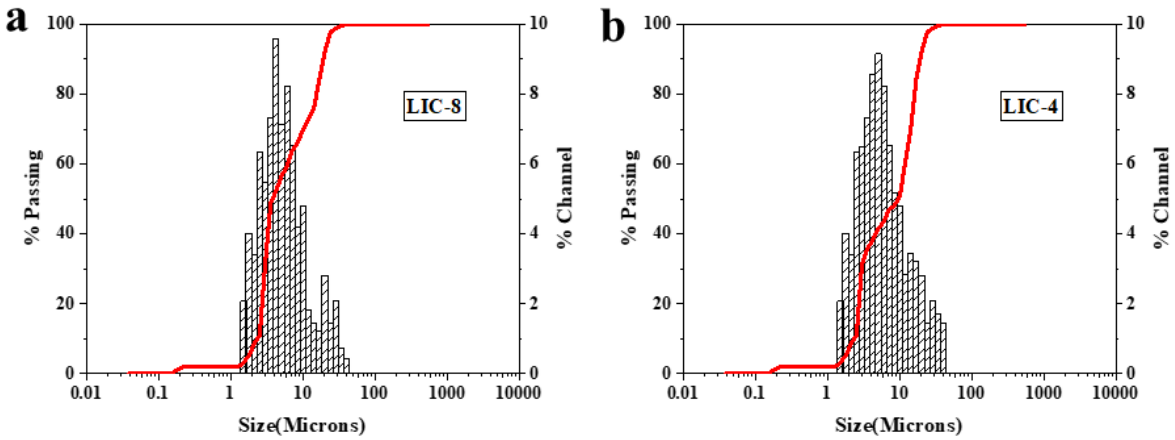

Fig. A2. 4 (a) Particle size distribution plot of LIC-8. (b) Particle size distribution plot of LIC-4.

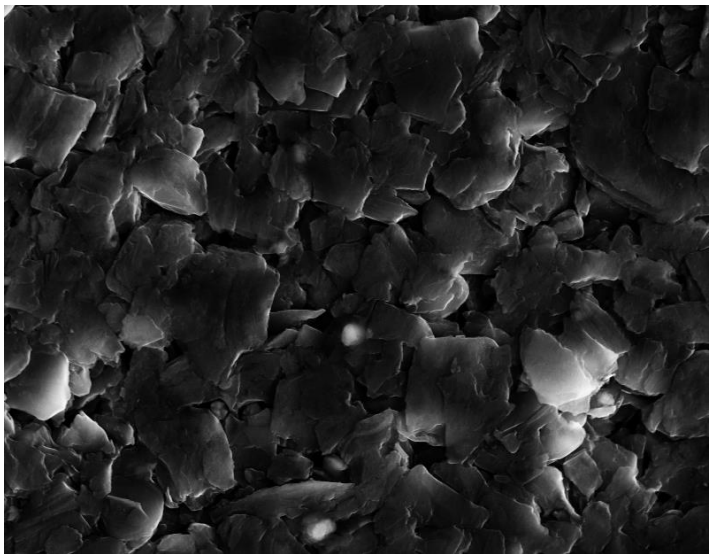

Fig. A2. 5 SEM image of typical microstructure when rpm exceeds 1000

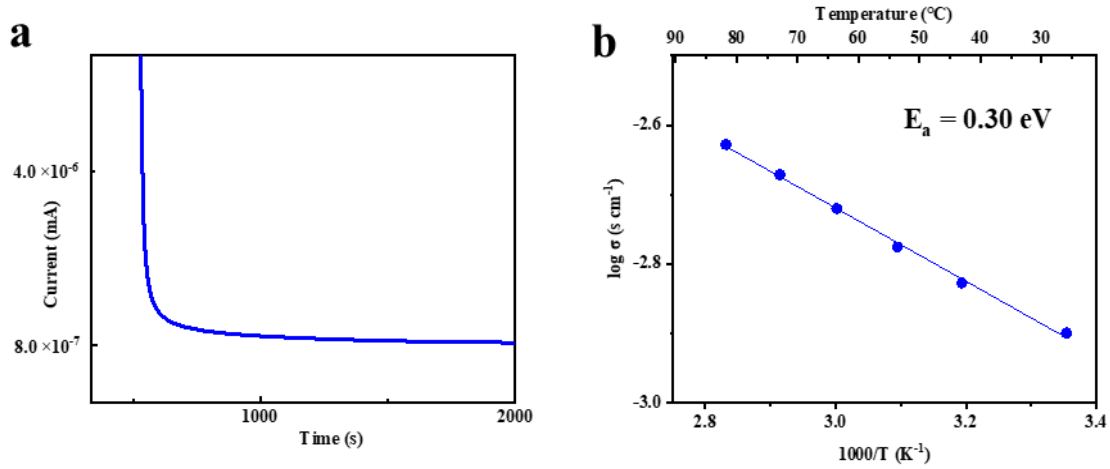

Fig. A2. 6 (a) Polarization current–time curve of 700-LIC-8 with an applied external voltage of 2 V. (b) Arrhenius plot of 700-LIC-8.

Table A2. 1 Comparison with reported LIC ionic conductivity

Ref	Ionic conductivity (mS cm^{-1})
[74]	1.49
[155]	0.6
[156]	1.03
[157]	0.98
[80]	2.04
[158]	1.68
[159]	0.79
[160]	2.0
[161]	1.29

Table A2. 2 D_{50} of LIC synthesized under different conditions

LIC	D_{50} (μm)
LIC-4	8.54

LIC-8	3.46
LIC-12	1.45
LIC-16	1.44
600-LIC-4	8.23
600-LIC-8	3.03
600-LIC-12	1.40
600-LIC-16	1.38

Chapter III: Fabrication of Thin Film Li_3InCl_6-Acetonitrile Electrolyte for SSB by Solvent Casting Method

3.1 Introduction

Although HSSE has only begun to attract renewed attention from researchers since 2018[61], they have good prospects for application as they combine the properties of different electrolytes, can be easily synthesized by ball milling, have high ionic conductivity at room temperature, are cost-efficient, and have some flexibility and air stability[74]. Moreover, some of the HSSEs can be synthesized on a large scale by the liquid-phase method, and the whole synthesis process only needs to be carried out under an inert gas atmosphere or vacuum and below 200 °C[162,163].

However, like most SSEs, the application conditions of HSSEs are very harsh. First, the powdered electrolyte must be molded under a pressure of more than 100 MPa, and then the mixed powder of cathode and electrolyte needs to be spread on one side and high pressure is applied again. The anode is placed on the other side of the electrolyte and pressure is applied a third time, and finally the sandwich-structured pellets are obtained for electrochemical testing. Moreover, high pressure needs to be maintained throughout the electrochemical test to maintain close contact between different interfaces to ensure the good operation of the battery[164,165]. The entire pellets preparation process must be prepared by at least three powder pressings, so is lengthy and difficult to manage[166]. On the one hand, the resulting pellet is highly brittle and prone to fracture under the action of external forces, and during the long-term operation of SSBs, their structure will also change under the action of micro-stress, and cracks and other phenomena will occur, resulting in performance degradation or even short circuit. Since it needs to be manufactured under uniform high pressure, it is difficult to manufacture large-area pellets at a time, and the production efficiency is low, which undoubtedly reduces the possibility of expanded production.

To avoid the limitations of pellets on SSBs, we prefer to use flexible film-like SSE synthesized by the liquid phase method to achieve HSSE operation at lower external pressure,

and the SSE itself does not need to be pressed. Inspired by the electrode slurry and liquid phase deposition methods, we have improved the solution casting method by mixing LIC, binder, solvent and other components into a slurry and pouring it onto the surface of the filter membrane to produce LIC-ACE films. The resulting samples can be easily peeled from the filter membrane with tweezers, do not break when bent, and show good resistance to humidity. They also have a high lithium ion conductivity of 0.76 mS cm^{-1} at room temperature and show good electrochemical performance in symmetrical cells and SSBs. At the same time, we also characterized its structure and other characteristics through SEM, XRD, XPS and other technologies. In this study, high-performance LIC-ACE films were fabricated by an improved solution casting method that eliminates the need to press the LIC powder, only the electrode powder needs to be pressed, greatly reducing the time-consuming manufacturing of pellets, and eliminating the limitations imposed by the compressed surface. It can work under pressure less than 1 MPa, greatly reduces the impact of external pressure on the performance of SSBs in past studies, further promoting the practical development of SSEs.

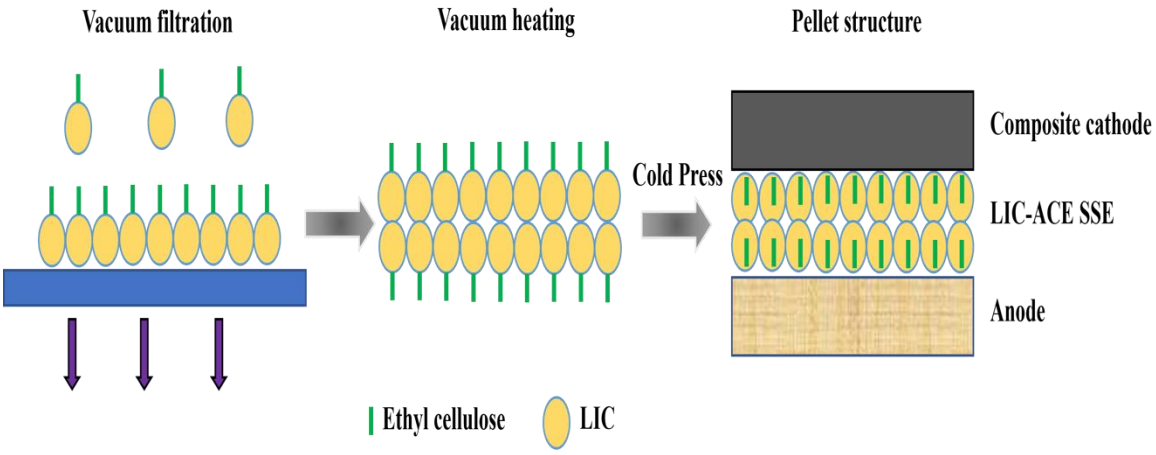

Fig. 3. 1 Schematic illustration of fabrication of LIC-ACE film

3.2 Experimental Section

3.2.1 Preparation of Li_3InCl_6-Acetonitrile film

The anhydrous lithium chloride (LiCl, Innochem, 99.99%) and anhydrous indium chloride ($InCl_3$, Sigma-Aldrich, 98%) were dissolved in deionized water in the ratio of 3:1 (molar ratio) and then dried under vacuum at 100 °C until most of the water evaporated, and finally dried under vacuum at 200 °C for 6 h to obtain the final product LIC.

To prepare the electrolyte film 95 mg of LIC and 5 mg of ethyl cellulose (Sigma-Aldrich, 48.0% (w/w) ethoxy basis and an average molecular weight of 100 g/mol) were added to 1 mL of anhydrous acetonitrile (CH_3CN, Sigma-Aldrich, 99.8%), followed by slow magnetic stirring until powders are completely distributed in the solvent. The solution was slowly poured onto polymer filter membrane and vacuum filtered for 1 h to remove most of the acetonitrile. The microstructure of the filter membrane is shown in Fig. A3.1. Finally, the full dry sample is obtained by heating at 80 °C for 12 h under vacuum. At this point, the final sample, which we call LIC-ACE, is separated from the filter membrane with tweezers and has the form of a translucent film under light.

3.2.2 Characterization methods

The microscopic morphology and structure of the samples were observed by scanning electron microscopy and the elemental distribution was determined by energy dispersive spectroscopy. Ion conductivity, Electrochemical Impedance Spectroscopy (EIS), Cyclic Voltammetry (CV), charge/discharge tests were performed on a Biologic VSP Potentiation (France, Grenoble) and NEWARE BT4008 (China, Shenzhen). The microstructure is visualized with a scanning electron microscope (SEM) **(**Zeiss Germany**)**. The crystal structure was determined by X-ray diffraction (XRD) using Rigaku MiniFlex X-ray diffractometer with Cu Kα radiation (λ = 1.54178 Å) (Japan, Tokyo). Information such as binding energy was collected using Al Ka source X-ray photoelectron spectroscopy (XPS) at 15 kV and 20 mA by PHI 5800 workstation (USA, Minneapolis). Stability under dry air was

measured by thermogravimetric analysis (TGA) on Mettler Toledo Thermogravimetric Analyzer (Germany, Giessen). The specific surface area and adsorption/desorption curves were determined by ASAP 2020 PLUS BET analyzer using krypton at 77.39K (USA).

3.2.3 Electrochemical performance measurement

The ionic conductivity was measured by EIS using LIC-ACE films peeled from the filter membrane by constructing SS|LIC-ACE|SS test bench. The test conditions are the same as in the last section.

Other electrochemical tests were performed by constructing SSB, the cathode part is made by simply mixing LIC and NCM111 powder at a weight ratio of 3:7. At this time, the electronic conductivity of the composite cathode under high pressure has met the experimental requirements. Since we mainly focus on the research of SSE, we need to keep other components as simple as possible, and we do not add conductive agents. For the specific assembly process, 20 mg of the cathode composite material was placed on one side of the LIC-ACE film and then pressed with a pressure of 147 MPa. Finally, the Li foil is placed on the other side of the LIC-ACE film and pressed with a pressure of 98 MPa to obtain a sandwiched pellet for electrochemical testing. The test bench setup for SSBs test is shown in Fig. A3.2, and the external pressure maintained is less than 1 MPa during the test, the minimum work pressure can be as low as 200 KPa.

The E_a was computed by same way like last section.

3.3 Results and Discussion

3.3.1 Characterization of structural of Li_3InCl_6-Acetonitrile

LIC-ACE was prepared by casting LIC slurry on the surface of polymer filter by solution casting method. To evaluate the effect of different solvents on the result, we tested different solvents to their polarity, and the LIC-ACE, obtained using acetonitrile as the solvent, had

the best overall performance. To obtain a structurally strong and flexible film, we added a small amount of amphiphilic binder such as ethyl cellulose (EC) to help the film formation[167,168]. It has been verified by many experiments with different amounts of EC added, it is finally determined that the addition of EC 5% is the best. The smooth and porous polymer filter membrane was selected as the support for the LIC-ACE film.

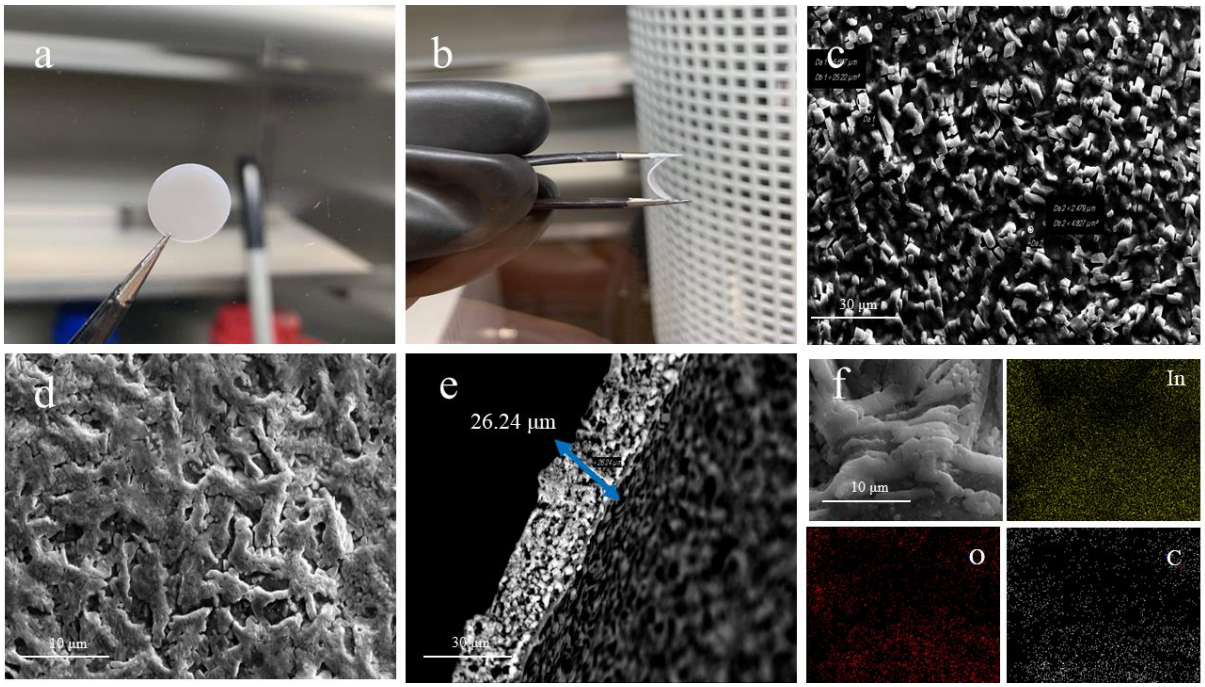

Fig. 3. 2 (a) digital photo of LIC-ACE after cut. (b) Bending test of LIC-ACE. (c) SEM image of particle size of LIC-ACE. (d) SEM image of LIC-ACE structure. (e) SEM image of edge thickness of LIC-ACE. (f) EDS element mapping of LIC-ACE.

The LIC-ACE appears under the light as a smooth milky film. By bending the filter membrane it can first be separated from the LIC-ACE, and then the complete LIC-ACE can be easily peeled off by using tweezers. Use punch to process LIC-ACE to get an edge-complete coin and after bending there are wrinkles, but the overall structure is still intact and there are no obvious breaks (Fig. 3.2a,b). We also tried to use traditional binders such as CMC and PVDF to prepare LIC film, but did not perform well, the film cracked after solvent removal and was not flexible (Fig. A3.3). This may be because the functional groups on the traditional binder can only form a stable structure with better cross-linking bonds with Li^+, while other ions such as In^{3+} cannot become good electron acceptors[169].

The LIC-ACE film appeared in SEM images as densely stacked nanorod clusters, with most of the rod-shaped monomers having a diameter of 2-6 μm and a length of about 50 μm (Fig. 3.2c). The monomers are connected by bridges, forming a relatively dense network structure that favors ion transport and provides structural strength (Fig. 3.2d). The longitudinal stacking between layers is relatively dense, but there are still some gaps and the densities can be further improved by applying a suitable pressure[170]. And the edge thickness is about 26 μm, reaching the thickness of commercial polymer separators (Fig. 3.2e). The results of EDS mapping show that elements such as C, O, In and Cl are evenly distributed. This shows that no material agglomeration occurred on the surface of LIC-ACE and the EC is well deposited in the LIC-ACE film providing mechanical stability and flexibility as the skeleton and does not participate in ion transfer (Fig. 3.2f, A3.4). The micropores, which serve as ion transport channels, are distributed over the entire surface, and pores are also present in the cross-section to prevent ion blockage (Fig. A3.5). In subsequent electrochemical tests, LIC-ACE will be used after high-pressure compaction, and the porosity of the film will be further reduced to avoid short circuits caused by direct contact between electrodes penetrating the film[171,172]. But the remaining micropores still allow Li^+ to pass evenly and rapidly through the electrolyte layer during charging and discharging[173-175]. And reduces the uneven deposition of lithium dendrites, which is one of the reasons for the good electrochemical performance[176]. The minimum thickness reachable with this method is around 10 μm however some mechanical constraints rise below 20 μm due to the reduced toughness that makes the cell assembling particularly difficult. Since it is synthesized by the liquid phase method, the thickness of the LIC-ACE film can be easily controlled, which also facilitates subsequent electrochemical tests such as ionic conductivity.

3.3.2 Characterization of physicochemical properties of Li_3InCl_6-Acetonitrile

The XRD results of LIC-ACE are shown in Figure 3.3a, and most of the sharp characteristic peaks, such as 13.9°, 27.4°, 33.6° and 48.4°, can be well indexed by Li_3InCl_6 (ICSD No. 89167, $C_{2/m}$) with the monoclinic rock-salt structure[80]. The typical crystal structure of Li_3InCl_6 is shown in Figure. 3.3b. Compared to the standard pattern, it is likely that the presence of residual tensile stress causes the anisotropic shrinkage of the lattice because EC has a high tensile strength (47-72 MPa), resulting in lattice distortion and larger interplanar spacing so that the peaks shift slightly to low angles. Among them, 13.9° and 33.6° represent the (001) and (131) planes of LIC respectively, and the peak intensity at 33.6° is much larger than that at 13.9°, indicating that the (131) plane is dominant. Because of the heterogeneity, when the (001) plane is the main orientation, it is difficult to arrange the single atoms in the unit cell to form a standard lattice, and Li^+ needs to overcome the interaction between the greater electrostatic force and the lattice[159]. Therefore, when the (131) plane is the main orientation, it can assist the transport of Li^+, which helps to compensate the decrease in ionic conductivity caused by the addition of EC. The peak around 5° can be retrieved as a small amount of residual LiCl, and the intensity of the two peaks between 27–31° exceeds expectations, which can be attributed to the superposition of LiCl and LIC[177,178]. The blunt peaks of low intensity at 9-12° and 19-22° can be retrieved as EC in LIC-ACE, indicating that EC exists in an amorphous state and is deposited as a skeleton throughout the sample[179]. It inhibits the excessive increase of crystallite size, improves the ordering of crystalline phases and reduces the strain[180]. The higher noise before 30° compared to the reference can also be explained by amorphous EC. The peak intensity of EC is low, does not cause the angle shift of the LIC peak, indicating good compatibility of LIC and EC in the case of acetonitrile as solvent. LIC-ACE presents a clear XRD pattern in total, and the good orientation of the crystal planes is maintained, proving that the solution casting method does not affect the structure and crystallinity of LIC when EC is added.

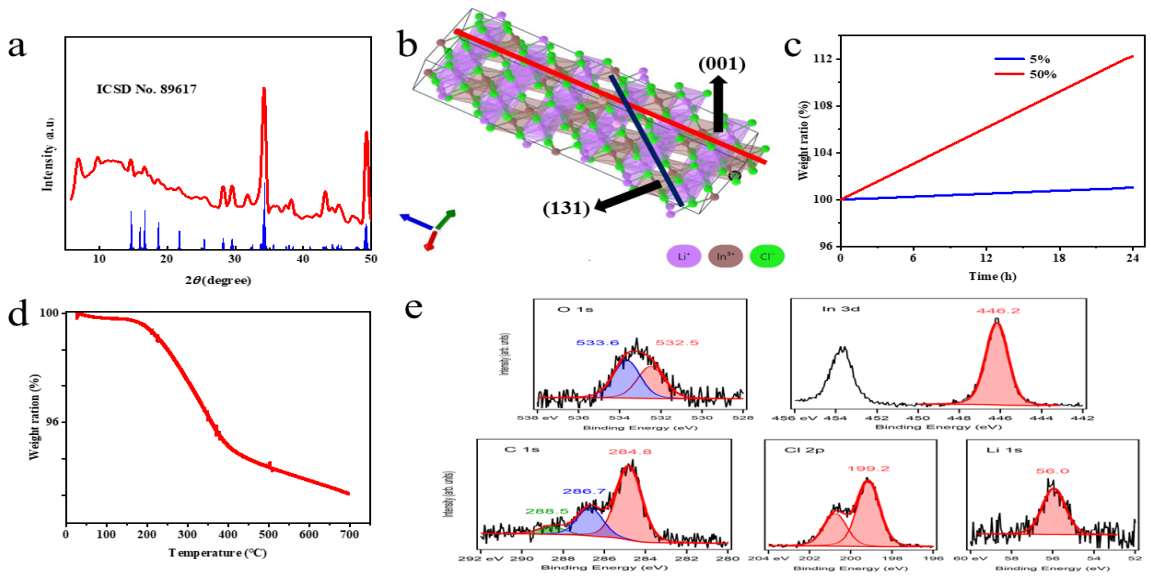

Fig. 3. 3 (a) XRD pattern of LIC-ACE. (b) Typical crystal structure of LIC in the database. (c) Weight change plot of LIC-ACE at different humidity. (d) Thermogravimetric analysis curve of LIC-ACE. (e) O 1s, In 3d, C 1s, Li 1s and Cl 2p, xps spectra of LIC-ACE.

In SSEs, it is usually difficult to keep the properties stable in the air because of water absorption, oxidation, etc. The main problem plaguing HSSEs is strong hygroscopicity, so moisture resistance is also one of the important indicators for performance evaluation. LIC pellets show good stability in dry air, but after only a few minutes of exposure to higher humidity, they absorb moisture and become damp[179]. The slightest touch can cause disintegration of the structure and will gradually dissolve over time. We exposed LIC-ACE to air at 20 °C with 5% and 50% relative humidity at room temperature, and recorded the change in sample weight (Fig. 3.3c). After 24 h of exposure at 5% relative humidity, the weight increase was very small, only about 0.5%, so it can be assumed that the weight of the sample remained relatively stable. After 24 h of exposure at 50% relative humidity, the weight increased by 12.2%, but the shape of the sample did not change and the rigidity was maintained. Compared with LIC, which cannot exist stably in humid air, although LIC-ACE also absorbs a small amount of water, its hygroscopicity has been significantly weakened, especially in a relatively high-humidity environment.

Moisturized LIC-ACE can also recover most of performance after proper heat treatment, which is similar to LIC[80]. The stability of LIC-ACE in 50% relative humidity was also measured at higher temperatures. When the temperature was maintained at 50 °C, there was

a slight decrease in sample weight (about 0.1%) in the first few hours, which can be considered as the removal of a small amount of moisture absorbed during the operation. Afterwards, the sample weight remained unchanged until the end of the 24 h test (Fig. A3.6). This indicates that the stability of LIC-ACE in humid air can be maintained by heating, and the minimum maintenance temperature of 50 °C does not cause a large consumption of energy. The stability of LIC-ACE at high temperatures was verified by TGA, which was tested by heating the sample from room temperature to 700 °C at a rate of 5 °C min^{-1}. Until the temperature exceeds 200 °C, the weight of the sample begins to decrease, and EC begins to decompose, which proves that LIC-ACE has sufficient resistance to high temperature, and the solvent can be completely removed by heating at high temperature during the preparation process (Fig. 3.3d)[179]. LIC-ACE can remain intact at a temperature not exceeding 200 °C and has a certain resistance to air environments. Further, the trouble of moisture in the air can be eliminated by lower heating temperatures.

The details of the LIC-ACE binding energy change were further determined by XPS spectra (Fig. A3.7). The peaks of In $3d_{5/2}$ at 446.2 eV and In $3d_{3/2}$ at 453.8 eV, Cl 2p at 199.2 eV, O 1s at 532.5 and 533.6 eV, are consistent with previous reported publications (Fig. 3.3e)[74,78,159,181]. The peak of Li 1s shifted from the reference 56.6-56.2 to 56.0 eV, which can be attributed to the introduction of low electronegativity carbon after the addition of EC, resulting in a decrease in binding energy[182]. The peak of C 1s at 284.8 eV represents the C=C, which may come from the micro-cleavage of EC after heating [183,184]. The peaks at 286.7 and 288.5 eV can correspond to O 1s, representing -COOH, -COH and -COC[185]. The XPS spectrum is consistent with the XRD analysis results, which proves the reliability of LIC-ACE.

The same EC showed a surface area of 6.279 $m^2 g^{-1}$ and a total pore volume of 0.1 $cm^3 g^{-1}$ in past tests[186]. According to the Kr adsorption/desorption isotherm test, The curve is similar to the type IV isotherm, and there is no saturated adsorption platform, indicating that the pore structure is irregular[187]. BET surface area of LIC-ACE containing 5% EC is 1.6818 $m^2 g^{-1}$ and the total pore volume is 0.04 $cm^3 g^{-1}$ (Fig. A3.8). Since LIC is dispersed in the skeleton made of EC as a filler, the significant decrease in the BET surface area and total pore volume

indicates that the pores of the sample have been almost uniformly filled by LIC[188]. It is worth noting that since EC only accounts for 5% of the total mass of LIC-ACE, and the surface area of LIC is always less than 1 $m^2 g^{-1}$, but the final BET surface area still reaches 1.6818 $m^2 g^{-1}$, which also proves that the strategy is successful and the final sample still retains a relatively good surface area that can provide more contact surface for ion transfer.

3.3.3 Characterization of electrochemical performance of Li_3InCl_6-Acetonitrile

The ionic conductivity of LIC and LIC-ACE were characterized by electrochemical impedance spectroscopy of the symmetrical cell of SS|LIC|SS. The ionic conductivity values of LIC and LIC-ACE at room temperature are shown in Figure 3.4a, where ionic conductivity at room temperature is 0.76 mS cm^{-1}. Equivalent circuit for EIS fitting show in Figure A3.9, Where R_2 represents the R_{ct} of the electrode/electrolyte interface, CPE_1 represents R_{sei}, and CPE_2 represents R_w. For comparison, the ionic conductivity of the same batch of LIC prepared by the wet process and subsequently used to make LIC-ACE was 1.09 mS cm^{-1}.. In other studies, the ionic conductivity of LIC is between 0.79-1.49 mS cm^{-1}, which is at a similar level to LIC-ACE[74,156,159,161]. The activation energy (E_a) of Li^+ migration reflects the level of the ion migration barrier and is calculated from the Arrhenius plot obtained from the Nyquist diagram at different temperatures, the LIC-ACE shows that the E_a is 0.289 eV (Fig. 3.4b). Due to the different details of the synthesis method, the activation energy of LIC is slightly different in studies, and the E_a is usually between 0.27-0.35 eV[74,189,190]. Although the activation energy increases after the addition of EC, but is still at the same level compared to the activation energy of LIC in other studies, so the Li^+ migration is almost unaffected on this side.

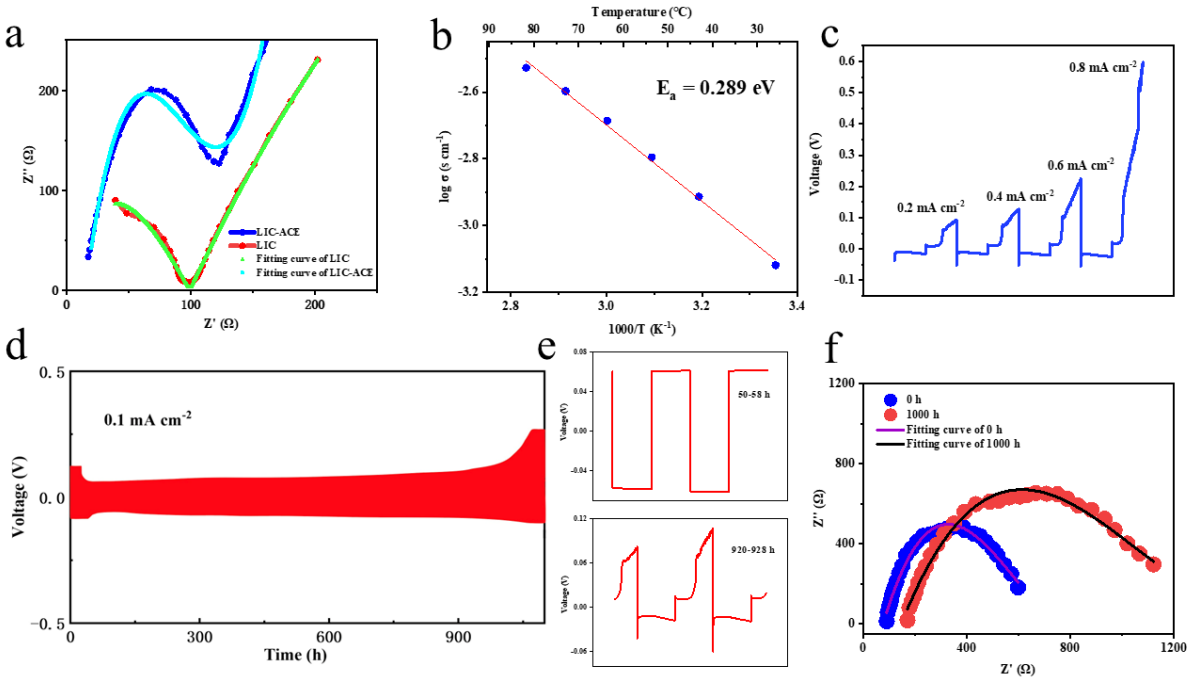

Fig. 3. 4 (a) EIS and fitting plots of LIC-ACE and LIC at room temperature. (b) Arrhenius plot of LIC-ACE. (c) Rate performance of symmetric Li |LIC-ACE| Li cell. (d) Galvanostatic stripping/plating voltage profiles of symmetric Li |LIC-ACE| Li cell during 1100 h cycling. (e) Amplified voltage profiles at 50-54 and 920-924 h. (f) EIS plot of Li |LIC-ACE| Li cell at cycle 0 h and 1000 h.

The symmetrical Li-Li cell without buffer layer was then constructed to verify the interfacial stability of the LIC-ACE/Li metal. At first, with the gradual increase of current density, the overpotential increases slowly from 0.2 mA cm^{-2} before reaching 0.8 mA cm^{-2}, so it can be considered that the critical current density is 0.8 mA cm^{-2} (Fig. 3.4c). Equivalent circuit for EIS fitting show in Figure A3.10. The Li plating/stripping voltage profile show that the LIC-ACE cell could cycle stably for approximately 900 h, with the overpotential always increasing slowly and relatively smoothly without short-circuiting (Fig. 3.4d,e). During cycling, a stable interface gradually forms and the growth of lithium dendrites is limited to acceptable limits. However, after 900 h of cycling, the overpotential suddenly increases abnormally and after a few cycles the increase exceeds the sum of the previous 900 h, indicating a rapid deterioration in the stability of the interface. The test results of EIS at 0 h and 1000 h also prove this point, and the resistance at 1000 h is almost doubled (Fig. 3.4f). LIC is thermodynamically unstable in direct contact with lithium metal, so previous works have often used sulfides as a buffer layer to improve the interfacial contact. We relied on a skeleton of EC to mitigate side reactions and short-circuiting caused by lithium dendrite

penetration. Compared with the low performance of LIC symmetric cells in previous studies, the 900 h stability cycle proved this strategy to be effective[161,182].

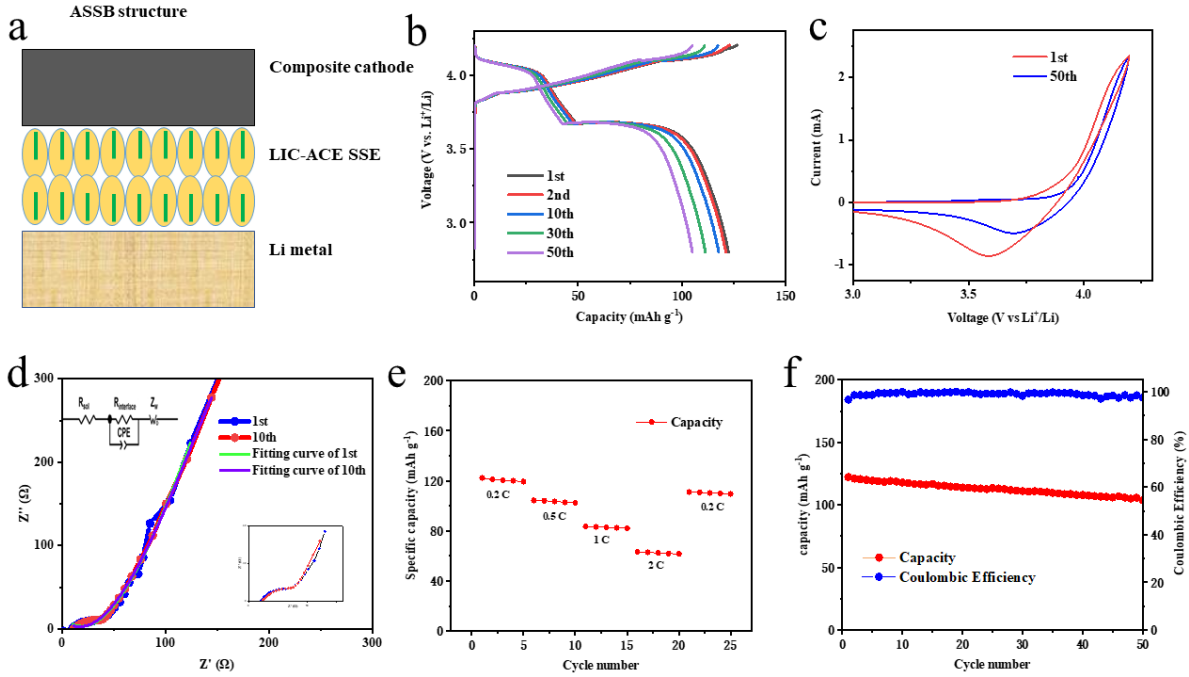

Fig. 3. 5 (a) Schematic of LIC-ACE ASSB structure (b) Voltage profiles of LIC-ACE ASSB at different cycles. (c) CV curves at 1 mV s^{-1} after the first cycle and 50 cycles of LIC-ACE ASSB. (d) EIS, fitting plot and equivalent circuit of LIC-ACE ASSB after the first cycle and after 10 cycles. (e) rate capacity of LIC-ACE ASSB. (f) Cycling performance and CE of LIC-ACE ASSB.

The SSB is assembled by NCM111-LIC mixed cathode, Li metal anode, and LIC-ACE. The initial discharge capacity of SSB is 122.3 mAh g^{-1} at 0.2 C, under the same conditions, the profile of the charge-discharge curve does not change significantly with increasing number of cycles (Fig. 3.5b). The charge-discharge plateau caused by the reversible phase transition can be observed in both the charge-discharge curve and the CV curve (Fig. 3.5c). The trend of the CV curve measured after 50 cycles is similar to the first cycles, indicating the stable cycle performance of the overall electrode-electrolyte system. But the whole system changed a lot after 50 cycles, which caused the oxidation peak and reduction peak in the CV curve to shift significantly compared with the first cycles, and the integral area became smaller[191,192]. It also represents the capacity decrease, which is also consistent with the results of the charge/discharge process.

The EIS plot measured after 10 cycles still shows good performance compared to the first cycle, with only a slight change in the high-frequency range and instead a decrease in resistance in the low-frequency region, also indicating the structural stability of the LIC-ACE (Fig. 3.6d). It is tentatively concluded that the cathode is gradually activated during the charge/discharge process and wets itself with the LIC-ACE, resulting in better interfacial contact, so that the mass transfer resistance between the layers decreases. At various current rates of 0.2, 0.5, 1, and 2 C, the discharge capacities of LIC-ACE ASSB are 122.2, 104.4, 83.6, and 63.3 mAh g^{-1}, respectively (Fig. 3.6e). After the 2 C cycle test, it was cycled again at 0.2 C, and the discharge capacity returned to 111.2 mAh g^{-1}, illustrating the good capacity retention and rate performance of LIC-ACE ASSB. After 50 cycles, the capacity retention rate is 84.8% and the coulombic efficiency (CE) of the first cycle is 94.5%. After 5 cycles, CE can be stabilized at more than 99%, and after 40 cycles, CE fluctuated but remains at 98% (Fig. 3.6f). The high capacity and CE show good cycle stability, indicating that there are fewer side reactions during cycling.

3.4 Conclusions

In summary, this research has successfully demonstrated the feasibility of producing LIC-ACE films as SSEs through a modified solution casting method and for the first time, the charging and discharging of LIC at a pressure below 1 MPa was achieved. The final sample was prepared by simply mixing LIC and EC in acetonitrile and then casting. The LIC-ACE film exhibited high ionic conductivity and good flexibility. LIC-ACE films have high ionic conductivity, and good flexibility and show good moisture resistance in dry air at various temperatures. The skeleton made of EC has good high-temperature performance, LIC are also uniformly filled in the skeleton. The electrochemical performance proves that it has good stability with electrode materials and good compatibility with Li metal, which can effectively reduce the occurrence of side reactions. Although the discharge capacity decreases rapidly, there is still much room for improvement. LIC-ACE films can be synthesized on a large scale by the liquid phase method, saving the time needed to press the powder in the production step, which further promotes the practical development of SSE.

Annex III

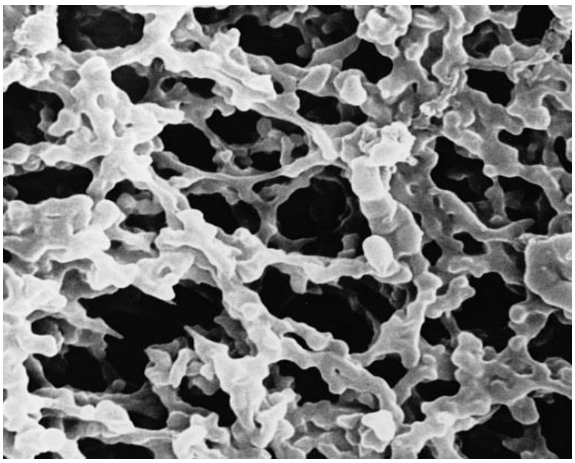

Fig. A3. 1 SEM image of filter membrane microstructure.

Fig. A3. 2 Image of test bench setup for ASSBs.

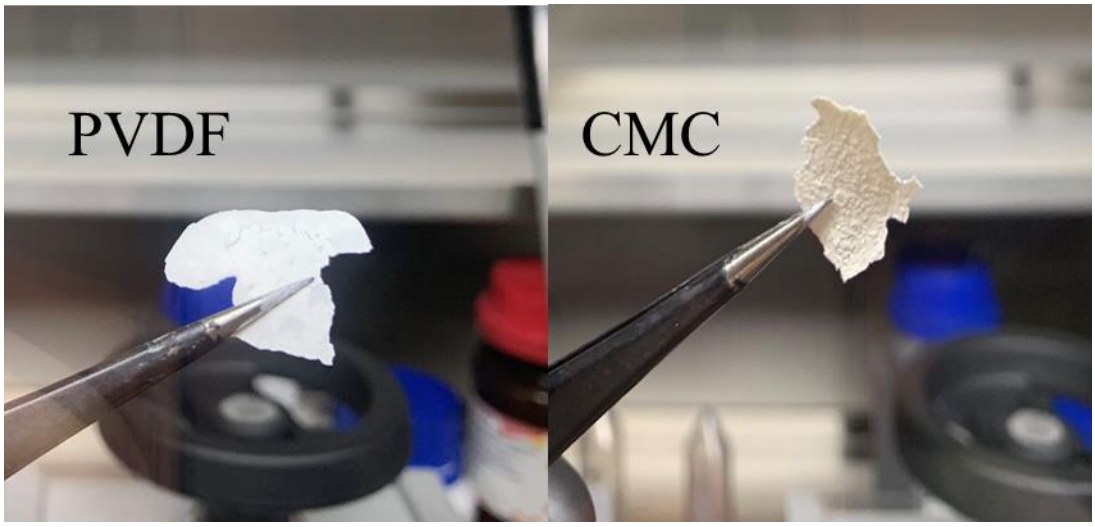

Fig. A3. 3 Digital photo of LIC film made by PVDF and CMC.

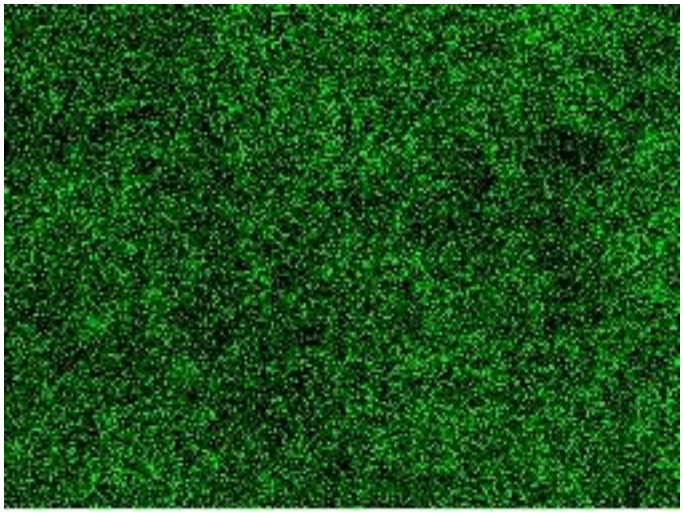

Fig. A3. 4 EDS mapping of Cl elements in LIC-ACE.

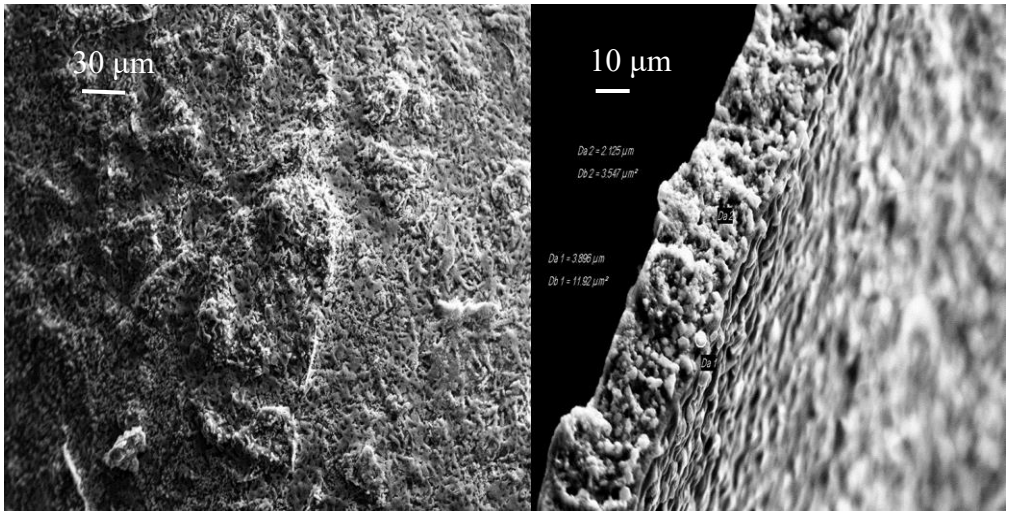

Fig. A3. 5 SEM images of the surface and cross-section of LIC-ACE.

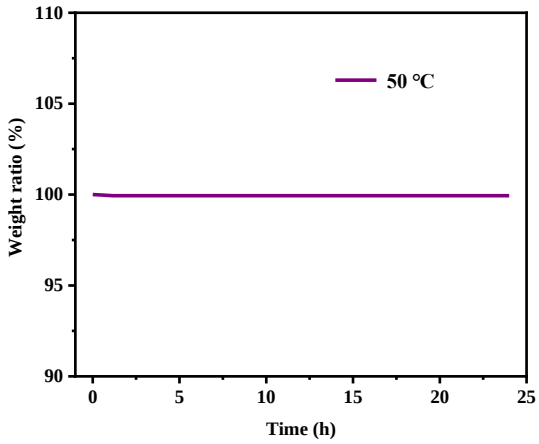

Fig. A3. 6 Weight curve at 50 °C under the condition of 50% relative humidity.

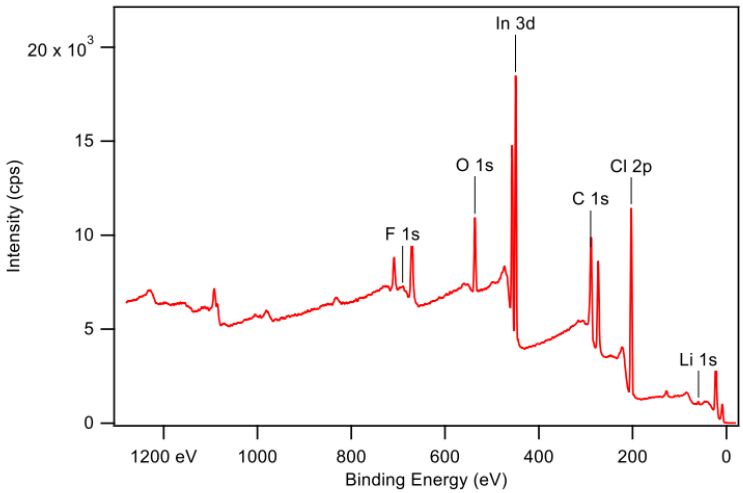

Fig. A3. 7 Overall XPS spectrum of LIC-ACE.

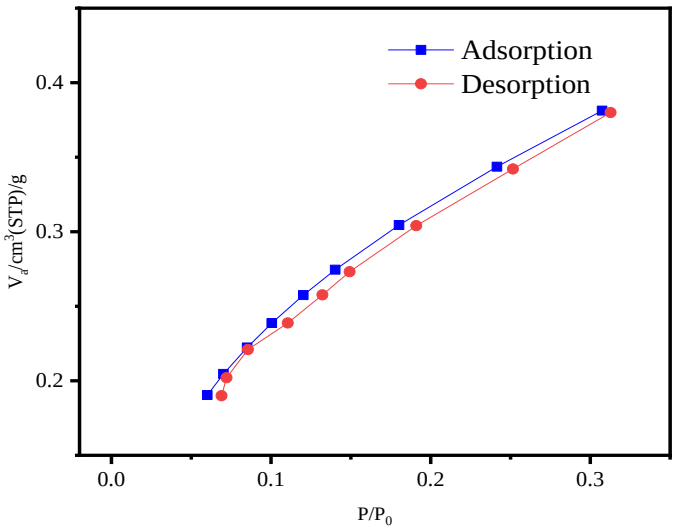

Fig. A3. 8 Kr adsorption isothermal at 77.39 K of LIC-ACE.

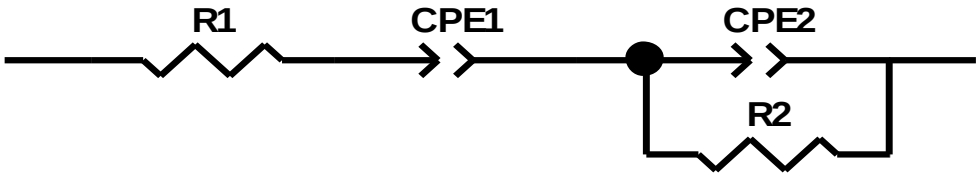

Fig. A3. 9 Equivalent circuit for EIS fitting of LIC-ACE and LIC.

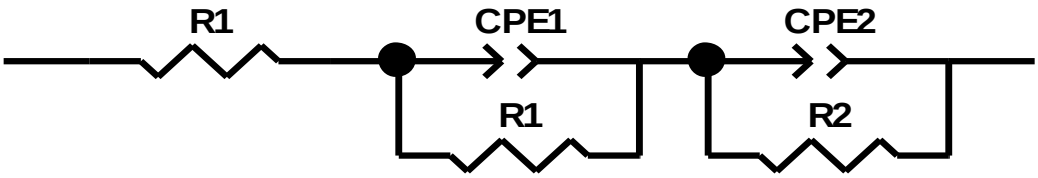

Fig. A3. 10 Equivalent circuit for EIS fitting of Li |LIC-ACE| Li cell.

Chapter IV: Application of Li_3InCl_6-PEO Composite Electrolyte in SSBs

4.1 Introduction

SPEs are also an important type of SSE. Among them, PEO is an important chemical raw material with stable supply and low price, so it has the most research[193]. However, the low performance caused by high crystallinity at room temperature limits its practical application, it usually needs to be compounded with other materials for use[194,195]. On the other hand, HSSEs represented by Li_3YCl_6 (LYC), Li_3InCl_6 (LIC), etc. have received widespread attention in recent years due to their good comprehensive performance since 2018[43,61]. Since halides are not as soft as polymers, they cannot work under normal pressure in most cases[74,196]. The test method is similar to that of sulfide and oxide SSEs, which always need to be made into pellets by powder compression method under high pressure. The pellets are brittle, and the entire preparation and testing process is cumbersome and difficult to promote. Different types of SSEs have their advantages and disadvantages, so in recent years, the research on mixing different SSEs to make composite SSEs with multiple advantages has become increasingly popular. SPEs usually do not need to be operated under pressure due to their good flexibility, so they are usually used as components of composite SSEs and are favored by many researchers.

In the previous work, we combined LIC with EC to form a LIC-ACE thin film SSE, which could operate at a pressure of less than 1 MPa. However, during the construction process of the cell, the cathode and anode still need to be adhered to the SSE through high pressure, which still limits its application to a certain extent. Composite SSEs formed by SPEs and oxides or sulfides are often reported and because the stronger flexibility and the gradual formation of ion transport networks at each interface during the rest process, cathode can usually be used in the form of cathode sheets, and the lithium metal also can fit well with the SSE without pressure. It only needs to be assembled into a coin cell to work normally, showing greater practicality.

Based on previous research on SPEs and HSSEs, we were inspired by the research on composite electrolytes and tried to combine LIC with PEO, successfully preparing a high-performance polymer halide solid-state electrolyte. The entire preparation process is based on the solution casting method, using acetonitrile as the solvent and $LiPF_6$ as an additional electrolyte additive. The obtained LIC-PEO film has good flexibility, can withstand repeated bending by tweezers, and has an ionic conductivity of 1.19 mS cm^{-1} at 35 °C. The moisture resistance is also significantly improved compared to LIC. It can work for more than 620 h without short circuit in Li-Li symmetrical cell, XPS results show the changes in element distribution, binding energy, etc. of LIC-PEO before and after cycling. And has a capacity retention rate of 84.2% after 300 cycles at 0.2 C, and a capacity retention rate of 80.6% after 150 cycles at 1.2 C, showing good electrochemical performance. Other tests such as XRD, SEM and other tests describe surface morphology, crystal structure, activation energy and other properties of LIC-PEO. The new SSE prepared in this work has good performance, has been rarely researched before, and has great application potential.

4.2 Experimental Section

4.2.1 Preparation of Li_3InCl_6-PEO and composite cathode

The anhydrous lithium chloride (LiCl, Innochem, 99.99%) and anhydrous indium chloride ($InCl_3$, Sigma-Aldrich, 98%) were dissolved in deionized water in the ratio of 3:1 (molar ratio) and dried at 100 °C until most of the water evaporated. Finally dried under vacuum at 200 °C for 6 h to obtain Li_3InCl_6 powder.

LIC-PEO is prepared by LIC, PEO (Polyethylene oxide, Mw=6×10^5,Sigma-Aldrich) and $LiPF_6$, etc. The raw materials need to be dissolved/dispersed in anhydrous acetonitrile (CH_3CN, Sigma-Aldrich, 99.8%) solvent. The mixture was first sonicated to prevent flocculation and then stirred continuously for 24 h until completely dissolved/dispersed. The resulting viscous slurry was then cast on a PTFE plate (polytetrafluoroethylene) and further dried at 60 °C for 12 h, and finally dried under vacuum for 4 h to obtain a LIC-PEO SSE film. Each component is pre-weighed before synthesis. The amount of $LiPF_6$ in LIC-PEO is

controlled by the molar ratio of EO group (−CH_2–CH_2O−) to lithium ions at 12 h (i.e. EO /Li^+ = 12:1). The content of LIC in the LIC-PEO film was maintained at different levels in different experiments, as will be discussed later. The thickness of the LIC-PEO film is controlled by the volume of anhydrous acetonitrile and blade. It is between 20-200 μm and can be easily peeled off with tweezers, and the shape remains intact under bending. The transparency changes with the change of LIC content.

The composite cathode part was prepared by mixing NCM111 powder, super carbon 65, PVDF, LIC, and $LiPF_6$ with a weight ratio of 8:1:0.5:0.25:0.25 in N-Methyl-2-pyrrolidone (NMP), mixed evenly and cast on the aluminum foil base material, and dried at 60 °C for 24 h, and stored under appropriate conditions.

4.2.2 Characterization methods

The characterization method is the same as 3.2.2 except that BET and TGA are not included.

4.2.3 Electrochemical performance measurement

The ionic conductivity was measured using LIC-PEO films by constructing SS (stainless steel)|LIC-PEO|SS PAT-Cell. The test bench setup is shown in Fig. A4.1. And test at a frequency range between 100 mHz and 1 MHz with an amplitude of 20 mV.

The electrochemical stability of LIC-PEO was measured by linear sweep voltammetry (LSV) with the cell structure of Li/ LIC-PEO /SS PAT-Cell at the scanning rate of 1 mV s^{-1} from 2 V to 6 V.

The preparation process of Li symmetrical cells is similar, with the LIC-PEO film sandwiched between two circular lithium foils with a thickness of 60 μm and test through coin cell. LIC Li symmetrical cells were tested using a special pressurized test bench (Fig. A3.2). The experiment was performed by applying a constant current to both electrodes and then recording the voltage changes.

Li^+ transference number (t_{Li+}) were measured by applying direct current (DC) polarization at different voltages, respectively. which can be estimated by the following Equation:

$$t_{Li^+} = \frac{I_s(\Delta V - I_0 R_1^0)}{I_0(\Delta V - I_s R_1^s)}$$

The Ea was computed by the same way like section 2. Electrochemical cycling performance was determined by evaluating Li // LIC-PEO // composite NCM111 coin cells on a NEWARE BT4008 instrument in galvanostatic mode.

4.3 Results and Discussion

4.3.1 Characterization of structural of Li_3InCl_6-PEO

The preparation process of the LIC-PEO sample is shown in the Fig. 4.1a. It needs to be stirred until it is uniformly milky, then cast and dried, and finally the edges are cut and modified to obtain the final sample (Fig. 4.1b). Cut pieces of LIC-PEO can remain intact under bending (Fig. 4.1c).

According to the different amounts of PEO added (10%, 20%, 30%, 40%wt), different samples are called LIC-PEO-1, LIC-PEO-2, LIC-PEO-3, LIC-PEO-4. The phase evolution of LIC-PEO structures with different PEO contents was studied by XRD. Most of the characteristic peaks in different LIC-PEO samples can be indexed by Li_3InCl_6 (ICSD No. 89167, $C_{2/m}$). The strong characteristic peaks at 13.5°, 34.2°, 49.2°, 28.1°, 29.5°, etc. always exist, but the intensity and peak width change with the change of PEO content (Fig. 4.1d). The larger peak intensities at 28.1° and 29.5° can be attributed to the LIC and a small amount of residual LiCl[177]. But subsequent conductivity measurements proved that the residual amount is extremely small and does not affect the specific performance. As the PEO content increases, the low-intensity peak between 36°-48° gradually becomes invisible. Compared with the standard PDF, the overall pattern shifts slightly to a lower angle (Fig. 4.1e). This can be attributed to the different tensile strength and other mechanical properties of PEO and LIC[197,198]. So it is caused by the internal stress generated by the crystallized part after

forming the composite structure, it is more obvious when higher PEO content. The crystal structure of standard LIC ($C_{2/m}$ with the monoclinic rock-salt structure) is shown in Fig. A4.2. The characteristic peak at 14.2° representing the (001) plane gradually disappeared, and the peak intensity at 34.2° representing the (131) plane did not change significantly. This shows that after the addition of PEO, the (131) plane still occupies a dominant position. And the electrostatic force and the interaction force between lattices that need to be overcome for Li^+ transport are further reduced, which facilitates the transport of Li^+ and reduces the impact of PEO addition on ion conductivity[159].

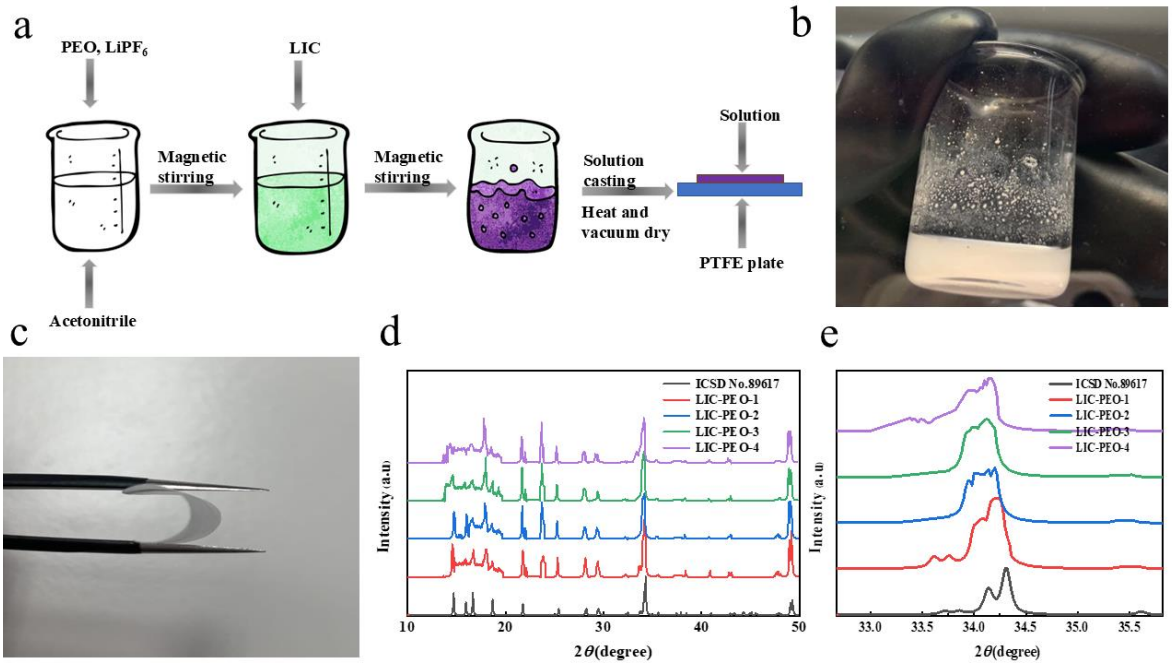

Fig. 4. 1 Synthesis process of LIC-PEO. (b) Digital photo of well-stirred precursor. (c) Bending test of LIC-ACE. (d) XRD patterns of LIC and LIC-PEO. (e) Details of the XRD pattern.

The continuous low-intensity peaks between 15° and 20° are due to the dominance of amorphous phase PEO[199]. The peaks at 17.9° and 23.9° also represent PEO[200,201]. As the PEO content increases, the peak of PEO width does not decrease, indicating that the increase in PEO crystallinity is always effectively suppressed by LIC, which contributes to the movement of PEO chain segments (Fig. A4.3)[202]. The segmental motion of the PEO chains was enhanced by LIC-PEO to help ion migration[203]. Since the XRD pattern shows the characteristics of both LIC and PEO, this indicates that the PEO has good chemical

compatibility with LIC. So during the preparation of LIC-PEO composite SSE through solution casting, no chemical reaction occurs between the two components, and the overall crystal structure does not undergo major changes, ensuring that properties such as ionic conductivity are inherited.

4.3.2 Characterization of performance of Li_3InCl_6-PEO

The ionic conductivity of LIC-PEO were measured using the impedance spectrum of the symmetrical cell of SS|LIC|SS at 35 ℃ (Fig. 4.2a). PEO-LIC-1 did not exhibit good conductivity because the lower PEO content did not improve flexibility enough, so the electrolyte could not fully fit the blocking electrode during lower pressure, and excessive LIC filling leads to uneven distribution in the PEO network, agglomeration is formed, which hinders the migration of lithium ions[204-206]. The ionic conductivity of PEO-LIC-2 has been improved, and it also shows better resilience than the PEO-LIC-1 when bent. The PEO content at this time can largely meet the low-pressure working condition, dispersion of LIC in the composite electrolyte results in multidirectional swelling of the polymer molecular chains, the swollen polymer molecular chains provide an effective channel for the Li^+ migration and a good ion transport network and corresponding framework have been roughly established[207]. LIC-PEO-3 has the highest ionic conductivity of 1.19 mS cm^{-1} (Fig. A4.4). In contrast, LIC-PEO-4 has the lowest ionic conductivity, this may be because the reduced LIC content prevents it from being evenly dispersed in the electrolyte film to form a sufficiently interconnected ion conduction channel. And more PEO content also means that has lower crystalline phase components, the working performance under 50 ℃ is reduced. Compared with PEO SSEs reported in the past, the ionic conductivity of LIC-PEO-3 at low temperatures is much higher[194,208-210]. Compared with other previous LIC SSEs projects, LIC-PEO-3 exhibits relatively high ionic conductivity, even exceeding some pure LIC (Table A4.1). Therefore, LIC-PEO-3 was used as the experimental subject in subsequent tests and simply to call it LIC-PEO.

The variation of ionic conductivity with temperature was also studied, the ionic conductivity of LIC-PEO significantly increases at high temperatures due to the frequent movement of

PEO segment in an amorphous state (Fig. 4.2b). The activation energy (Ea) is calculated from the Arrhenius plot obtained and Nyquist plots at different temperatures, the Ea of the LIC-PEO is 0.26 eV. In past reports, the Ea of LIC is usually between 0.27-0.38 eV[74,161,189,211]. The lower activation energy than LIC indicates that the Li^+ migration barrier is reduced under the synergistic effect of an appropriate amount of PEO and lithium salt. In addition, the t_{Li+} was tested by DC polarization and AC impedance before and after polarization. The result is shown in Fig. A4.5, and the calculated t_{Li+} is 0.405, which is much higher than pure PEO SPE. The ESW of the electrolyte determines whether the electrolyte can be adapted to the high-voltage cathode. In the LSV test, the oxidation current of a typical PEO electrolyte will begin to increase significantly at around 4.2 V due to violent oxidative decomposition[212,213]. LIC itself has a relatively wide ESW and has been verified to have good compatibility with most cathodes in previous studies[64]. The ESW higher than 4.2 V opens the opportunity to test innovative halide-based cathodes that work up to 4.5 V. From LSV curve, LIC PEO has higher ESW than pure chloride SSEs. When the potential is lower than 5.15 V, the current always approaches to 0, and when the potential exceeds 5.15 V, the current begins to increase, which also means that LIC-PEO begins to decompose (Fig. 4.2c). Due to the ESW of LIC-PEO measured by LSV is almost more than 5.15 V, LIC-PEO can be compatible with most high-voltage cathode. The microsurface morphology of LIC-PEO was then confirmed by SEM (Fig. 4.2d). The white LIC in the SEM mainly exists in the form of rods, most of which are more than 50 μm in length. Some are connected to each other. And evenly distributed or partially embedded on the surface of the gray PEO smooth film used as a support, it plays a good ion conduction role. The figure under higher magnification also show the tight binding of LIC to PEO. The EDX results prove that LIC not only exists in the form of rods on the surface, but is also evenly distributed inside the film, acting as part of the electrolyte filler and effectively improving the internal ion conductivity (Fig. A4.6a). A small amount of PEO is also distributed in the rod-shaped LIC to help maintain the flexibility of the surface. These factors together enable LIC-PEO to have high ionic conductivity at low pressure.

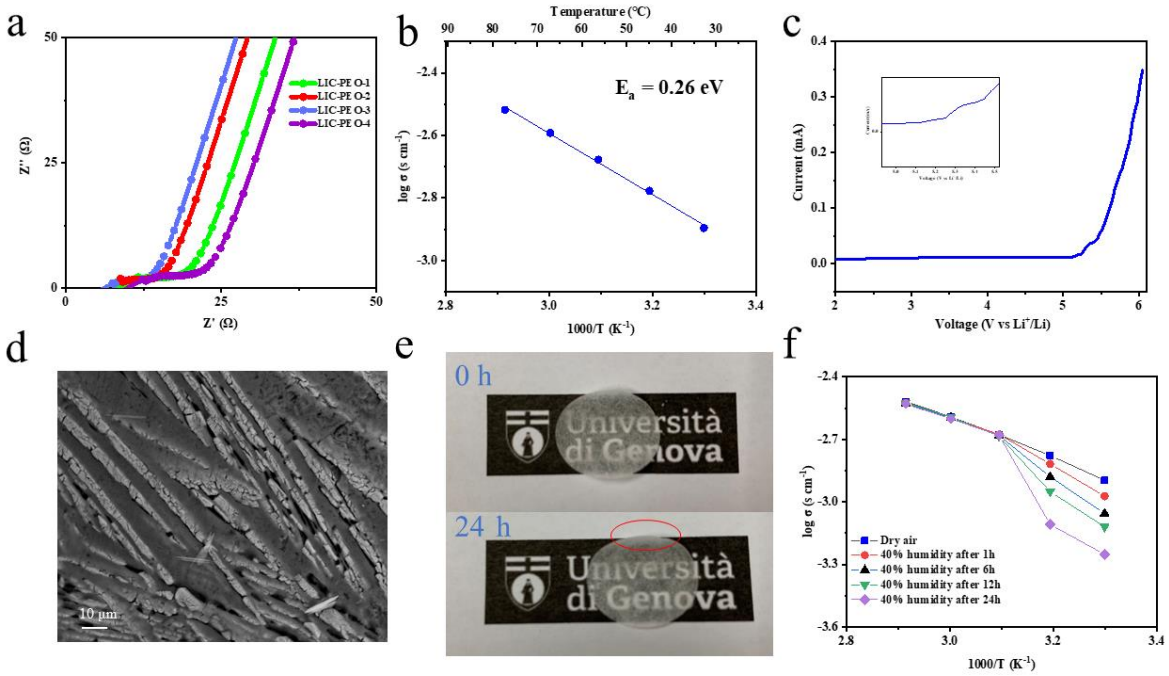

Fig. 4. 2 (a) EIS plots of LIC-PEO at 35 °C. (b) Arrhenius plot of LIC-PEO-3. (c) The electrochemical stability window of LSV curve. (d) SEM image of LIC-PEO-3. (e) Digital photo of LIC-PEO-3 before and after exposure. (f) Plot of temperature on LIC-PEO-3 hygroscopicity.

According to previous research, LIC easily absorbs moisture in humid environments to form corresponding hydrates, which leads to a reduction in ionic conductivity and changes in other properties. Therefore, we also studied the hygroscopicity of LIC-PEO. Considering that the amount of moisture absorbed by high molecular weight PEO is negligible compared with LIC, we placed LIC and LIC-PEO containing same weight of LIC at dry, 5%, 40% humidity environments at room temperature, the weight changes of these samples were recorded using an electronic balance, and the ionic conductivity was measured after different exposure times. At the same time, to facilitate the observation of changes in transparency, thinner LIC-PEO prepared by controlling conditions was used, with a thickness of 43 μm (Fig. A4.6b). When exposed to a dry environment, the weight of LIC-PEO and LIC did not change; When exposed to a 5% humidity environment, the weight of LIC-PEO and LIC initially changed slightly; when exposed to a 40% humidity environment, the weight of LIC-PEO increased significantly within the first few minutes, but was much weaker than the LIC (Fig. A4.6c). The change trend of ion conductivity is also the same as the change trend of mass. In the dry and 5% humidity environment, the ion conductivity almost does not change (±0.05 mS cm^{-1}). This may be due to deviation in EIS tests at different times. While at 40% humidity, the

ionic conductivity drops significantly, but is still better than LIC (Fig. A4.6d). The plot of Ea change with time is shown in Fig. A4.7. After being exposed to 40% humidity for 24 h at room temperature, LIC-PEO showed slight stickiness, but the light transmittance and geometric shape did not change significantly, with only a slight upwarping at the edges (Fig. 4.2e).

At the same time, to examine the effect of temperature on hygroscopicity. We also measured the weight and conductivity of LIC-PEO with different moisture levels (Exposed to the atmosphere for 1-24h) after being left at different temperatures for 1 h (Fig. 4.2f). When the temperature reached 55 °C, the moisture was completely removed from the LIC-PEO, which can be proved by the weight curve, and the similar ionic conductivity illustrates that after the moisture be removed, the good ionic conductor structure of LIC-PEO is also was restored.

The improved moisture resistance of LIC-PEO can be attributed to the fact that the addition of PEO forms a dense network structure that wraps LIC, which largely prevents the penetration of moisture. Therefore, moisture is easily removed by simple heating, and LIC-PEO can be restored to original performance. In short, these results indicate that the addition of PEO has a positive effect on improving the moisture resistance of LIC. The measurement of weight and ionic conductivity jointly prove that LIC-PEO has better resistance to humid air than LIC.

Considering the importance of symmetrical Li-Li cells for SSEs stability testing. To check the cycling and lithium deposition stability of LIC-PEO electrolyte, the symmetrical Li-Li cells were assembled for Galvanostatic cycling testing compared with LIC symmetrical Li-Li cells[214]. Before the test started, the resistance of Li/LIC-PEO/Li cell and Li/LIC/Li cell were measured respectively. Even under pressurized conditions, the resistance of LIC was still significantly higher than that of LIC-PEO, which proves that LIC-PEO has better interfacial wettability with lithium metal (Fig. A4.8). As shown in Fig 4.3a, the Li/LIC-PEO/Li cell show stable cycling over 620 h at a current density of 0.1 mA cm^{-2}. The overpotential of the Li/LIC/Li cell increases to 2 V in only 40 h. On the other hand, the overpotential of Li/LIC-PEO/Li cell only increases from 0.025 V to 0.071 V. Figure 4.3b is

a comparison of the EIS results before the start of galvanostatic cycling testing and after 620 h of testing. In the same trend as the overpotential, the resistance gradually increases, but the contour of the curve does not change significantly, which is an interface deterioration caused by normal Li plating/stripping. From the disassembled cell, it can be found that after 40 h of testing, the LIC pellet almost completely changed from white to purple-black, showing brittleness, a thick interface layer was formed on the surface, which indicates that a serious interaction between LIC and lithium metal occurred, and the trace amounts of oxygen, water and other pollutants also participate in the reaction (Fig. A4.9)[112].

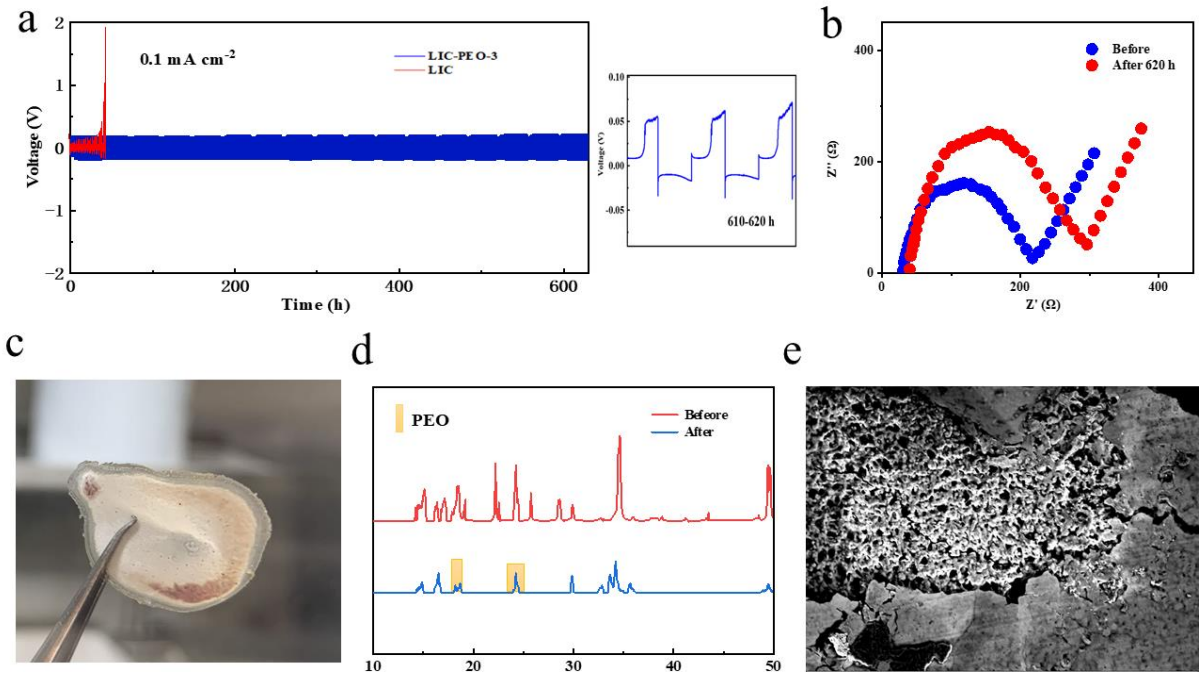

Fig. 4. 3 (a) Galvanostatic stripping/plating voltage profiles of symmetric Li |LIC-PEO| Li cell during 620 h cycling and amplified voltage profiles. (b) EIS plot of Li |LIC-PEO| Li cell at cycle 0 h and 620 h. (c) Optical images of LIC-PEO after cycling of symmetric Li-Li cell. (d) XRD pattern of LIC-PEO after cycling of symmetric Li-Li cell. (e) SEM image of LIC-PEO after cycling of symmetric Li-Li cell

But the LIC-PEO film after the 620 h test only showed an uneven and thin red-purple interface layer at the edge, and the overall state still maintained the state before the test (Fig. 4.3c). The side reaction between LIC and lithium metal has been effectively suppressed after the addition of PEO. Considering that the color of the LIC-PEO film changed after used of the symmetrical cell, the XRD measurement was performed again (Fig. 4.3d). The results showed that some characteristic peaks representing LIC and PEO still existed. However, the

overall pattern changes are more, which shows that although LIC-PEO can greatly slow down the occurrence of side reactions compared with LIC, the degradation of the interface is inevitable, especially in the repeated intercalation and de-intercalation cycle of Li^+. Some characteristic peaks with lower intensity disappeared, this may be because the amorphous byproducts produced during the operation of lithium metal and LIC-PEO increased the background noise, making it impossible to distinguish the characteristic peaks with low intensity[215]. The detailed image shows that the characteristic peaks of PEO have only changed in intensity, and no change in the number of characteristic peaks (Fig A4.10). After test, the main part of LIC-PEO still appears as a gray smooth film under SEM, the damaged part is PEO erosion caused by high-energy electron beam, and no penetration traces caused by lithium dendrites were found. After manually tearing apart part of the surface interface, the dense three-dimensional structure of LIC can be seen (Fig. 4.3e).

To further verify the changes in the composition of the pristine and used LIC-PEO samples b, we also performed XPS analysis on the pristine samples and the used samples. The spectras have been aligned on the main component of carbon for the PE/PP membrane (El-Cell FS-5P separator membrane), C-C at 285.0 eV[216,217]. Considering that LIC-PEO is in the form of a film, the composition uniformity of different parts of the pristine sample film was first verified. As shown in Figure A4.11, the XPS spectra measured at different sampling points are very similar, and further element concentration analysis also proves the uniformity of the pristine sample.

For the used samples, considering that the center part and the edge part show a large color difference, these two parts were also sampled and measured separately. Comparison between the pristine sample (red), the used sample near the edge area (green) and in the center area (blue) (Fig. 4.4a). The two used samples are more similar between each other than with the pristine sample. The main difference between the pristine sample and the used samples is a decrease in lithium from 40% to about 13%. The ratio between lithium and indium is about 26 in the case of the pristine sample. The used (edge) sample has less lithium than the Used (center) sample. The pristine sample also contains a larger amount of fluorine than the Used samples. The main differences between the two sampled areas in the used sample is

phosporus and oxygen is present in larger amount in the center area. Silicon is present in the pristine sample and is reduced or absent in the used samples. small amounts of Si can be considered as impurities introduced.

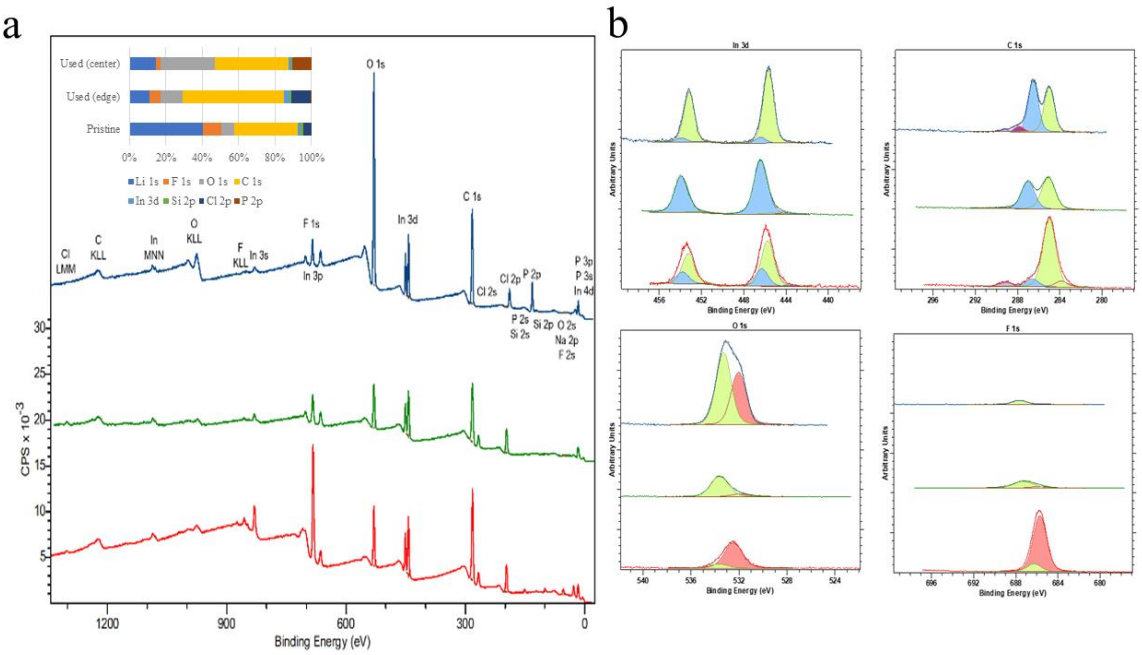

Fig. 4. 4 (a) Overall XPS spectrum of LIC-PEO pristine and used sample. (b) In 3d, C 1s, O 1s and F 1s, xps spectra of LIC-PEO pristine and used sample.

Further analysis of the characteristic peaks represented by each element as shown in Fig 4.4b. Indium is mostly In^{3+} state (green component) which may be associated with the presence of In_2O_3, Li_3O_4 (supported by the oxygen components) but is also compatible with compounds like $Li_xIn_{1-x}O_3$. A secondary component associated with $LiCl_3$ is present in the pristine and used (center) sample. This is in agreement with the larger relative amount of chlorine present in this sample. A small component at lower binding energy corresponds to indium in metallic (0) state is barely detectable.

The main component (green) of carbon at 285.0 eV is due to the C-C bond present in the PE/PP membrane (El-Cell FS-5P). A small component at lower binding energy (283.8 eV red) may be due to adventitious carbon or metallic carbides. Additional components can be found at higher binding energy and can be assigned to C-OH, C-O and PEO (286.6 eV light blue), C=O/O-C-O and O=C-O (288 eV) and O=C-O (289.1 eV, purple). Oxygen contains at

least two different species, one centered around 532.4 eV associated with O/CO_3/O-C=O and one centered around 533.6 eV which may be due to C-O/O-C=O. All of these can be attributed to PEO and the products after the reaction[218]. the main component of fluorine (red) in the pristine sample is centered at 685.7 eV and is due to LiF. Additional components at larger binding energy (686.2-686.8, green) are due to $LiPF_6$ and the various dissociation compounds $Li_xPF_yO_z$. The appearance of oxygen-containing compounds is due to the side reactions between $LiPF_6$ and the components such as PEO.

In summary, it can be inferred that the reduction in lithium content indicates that the deposition of lithium dendrites is not serious. And there is also the possibility that a certain amount of ions are lost when the used sample is stripped. The color difference in the center of the used sample can be attributed to the enrichment of oxygen and phosphorus, and the reaction with lithium. This is proved by the changes in the composition of phosphorus and oxygen. XPS results demonstrate that the element distribution and binding energy change to a certain extent before and after use. Although the side reaction between LIC-PEO and lithium metal is inevitable, it can be suppressed in long-term operation, and the performance far exceeds that of pure LIC.

The cyclic charge and discharge results under different currents are also important indicator to test the performance of SSEs. Therefore, ASSBs with LIC-PEO as electrolyte were prepared with lithium-foil anode and composite NCM111 cathode. The cells are termed Li /LIC-PEO/NCM. And the electrochemical performances were evaluated at 35 °C and 0.2 C. The Coulombic efficiency of the first cycle is 91.81% , and after first cycle are always over 99%, except for some unusual cycles (Fig 4.5a). After activation, the cell exhibited a specific discharge capacity of 152.7 mAh g^{-1} and delivered a specific discharge capacity of 128.6 mAh g^{-1} for 300 cycles with a capacity retention of 84.2% (Fig 4.5b). The EIS curves before and after cycling are shown in the figure. The bulk resistance in the high-frequency region decreases slightly after cycling. This can be attributed to the fact that cycling activates the PEO polymer chain and opens more ion channels. The interface resistance in the low-frequency region gradually increases. On the one hand, it is due to the continuous deterioration of the interface during the cycling process. On the other hand, it may be due to

the generation of a small amount of SEI. The overall resistance of LIC-PEO increased after cycling (Fig 4.5c). The LIC-PEO film after 0.2 C cycle still appears relatively smooth under SEM. However, after increasing the magnification, some obvious cracks can be found in the dense LIC structure, which also affects ion transport and further reduces the cycle performance (Fig 4.5d).

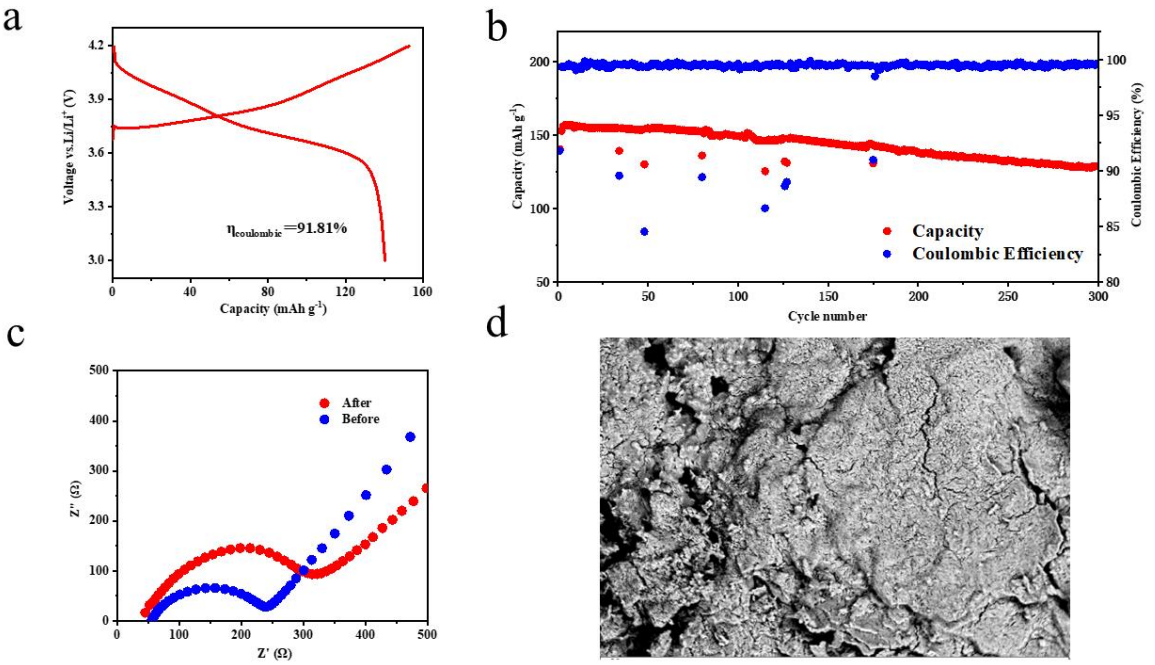

Fig. 4. 5 (a) Plot of the first charge and discharge cycle and CE. (b) Cycling performance and CE of LIC-PEO ASSB at 0.2 C. (c) EIS plot of LIC-PEO ASSB before and after cycles. (d) SEM image after 0.2 C cycle.

The Li/LIC-PEO/NCM cells also can stably cycle at 1.2 C. The Coulombic efficiency of the first cycle is 78.97% (Fig A4.12). After activation, the cell exhibited a specific discharge capacity of 100.4 mAh g-1 and delivering a specific stable capacity of 81.4 mAh g^{-1} for 150 cycles with a capacity retention of 81.1% (Fig 4.6a). Higher current density is always a challenge for ASSBs, as lithium dendrites will be more easily generated and further grow on a three-dimensional scale until a short circuit occurs. Therefore, SSEs that also act as separators must be able to resist the penetration of dendrites and inhibit their growth. After the cyclic test, the cell was disassembled and the LIC-PEO film was peeled off. Under optical photo, the flexibility of the film is reduced, the main part is still white, and some areas had silver and gray spots (Fig 4.6b). The surface is relatively rough because during long-term

high-current cycling, part of the lithium element is unevenly deposited on the surface of the film in the form of dendrites. LIC-PEO still has a capacity retention rate of more than 80% after 150 cycles at a current of 1.2 C, and no short circuit or sudden capacity drop occurred, other research on LIC SSEs has never reached the same level in the 1.2 C cycling, further demonstrating that Li/LIC-PEO/NCM cells have excellent cycling stability at high C-rates. This proves that the presence of PEO alleviates the penetration of lithium dendrites into the SSE film. Although lithium dendrites continue to grow, and LIC-PEO film is soft, but is also has sufficient toughness, the overall structure of the cell is still stable and can still conduct ions well. Although LIC itself is very hard and seems to be able to resist penetration, past studies have shown that tiny pores can also meet the passage of lithium dendrites, and the flexibility of PEO allows it to cover the surface of LIC and minimize the presence of pores[219,220]. In addition, since the layers are in very close contact after test, some damage to the surface will occur during the separation process, which also increases the roughness of the film surface. XRD measurements were performed on the LIC-PEO film before and after 1.2 C cycling (Fig 4.6c). The results showed that most of the characteristic peaks representing LIC and PEO in the XRD pattern after cycling still exist, only the intensity has changed. Among them, the favorable orientation (131) plane still dominates. The peak width of the characteristic peak representing PEO has not changed significantly compared with before the cycle, the peak intensity has only slightly decreased. Some new weak peaks can be confirmed as NCM, which may come from a small amount of powder falling off the cathode during the circulation process, it can be reduced by improving the coating process in the future. The XRD results also prove from the side that after 150 cycles at 1.2 C, the microstructure of LIC-PEO has not changed and remains stable.

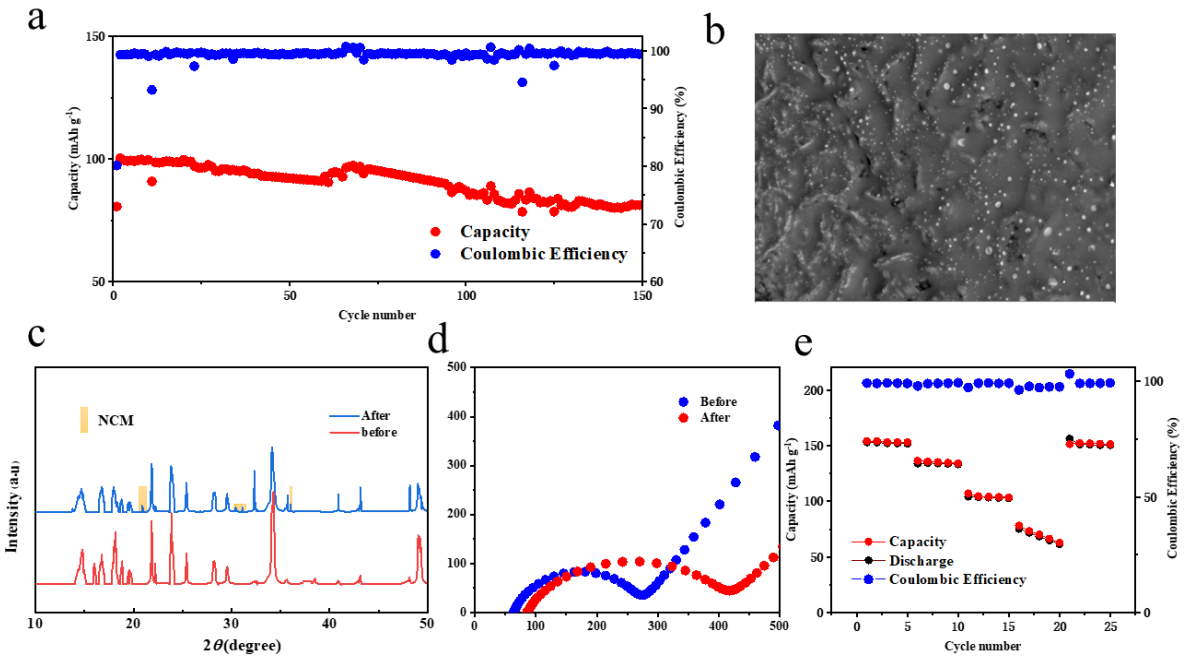

Fig. 4. 6 (a) Cycling performance and CE of LIC-PEO ASSB at 1.2 C. (b) SEM image after 1.2 C cycle. (c) XRD patterns of LIC-PEO before and after cycles at 1.2 C . (d) EIS plot of LIC-PEO ASSB before and after cycles at 1.2 C. (e) Rate capacity of LIC-PEO ASSB.

We also detected the changes in the EIS curve before and after the 1.2 C cycling. It is similar to the 0.2 C cycling (Fig 4.6d). The slight difference is that the bulk resistance in the high-frequency area increased after cycling. This may be because under thigh current, the expected activation failed to occur, and as the cycle progressed, the cell deteriorated and the overall resistance of the curve also increased. However, due to the good stability of LIC-PEO, it still performs well under high current. Compared with the LIC-PEO film after 0.2 C cycle, the film after 1.2 C cycle has higher tortuosity and lithium deposition, which can be attributed to the fact that the high current density increases the charge and discharge rate and generates more lithium dendrites. In addition, the expansion and contraction of each component are accelerated, and the film has thus become a curved shape that is more adaptable to the rapid volume change caused by expansion.

Furthermore, more measurements of rate performance details were performed, it presents the reversible specific discharge capacities of 152.9, 135.1, 105.2, and 75.3 mAh g^{-1} at 0.2 C, 0.5 C, 1 C and 2 C, respectively (Fig 4.6e). The cell still shows high specific discharge capacity

of 151.2 mAh g^{-1} when the discharge rate is reset to 0.2 C again. This proves that the cell has excellent rate performance. It can still maintain about 50% of the maximum capacity at 2 C, and restore the maximum capacity when reset to 0.2 C. This shows that the various components of the cell have intimate interface contact and a large number of conduction channels to assist ion migration at high current densities.

4.4 Conclusions

A new composite SSE containing LIC and PEO was prepared by a simple slurry casting method. Among them, PEO is a good support, with LIC evenly embedded on the surface and a certain amount of LIC distributed inside, which builds a good ion transfer network and effectively improves performance. After that, a series of tests were carried out on SSE films with different component contents to obtain the best ratio. The best LIC-PEO SSE has an ionic conductivity of 1.19 mS cm^{-1} at 35 °C, t_{Li+} is 0.405, and the electrochemical stability window of more than 5V, which is better than most SPEs at this temperature. And because of its flexibility, it can operate without strong external pressure, and its moisture resistance and stability of the metal anode have been greatly improved compared with LIC. It can work stably for more than 620 h in Li-Li symmetrical cell tests. At 35 °C, it has a capacity retention rate of 84.2% after 300 cycles at 0.2 C, this is also proved by XRD, XPS and other characterization methods. And it also has good cycle stability at 1.2 C, a capacity retention rate of 80.6% after 150 cycles. At a current density of 2 C, it can also maintain 50% of the maximum specific capacity. In summary, LIC-PEO composite SSE has good performance, and there is still much room for improvement in performance, cost, etc. Therefore, this study has great guiding significance for the design of practical ASSEs.

Annex IV

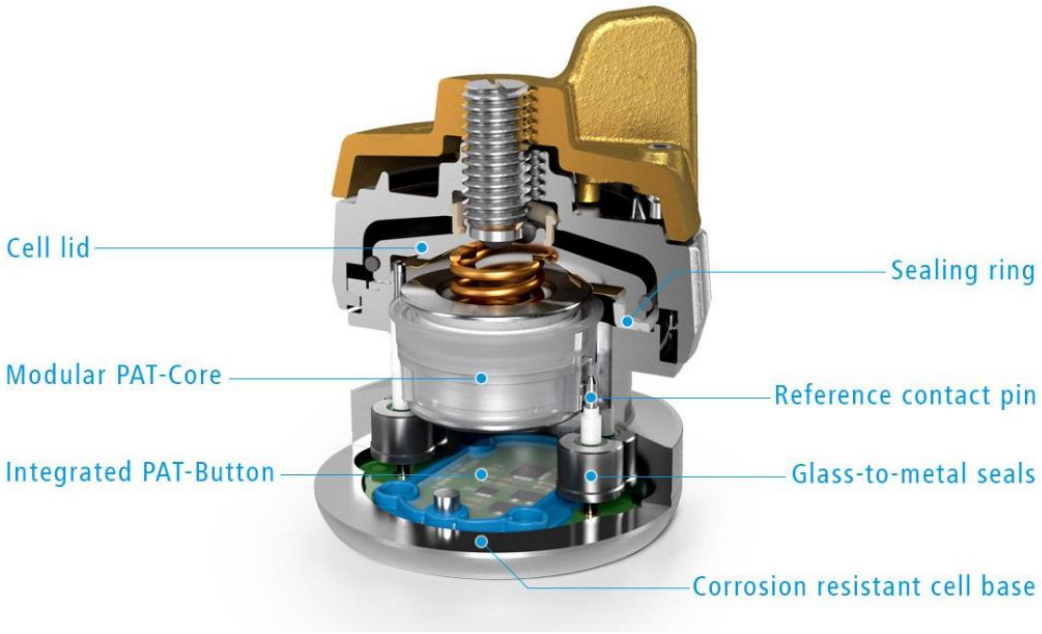

Fig. A4. 1 Structure of test bench setup for ionic conductivity.

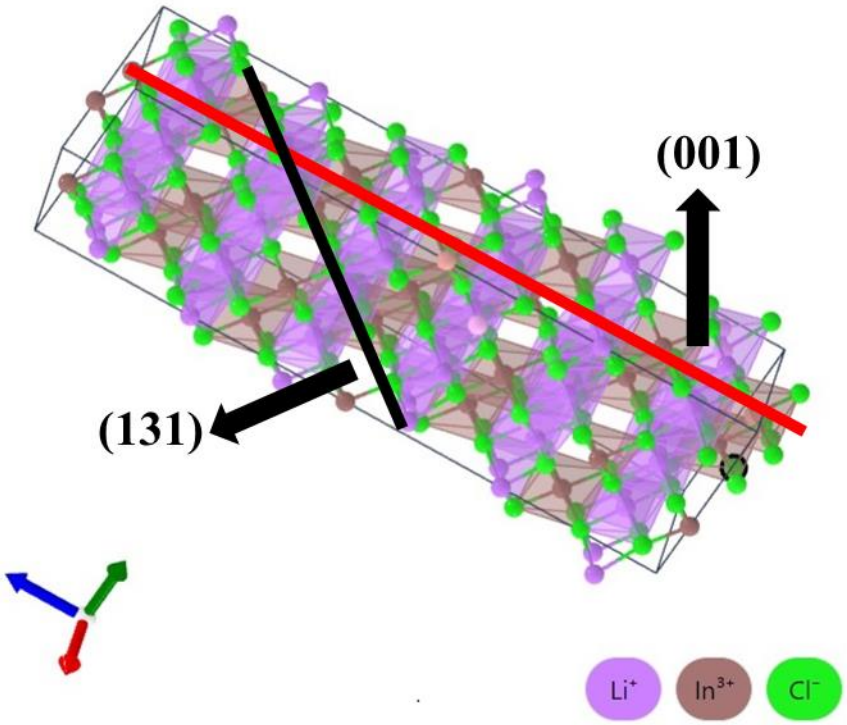

Fig. A4. 2 Crystal structure of standard LIC

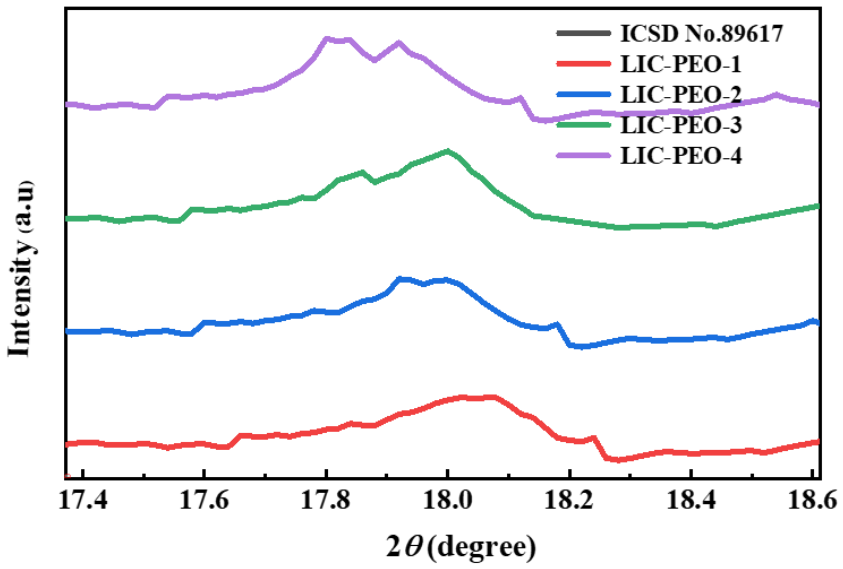

Fig. A4. 3 Partial enlargement of XRD pattern.

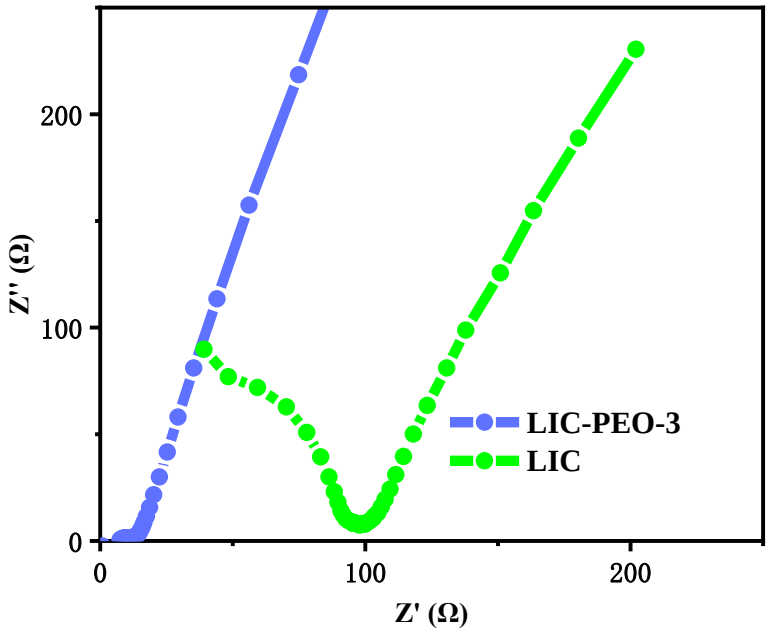

Fig. A4. 4 Comparison of ionic conductivity between LIC and LIC-PEO-3.

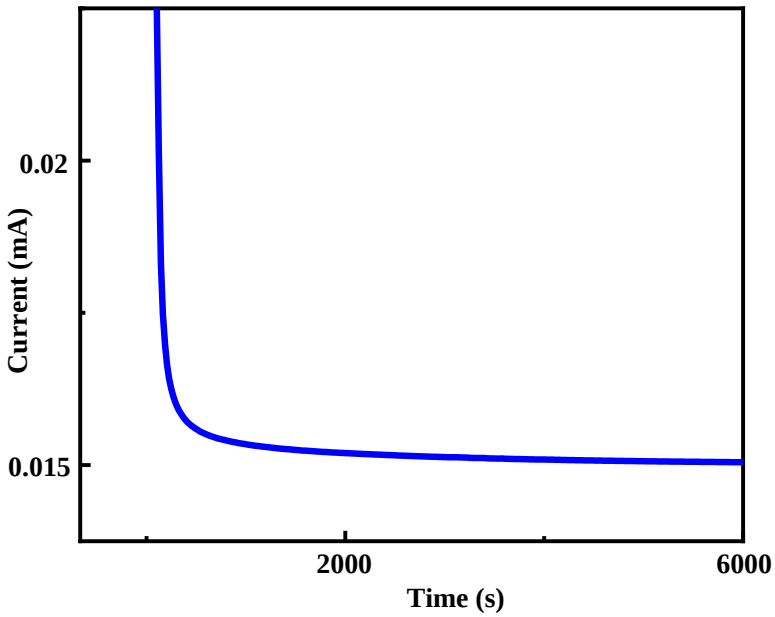

Fig. A4. 5 Li^+ transference number measurement of the LIC-PEO.

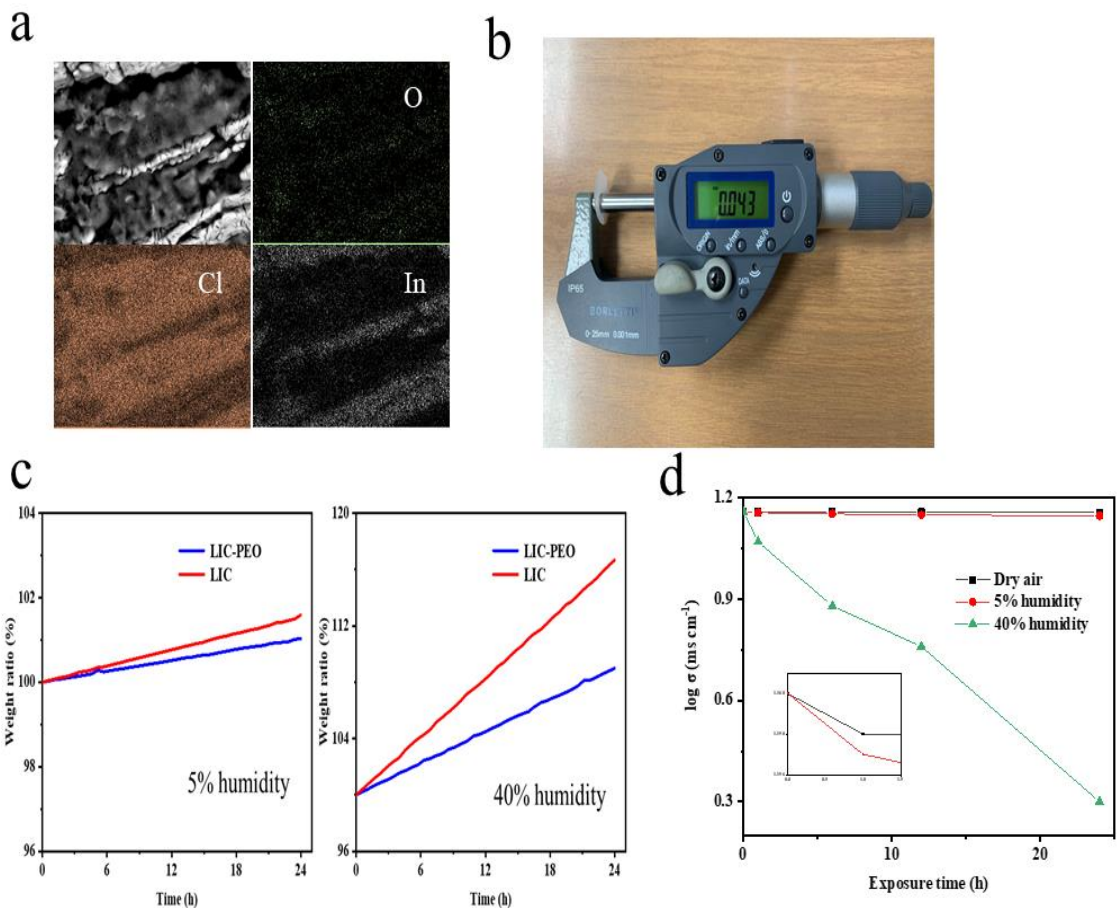

Fig. A4. 6 (a) EDX of LIC-PEO-3. (b) Measuring LIC-PEO thickness by electronic caliper. (c) Weight change at different humidity levels. (d) Plots of ionic conductivity as a function of exposure time and humidity.

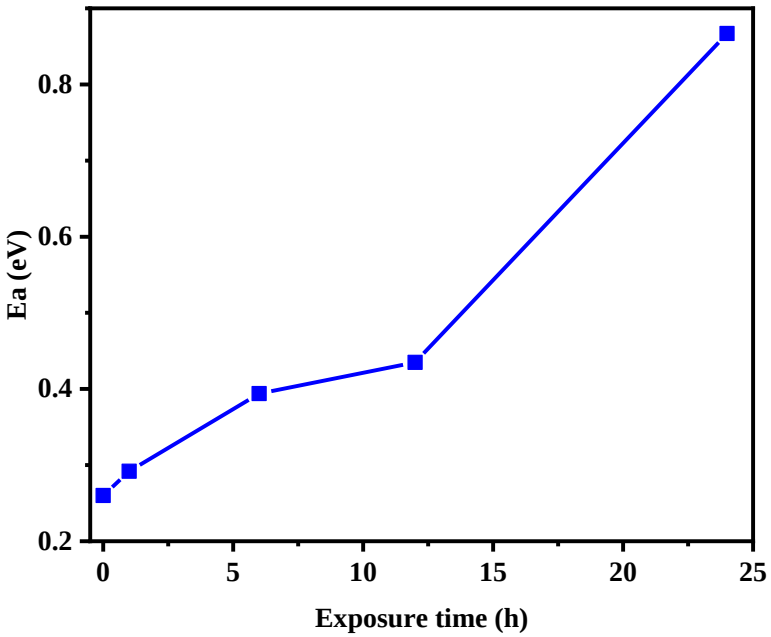

Fig. A4. 7 The plot of Ea with time.

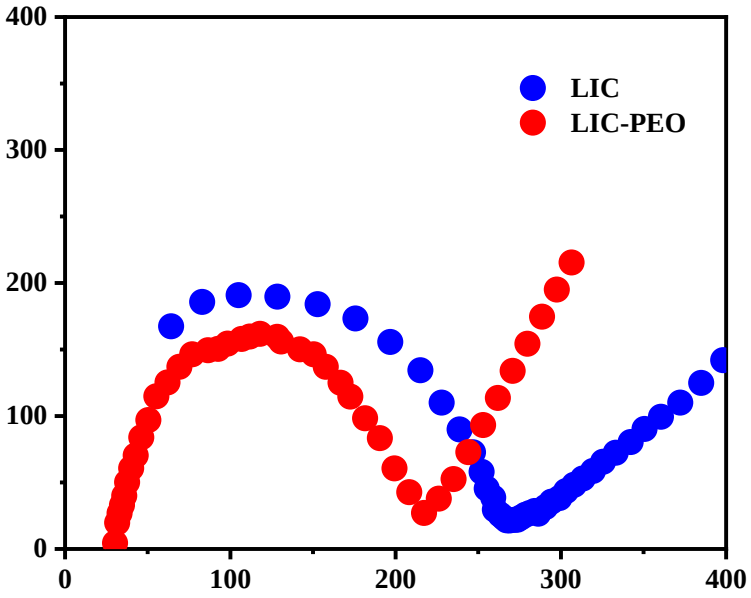

Fig. A4. 8 EIS plots of LIC and LIC-PEO in Li-Li symmetrical cell.

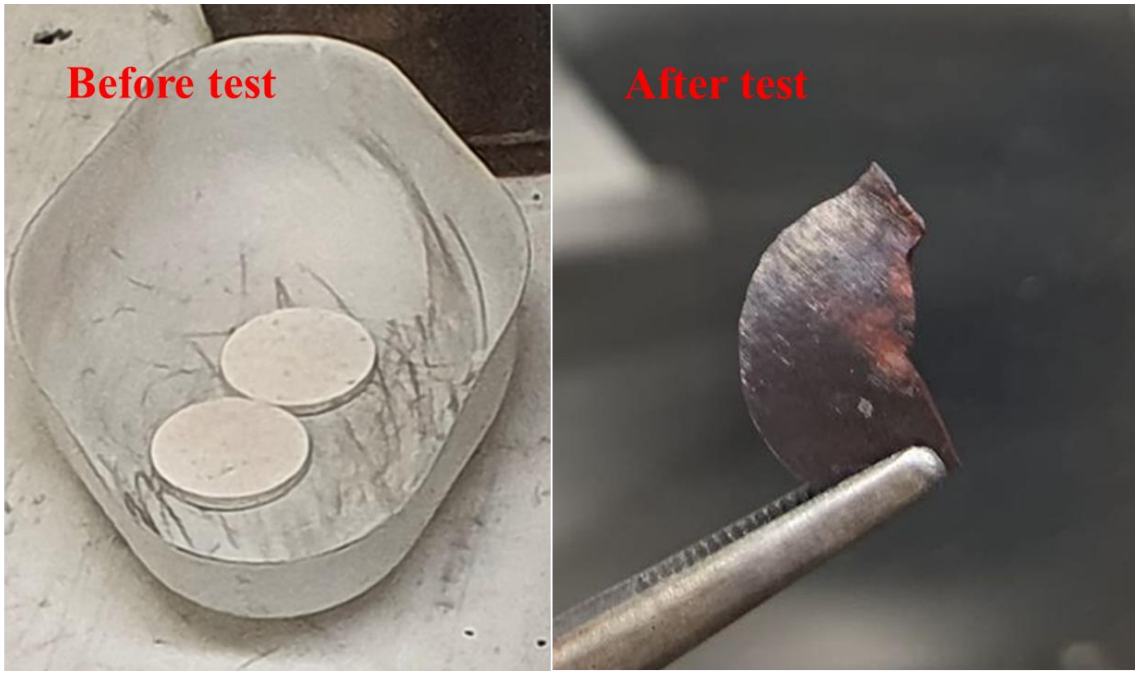

Fig. A4. 9 Digital photos of LIC pellet before and after testing.

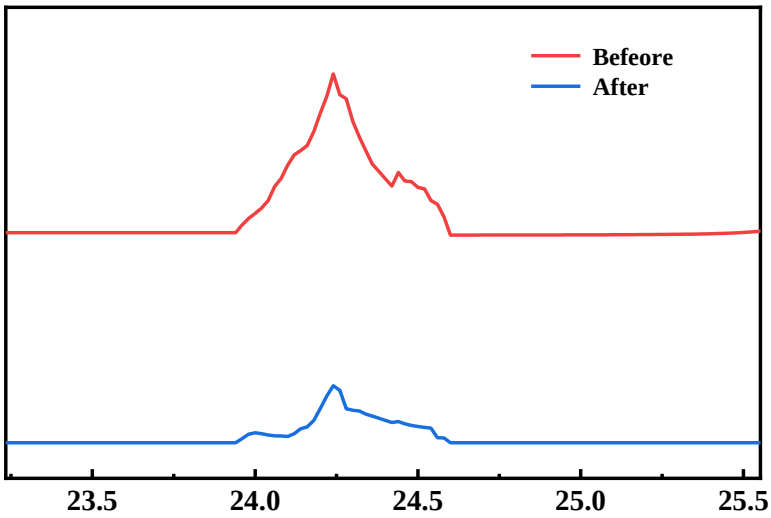

Fig. A4. 10 Partial enlargement of XRD pattern

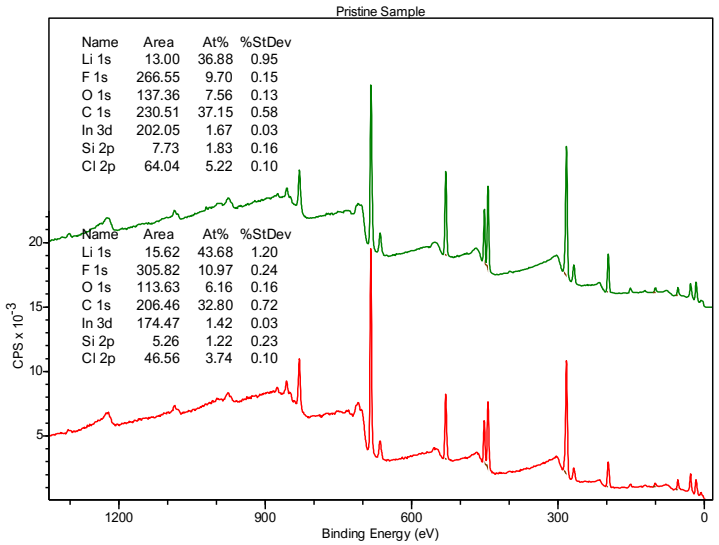

Fig. A4. 11 Overall XPS spectrum of LIC-PEO pristine sample as a homogeneity check.

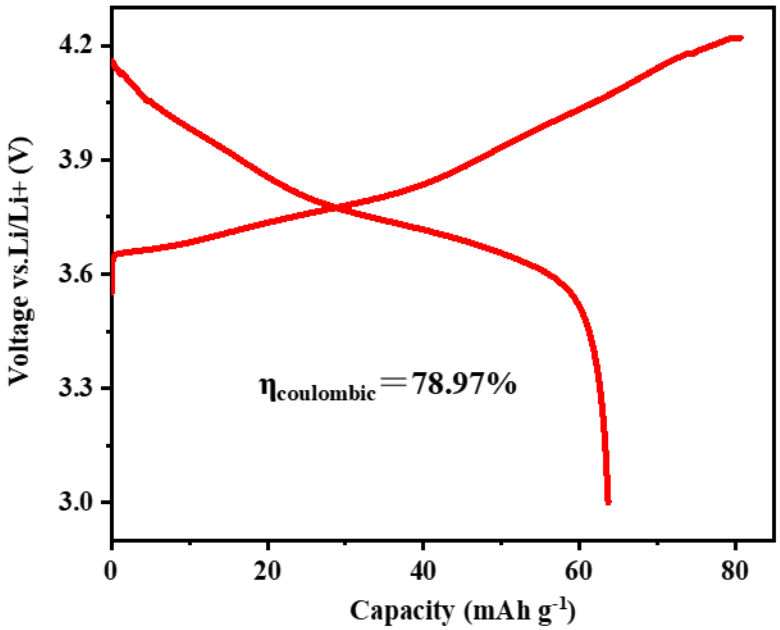

Fig. A4. 12 Plot of the first charge and discharge cycle and CE

Ref	Ionic conductivity (mS cm^{-1})
62	1.49
64	0.98
133	2.04
134	1.03
136	0.79
138	1.29
168	1.31

Table A4. 1 The comparison of Ionic conductivity of different LIC electrolytes from representative works[74,80,156,157,159,161,190].

Chapter V: Conclusion and Perspectives

This thesis focuses on the synthesis of HSSEs and their application in lithium-ion batteries. The research focuses on how to improve the efficiency of HSSEs synthesized by mechanochemical methods and simplify the application of HSSEs in LIBs.

In the first project (Chapter 2), the highlight of this part is the significant improvement in the process of mechanochemical synthesis of LIC. The focus is on studying the effects of various conditions on LIC synthesis during the ball milling process. By increasing the ball milling speed in a small amount, a 60% reduction in synthesis time was achieved, greatly improving the synthesis efficiency. The LIC synthesized by our method also has good comprehensive performance, there is only a slight increase in particle size, which does not affect subsequent applications. So it promotes the large-scale synthesis of LIC and increases the possibility of application. In future research, we hope to further improve the synthesis efficiency of LIC. At the same time, we also hope to use this method to reduce the synthesis time of other HSSEs, eliminate the application bottleneck caused by low synthesis efficiency, and thus enhance the practical potential of the entire halide SSE family.

In the second project (Chapter 3), The highlight of this part is that for the first time to prepared the flexible LIC-ACE SSE film by adding a binder, which optimized the assembly process of traditional ASSBs, reduced the proportion of powder pressing steps with low yield. And reduced the external pressure, and maintained good electrochemical performance. The main purpose is to mix LIC and EC into a flexible SSE film by a liquid phase method using acetonitrile as a solvent. The resulting product has good electrochemical properties and significantly improved moisture resistance compared to LIC. The most important thing is that it has strong flexibility and can work well under an external pressure of less than 1 MPa. Since there is still a lot of space for improvement in electrochemical performance, in future research, we hope to further improve the electrochemical properties of the product, such as ionic conductivity and cycle stability, by improving the preparation process or selecting more binders and solvents, while minimizing the pressure required to maintain during operation.

In the third project (Chapter 4), The highlight of this part is the study of the flexible LIC-Based SSE film based on the second project. It mainly refers to the concept of composite SSE in past research. Innovatively combines PEO and LIC, prepares a LIC-PEO composite SSE with good mechanical performance and electrochemical properties. The project has good originality. It is a important research to compound halides and polymers, and the gains have both the advantages of the two. After assembly to ASSB, it shows the advantages such as no apply pressure, wide ESW, high cycle stability, good rate performance etc.. And also have good moisture resistance. The most important thing is that it can be operated at a temperature slightly higher than room temperature, avoiding the inconvenience that SPEs always needs to be operated at high temperature in most cases. Since low-temperature performance always plagues the practical application of composite electrolytes. In future research, we hope to improve the low-temperature performance of halide composite electrolytes by screening and modifying polymers so that they can cope with all-weather conditions.

Reference

[1] Lanzafame P, Abate S, Ampelli C, et al. Beyond Solar Fuels: Renewable Energy-Driven Chemistry[J]. ChemSusChem: 2017, 10(22): 4409-4419.

[2] Harfoot M B, Tittensor D P, Knight S, et al. Present and future biodiversity risks from fossil fuel exploitation[J]. Conservation Letters: 2018, 11(4): e12448.

[3] Hassan Q, Algburi S, Sameen A Z, et al. A comprehensive review of international renewable energy growth[J]. Energy and Built Environment: 2024:

[4] Wang F, Harindintwali J D, Yuan Z, et al. Technologies and perspectives for achieving carbon neutrality[J]. The Innovation: 2021, 2(4):

[5] Kabir E, Kumar P, Kumar S, et al. Solar energy: Potential and future prospects[J]. Renewable and Sustainable Energy Reviews: 2018, 82: 894-900.

[6] Olabi A G, Mahmoud M, Soudan B, et al. Geothermal based hybrid energy systems, toward eco-friendly energy approaches[J]. Renewable Energy: 2020, 147: 2003-2012.

[7] Veers P, Dykes K, Lantz E, et al. Grand challenges in the science of wind energy[J]. Science: 2019, 366(6464):

[8] Liu Z, Hao H, Cheng X, et al. Critical issues of energy efficient and new energy vehicles development in China[J]. Energy Policy: 2018, 115: 92-97.

[9] Li M, Lu J, Chen Z, et al. 30 years of lithium-ion batteries[J]. Advanced Materials: 2018, 30(33): 1800561.

[10] Delmas C. Sodium and sodium-ion batteries: 50 years of research[J]. Advanced Energy Materials: 2018, 8(17): 1703137.

[11] Olabi A, Wilberforce T, Abdelkareem M A. Fuel cell application in the automotive industry and future perspective[J]. Energy: 2021, 214: 118955.

[12] Wu F, Maier J, Yu Y. Guidelines and trends for next-generation rechargeable lithium and lithium-ion batteries[J]. Chemical Society Reviews: 2020, 49(5): 1569-1614.

[13] Tarascon J-M, Armand M. Issues and challenges facing rechargeable lithium batteries[J]. nature: 2001, 414(6861): 359-367.

[14] Zubi G, Dufo-López R, Carvalho M, et al. The lithium-ion battery: State of the art and future perspectives[J]. Renewable and Sustainable Energy Reviews: 2018, 89: 292-308.

[15] Da Silva F S, de Souza T M. Novel materials for solid oxide fuel cell technologies: A literature review[J]. international journal of hydrogen energy: 2017, 42(41): 26020-26036.

[16] Wang Q, Jiang L, Yu Y, et al. Progress of enhancing the safety of lithium ion battery from the electrolyte aspect[J]. Nano Energy: 2019, 55: 93-114.

[17] Wakihara M. Recent developments in lithium ion batteries[J]. Materials Science and Engineering: R: Reports: 2001, 33(4): 109-134.

[18] Lyu Y, Wu X, Wang K, et al. An overview on the advances of $LiCoO_2$ cathodes for lithium-ion batteries[J]. Advanced Energy Materials: 2021, 11(2): 2000982.

[19] Scrosati B. History of lithium batteries[J]. Journal of solid state electrochemistry: 2011, 15(7): 1623-1630.

[20] Kim T, Song W, Son D-Y, et al. Lithium-ion batteries: outlook on present, future, and hybridized technologies[J]. Journal of materials chemistry A: 2019, 7(7): 2942-2964.

[21] Evarts E C. Lithium batteries: to the limits of lithium[J]. Nature: 2015, 526(7575): S93-S95.
[22] Dias F B, Plomp L, Veldhuis J B. Trends in polymer electrolytes for secondary lithium batteries[J]. Journal of Power Sources: 2000, 88(2): 169-191.
[23] Xu K. Nonaqueous liquid electrolytes for lithium-based rechargeable batteries[J]. Chemical reviews: 2004, 104(10): 4303-4418.
[24] Huang X. Separator technologies for lithium-ion batteries[J]. Journal of Solid State Electrochemistry: 2011, 15(4): 649-662.
[25] Zheng F, Kotobuki M, Song S, et al. Review on solid electrolytes for all-solid-state lithium-ion batteries[J]. Journal of Power Sources: 2018, 389: 198-213.
[26] Sun C, Liu J, Gong Y, et al. Recent advances in all-solid-state rechargeable lithium batteries[J]. Nano Energy: 2017, 33: 363-386.
[27] Zhang T, He W, Zhang W, et al. Designing composite solid-state electrolytes for high performance lithium ion or lithium metal batteries[J]. Chemical Science: 2020, 11(33): 8686-8707.
[28] Chen J, Wu J, Wang X, et al. Research Progress and Application Prospect of Solid-state Electrolytes in Commercial Lithium-ion Power Batteries[J]. Energy Storage Materials: 2020:
[29] Yao X, Huang B, Yin J, et al. All-solid-state lithium batteries with inorganic solid electrolytes: Review of fundamental science[J]. Chinese Physics B: 2015, 25(1): 018802.
[30] Kennedy J H, Miles R, Hunter J. Solid electrolyte properties and crystal forms of lead fluoride[J]. Journal of The Electrochemical Society: 1973, 120(11): 1441.
[31] Hebb M H. Electrical conductivity of silver sulfide[J]. The journal of chemical physics: 1952, 20(1): 185-190.
[32] Reddy M V, Julien C M, Mauger A, et al. Sulfide and oxide inorganic solid electrolytes for all-solid-state Li batteries: A Review[J]. Nanomaterials: 2020, 10(8): 1606.
[33] Sakuda A, Hayashi A, Tatsumisago M. Sulfide solid electrolyte with favorable mechanical property for all-solid-state lithium battery[J]. Scientific reports: 2013, 3(1): 1-5.
[34] Zhao Q, Stalin S, Zhao C-Z, et al. Designing solid-state electrolytes for safe, energy-dense batteries[J]. Nature Reviews Materials: 2020, 5(3): 229-252.
[35] Isikli S, Ryan K M. Recent advances in solid-state polymer electrolytes and innovative ionic liquids based polymer electrolyte systems[J]. Current Opinion in Electrochemistry: 2020, 21: 188-191.
[36] Cui Y, Wan J, Ye Y, et al. A fireproof, lightweight, polymer–polymer solid-state electrolyte for safe lithium batteries[J]. Nano letters: 2020, 20(3): 1686-1692.
[37] Armand M. Polymer solid electrolytes-an overview[J]. Solid State Ionics: 1983, 9: 745-754.
[38] Di Noto V, Lavina S, Giffin G A, et al. "Polymer electrolytes: Present, past and future," vol. 57: Elsevier, 2011, pp. 4-13.
[39] Sequeira C, Santos D. Polymer electrolytes: fundamentals and applications[M]. Elsevier, 2010:

[40] Campanella D, Belanger D, Paolella A. Beyond garnets, phosphates and phosphosulfides solid electrolytes: New ceramic perspectives for all solid lithium metal batteries[J]. Journal of Power Sources: 2021, 482: 228949.
[41] Duchêne L, Remhof A, Hagemann H, et al. Status and prospects of hydroborate electrolytes for all-solid-state batteries[J]. Energy Storage Materials: 2020, 25: 782-794.
[42] Zhao R, Wu Y, Liang Z, et al. Metal–organic frameworks for solid-state electrolytes[J]. Energy & Environmental Science: 2020, 13(8): 2386-2403.
[43] Mei H-x, Piccardo P, Cingolani A, et al. Unconventional solid-state electrolytes for lithium-based batteries: Recent advances and challenges[J]. Journal of Power Sources: 2023, 553: 232257.
[44] Wang H, Sheng L, Yasin G, et al. Reviewing the current status and development of polymer electrolytes for solid-state lithium batteries[J]. Energy Storage Materials: 2020, 33: 188-215.
[45] Seol J-c, Balasubramaniam R, Aravindan V, et al. Ameliorating the electrode/electrolyte interface compatibility in Li-ion solid-state batteries with plasticizer[J]. Journal of Alloys and Compounds: 2022, 927: 167077.
[46] Subramani R, Tseng Y-H, Lee Y-L, et al. High Li^+ transference gel interface between solid-oxide electrolyte and cathode for quasi-solid lithium-ion batteries[J]. Journal of materials chemistry A: 2019, 7(19): 12244-12252.
[47] Chang Z, Yang H, Zhu X, et al. A stable quasi-solid electrolyte improves the safe operation of highly efficient lithium-metal pouch cells in harsh environments[J]. Nature Communications: 2022, 13(1): 1510.
[48] Lu Q, Wang C, Bao D, et al. High-Performance Quasi-Solid-State Pouch Cells Enabled by in situ Solidification of a Novel Polymer Electrolyte[J]. Energy & Environmental Materials: 2023, 6(4): e12447.
[49] Bertasi F, Pagot G, Vezzù K, et al. Exotic solid state ion conductor from fluorinated titanium oxide and molten metallic lithium[J]. Journal of Power Sources: 2018, 400: 16-22.
[50] Bertasi F, Vezzù K, Giffin G A, et al. Single-ion-conducting nanocomposite polymer electrolytes based on PEG400 and anionic nanoparticles: Part 2. Electrical characterization[J]. International journal of hydrogen energy: 2014, 39(6): 2884-2895.
[51] Bertasi F, Vezzù K, Negro E, et al. Single-ion-conducting nanocomposite polymer electrolytes based on PEG400 and anionic nanoparticles: Part 1. Synthesis, structure and properties[J]. International journal of hydrogen energy: 2014, 39(6): 2872-2883.
[52] Ginnings D, Phipps T. Temperature-conductance curves of solid salts. III. Halides of Lithium[J]. Journal of the American Chemical Society: 1930, 52(4): 1340-1345.
[53] Hartwig P, Weppner W, Wichelhaus W. Fast ionic lithium conduction in solid lithium nitride chloride[J]. Materials Research Bulletin: 1979, 14(4): 493-498.
[54] Kanno R, Takeda Y, Yamamoto O. Structure, ionic conductivity and phase transformation of double chloride spinels[J]. Solid State Ionics: 1988, 28: 1276-1281.
[55] Tomita Y, Ohki H, Yamada K, et al. Ionic conductivity and structure of halocomplex salts of group 13 elements[J]. Solid State Ionics: 2000, 136: 351-355.
[56] Steiner H J, Lutz H. Neue schnelle Ionenleiter vom Typ M MIIICl6 (MI= Li, Na, Ag; MIII= In, Y)[J]. Zeitschrift für anorganische und allgemeine Chemie: 1992, 613(7): 26-30.

[57] Bohnsack A, Stenzel F, Zajonc A, et al. Ternäre Halogenide vom Typ A_3MX_6. VI [1]. Ternäre Chloride der Selten-Erd-Elemente mit Lithium, Li_3MCl_6 (M Tb Lu, Y, Sc): Synthese, Kristallstrukturen und Ionenbewegung[J]. Zeitschrift für anorganische und allgemeine Chemie: 1997, 623(7): 1067-1073.

[58] Tomita Y, Matsushita H, Kobayashi K, et al. Substitution effect of ionic conductivity in lithium ion conductor, $Li_3InBr_{6-x}Cl_x$[J]. Solid State Ionics: 2008, 179(21-26): 867-870.

[59] Yamada K, Iwaki K, Okuda T, et al. "Impedance Spectroscopy and Structural Investigation of Li^+ Conductor Li_3InBr_6," in *Solid State Ionics: Trends in the New Millennium*: World Scientific, 2002, pp. 621-628.

[60] Spector J, Villeneuve G, Hanebali L, et al. NMR Investigations of the Li+ ion mobility in the double chlorides Li_2MgCl_4 and $LiMgCl_3$[J]. Materials Letters: 1982, 1(2): 43-48.

[61] Asano T, Sakai A, Ouchi S, et al. Solid Halide Electrolytes with High Lithium-Ion Conductivity for Application in 4 V Class Bulk-Type All-Solid-State Batteries[J]. Advanced Materials: 2018, 30(44): 1803075.

[62] Schnell J, Günther T, Knoche T, et al. All-solid-state lithium-ion and lithium metal batteries–paving the way to large-scale production[J]. Journal of Power Sources: 2018, 382: 160-175.

[63] Yu C, Li Y, Adair K R, et al. Tuning ionic conductivity and electrode compatibility of Li3YBr6 for high-performance all solid-state Li batteries[J]. Nano Energy: 2020, 77: 105097.

[64] Wang S, Bai Q, Nolan A M, et al. Lithium Chlorides and Bromides as Promising Solid - State Chemistries for Fast Ion Conductors with Good Electrochemical Stability[J]. Angewandte Chemie International Edition: 2019, 58(24): 8039-8043.

[65] Fu Y, Ma C. Interplay between Li_3YX_6 (X= Cl or Br) solid electrolytes and the Li metal anode[J]. Science China Materials: 2021: 1-8.

[66] Muy S, Voss J, Schlem R, et al. High-throughput screening of solid-state Li-ion conductors using lattice-dynamics descriptors[J]. Iscience: 2019, 16: 270-282.

[67] Schlem R, Muy S, Prinz N, et al. Mechanochemical synthesis: a tool to tune cation site disorder and ionic transport properties of Li_3MCl_6 (M= Y, Er) superionic conductors[J]. Advanced Energy Materials: 2020, 10(6): 1903719.

[68] Li X, Liang J, Yang X, et al. Progress and Perspectives for Halide Solid-State Electrolyte for All-Solid-State Lithium Batteries[J]. Energy: 2018, 11(4): 719-1000.

[69] Liang J, Li X, Wang S, et al. Site-Occupation-Tuned Superionic Li_xScCl_{3+x} Halide Solid Electrolytes for All-Solid-State Batteries[J]. Journal of the American Chemical Society: 2020, 142(15): 7012-7022.

[70] Tanibata N, Takimoto S, Nakano K, et al. Metastable Chloride Solid Electrolyte with High Formability for Rechargeable All-Solid-State Lithium Metal Batteries[J]. ACS Materials Letters: 2020, 2(8): 880-886.

[71] Liu Q, Geng Z, Han C, et al. Challenges and perspectives of garnet solid electrolytes for all solid-state lithium batteries[J]. Journal of Power Sources: 2018, 389: 120-134.

[72] Banerjee A, Wang X, Fang C, et al. Interfaces and interphases in All-Solid-State batteries with inorganic solid electrolytes[J]. Chemical reviews: 2020, 120(14): 6878-6933.

[73] DeWees R, Wang H. Synthesis and Properties of NASICON-type LATP and LAGP Solid Electrolytes[J]. ChemSusChem: 2019, 12(16): 3713-3725.
[74] Li X, Liang J, Luo J, et al. Air-stable Li_3InCl_6 electrolyte with high voltage compatibility for all-solid-state batteries[J]. Energy & Environmental Science: 2019, 12(9): 2665-2671.
[75] Li W J, Hirayama M, Suzuki K, et al. Fabrication and electrochemical properties of a $LiCoO_2$ and $Li_{10}GeP_2S_{12}$ composite electrode for use in all-solid-state batteries[J]. Solid State Ionics: 2016, 285: 136-142.
[76] Gombotz M, Wilkening H M R. Fast Li Ion Dynamics in the Mechanosynthesized Nanostructured Form of the Solid Electrolyte Li_3YBr_6[J]. ACS Sustainable Chemistry & Engineering: 2020:
[77] Wang S, Xu X, Cui C, et al. Air sensitivity and degradation evolution of halide solid state electrolytes upon exposure[J]. Advanced Functional Materials: 2022, 32(7): 2108805.
[78] Deng S, Jiang M, Rao A, et al. Fast-Charging Halide-Based All-Solid-State Batteries by Manipulation of Current Collector Interface[J]. Advanced Functional Materials: 2022: 2200767.
[79] Xie M, Hu T, Yang L, et al. Synthesis of high-voltage (4.7 V) $LiCoO_2$ cathode materials with Al doping and conformal Al_2O_3 coating by atomic layer deposition[J]. RSC advances: 2016, 6(68): 63250-63255.
[80] Li X, Liang J, Chen N, et al. Water-mediated synthesis of a superionic halide solid electrolyte[J]. Angewandte Chemie: 2019, 131(46): 16579-16584.
[81] Li X, Liang J, Adair K R, et al. Origin of Superionic $Li_3Y_{1-x}In_xCl_6$ Halide Solid Electrolytes with High Humidity Tolerance[J]. Nano letters: 2020, 20(6): 4384-4392.
[82] Kartzmark E M. Double salts of indium trichloride with the alkali chlorides, with ammonium chloride, and with indium sulfate[J]. Canadian Journal of Chemistry: 1977, 55(15): 2792-2798.
[83] Liu Z, Ma S, Liu J, et al. High Ionic Conductivity Achieved in $Li_3Y(Br_3Cl_3)$ Mixed Halide Solid Electrolyte via Promoted Diffusion Pathways and Enhanced Grain Boundary[J]. ACS Energy Letters: 2020, 6: 298-304.
[84] Taylor S. Abundance of chemical elements in the continental crust: a new table[J]. Geochimica et cosmochimica acta: 1964, 28(8): 1273-1285.
[85] Innocenzi V, De Michelis I, Kopacek B, et al. Yttrium recovery from primary and secondary sources: A review of main hydrometallurgical processes[J]. Waste management: 2014, 34(7): 1237-1250.
[86] Wang K, Ren Q, Gu Z, et al. A cost-effective and humidity-tolerant chloride solid electrolyte for lithium batteries[J]. Nature Communications: 2021, 12(1): 1-11.
[87] Park K-H, Kaup K, Assoud A, et al. High-voltage superionic halide solid electrolytes for all-solid-state Li-ion batteries[J]. ACS Energy Letters: 2020, 5(2): 533-539.
[88] Kwak H, Han D, Lyoo J, et al. New Cost-Effective Halide Solid Electrolytes for All-Solid-State Batteries: Mechanochemically Prepared Fe^{3+}-Substituted Li_2ZrCl_6[J]. Advanced Energy Materials: 2021: 2003190.
[89] Zhu Y, Mo Y. Materials Design Principles for Air-Stable Lithium/Sodium Solid Electrolytes[J]. Angewandte Chemie International Edition: 2020, 59(40): 17472-17476.

[90] Li F, Cheng X, Lu L-L, et al. Stable All-Solid-State Lithium Metal Batteries Enabled by Machine Learning Simulation Designed Halide Electrolytes[J]. Nano Letters: 2022, 22(6): 2461-2469.
[91] Wang Y, Seo B, Wang B, et al. Fundamentals, materials, and machine learning of polymer electrolyte membrane fuel cell technology[J]. Energy and AI: 2020, 1: 100014.
[92] Chen Y-T, Duquesnoy M, Tan D H, et al. Fabrication of high-quality thin solid-state electrolyte films assisted by machine learning[J]. ACS Energy Letters: 2021, 6(4): 1639-1648.
[93] Aykol M, Herring P, Anapolsky A. Machine learning for continuous innovation in battery technologies[J]. Nature Reviews Materials: 2020, 5(10): 725-727.
[94] Guo H, Wang Q, Stuke A, et al. Accelerated atomistic modeling of solid-state battery materials with machine learning[J]. Frontiers in Energy Research: 2021, 9: 695902.
[95] Strock L W. Kristallstruktur des hochtemperatur-jodsilbers a-AgJ[J]. Zeitschrift für Physikalische Chemie: 1934, 25(1): 441-459.
[96] Bo S-H, Wang Y, Kim J C, et al. Computational and experimental investigations of Na-ion conduction in cubic Na3PSe4[J]. Chemistry of Materials: 2016, 28(1): 252-258.
[97] Kuhn A, Narayanan S, Spencer L, et al. Li self-diffusion in garnet-type $Li_7La_3Zr_2O_{12}$ as probed directly by diffusion-induced Li 7 spin-lattice relaxation NMR spectroscopy[J]. Physical Review B: 2011, 83(9): 094302.
[98] Kuhn A, Kunze M, Sreeraj P, et al. NMR relaxometry as a versatile tool to study Li ion dynamics in potential battery materials[J]. Solid state nuclear magnetic resonance: 2012, 42: 2-8.
[99] Zhang B, Zhong J, Zhang Y, et al. Discovering a New class of fluoride solid-electrolyte materials via screening the structural property of Li-ion sublattice[J]. Nano Energy: 2021, 79: 105407.
[100] Schlem R, Bernges T, Li C, et al. Lattice Dynamical Approach for Finding the Lithium Superionic Conductor Li_3ErI_6[J]. ACS Applied Energy Materials: 2020, 3(4): 3684-3691.
[101] Xu Z, Chen X, Liu K, et al. Influence of anion charge on Li ion diffusion in a new solid-state electrolyte, Li_3LaI_6[J]. Chemistry of Materials: 2019, 31(18): 7425-7433.
[102] Bertasi F, Pagot G, Vezzù K, et al. Lithiated nanoparticles doped with ionic liquids as quasi-solid electrolytes for lithium batteries[J]. Electrochimica Acta: 2019, 307: 51-63.
[103] Li C, Gu L, Tsukimoto S, et al. Low-Temperature Ionic-Liquid-Based Synthesis of Nanostructured Iron-Based Fluoride Cathodes for Lithium Batteries[J]. Advanced Materials: 2010, 22(33): 3650-3654.
[104] Plass M A, Bette S, Dinnebier R E, et al. Enhancement of Superionic Conductivity by Halide Substitution in Strongly Stacking Faulted $Li_3HoBr_{6-x}I_x$ Phases[J]. Chemistry of Materials: 2022:
[105] Jiang M, Mukherjee S, Chen Z W, et al. Materials perspective on new lithium chlorides and bromides: insights into thermo-physical properties[J]. Physical Chemistry Chemical Physics: 2020, 22(39): 22758-22767.
[106] Yu S, Schmidt R D, Garcia-Mendez R, et al. Elastic properties of the solid electrolyte $Li_7La_3Zr_2O_{12}$ (LLZO)[J]. Chemistry of Materials: 2016, 28(1): 197-206.

[107] Ni J E, Case E D, Sakamoto J S, et al. Room temperature elastic moduli and Vickers hardness of hot-pressed LLZO cubic garnet[J]. Journal of Materials Science: 2012, 47(23): 7978-7985.
[108] Monroe C, Newman J. The impact of elastic deformation on deposition kinetics at lithium/polymer interfaces[J]. Journal of The Electrochemical Society: 2005, 152(2): A396.
[109] Ke X, Wang Y, Ren G, et al. Towards rational mechanical design of inorganic solid electrolytes for all-solid-state lithium ion batteries[J]. Energy Storage Materials: 2020, 26: 313-324.
[110] Xiao H, Jiang M, Zhao F, et al. Thermal and mechanical stability, electronic structure and energetic properties of Pu-containing pyrochlores: $La_{2-y}Pu_yZr_2O_7$ and $La_2Zr_{2-y}Pu_yO_7$ ($0 \leqslant y \leqslant 2$)[J]. Journal of Nuclear Materials: 2015, 466: 162-171.
[111] Pugh S. XCII. Relations between the elastic moduli and the plastic properties of polycrystalline pure metals[J]. The London, Edinburgh, and Dublin Philosophical Magazine and Journal of Science: 1954, 45(367): 823-843.
[112] Riegger L M, Schlem R, Sann J, et al. Lithium - metal anode instability of the superionic halide solid electrolytes and the implications for solid - state batteries[J]. Angewandte Chemie International Edition: 2021, 60(12): 6718-6723.
[113] Chun H, Nam K, Hong S J, et al. Design of a Unique Anion Framework in Halospinel for Outstanding Performance of All Solid-state Li-ion Battery: First-principles Approach[J]. Journal of Materials Chemistry A: 2021:
[114] Zhang S, Zhao F, Wang S, et al. Advanced High - Voltage All - Solid - State Li - Ion Batteries Enabled by a Dual - Halogen Solid Electrolyte[J]. Advanced Energy Materials: 2021, 11(32): 2100836.
[115] Nolan A M, Zhu Y, He X, et al. Computation-accelerated design of materials and interfaces for all-solid-state lithium-ion batteries[J]. Joule: 2018, 2(10): 2016-2046.
[116] Zhu Y, He X, Mo Y. Origin of outstanding stability in the lithium solid electrolyte materials: insights from thermodynamic analyses based on first-principles calculations[J]. ACS applied materials & interfaces: 2015, 7(42): 23685-23693.
[117] Yang X, Jiang M, Gao X, et al. Determining the limiting factor of the electrochemical stability window for PEO-based solid polymer electrolytes: main chain or terminal–OH group?[J]. Energy & Environmental Science: 2020, 13(5): 1318-1325.
[118] Li X, Liang J, Yang X, et al. Progress and perspectives on halide lithium conductors for all-solid-state lithium batteries[J]. Energy & Environmental Science: 2020, 13(5): 1429-1461.
[119] Zahiri B, Patra A, Kiggins C, et al. Revealing the role of the cathode–electrolyte interface on solid-state batteries[J]. Nature Materials: 2021:
[120] Shaw D. The geochemistry of indium[J]. Geochimica et Cosmochimica Acta: 1952, 2(3): 185-206.
[121] Betz U, Olsson M K, Marthy J, et al. Thin films engineering of indium tin oxide: large area flat panel displays application[J]. Surface and Coatings Technology: 2006, 200(20-21): 5751-5759.
[122] Wadas T J, Wong E H, Weisman G R, et al. Coordinating radiometals of copper, gallium, indium, yttrium, and zirconium for PET and SPECT imaging of disease[J]. Chemical reviews: 2010, 110(5): 2858-2902.

[123] H. Nielsen R, H. Schlewitz J, Nielsen H, et al. Zirconium and zirconium compounds[J]. Kirk-Othmer Encyclopedia of Chemical Technology: 2000:
[124] Haynes W M, Lide D R, Bruno T. Abundance of Elements in the Earth's Crust and in the Sea[J]. CRC handbook of chemistry and physics: 2016, 97(2402): 14-17.
[125] Zhang C, Zhuang H, Qi Z, et al. The effect of defects for the ion transport of Li3ScCl6 and Li_3InCl_6 with the interface of lithium metal anode: A first-principles study[J]. Materials Today Communications: 2023, 35: 105764.
[126] Feng B, Ishikawa R, Kumamoto A, et al. Atomic scale origin of enhanced ionic conductivity at crystal defects[J]. Nano letters: 2019, 19(3): 2162-2168.
[127] Jianxing Z, Zongyu F, Jianhui S, et al. Crystal defects and phase transitions of nanocrystalline yttria-stabilised zirconia induced by high-energy ball milling[J]. Ceramics International: 2021, 47(12): 16432-16440.
[128] Di Noto V, Piga M, Negro E, et al. New hybrid inorganic-organic proton conducting membranes based on Nafion and a $[(ZrO_2)\cdot(Ta_2O_5)_{0.119}]$ oxide core-shell nanofiller[J]. MRS Online Proceedings Library (OPL): 2012, 1384: mrsf11-1384-b1311-1301.
[129] Di Noto V, Piga M, Giffin G A, et al. Interplay between mechanical, electrical, and thermal relaxations in nanocomposite proton conducting membranes based on nafion and a $[(ZrO_2)\cdot(Ta_2O_5)_{0.119}]$ core–shell nanofiller[J]. Journal of the American Chemical Society: 2012, 134(46): 19099-19107.
[130] Zheng X, Ge T, Wang R, et al. Performance study of composite silica gels with different pore sizes and different impregnating hygroscopic salts[J]. Chemical engineering science: 2014, 120: 1-9.
[131] Wang L, Li B, Shen M, et al. Corrosion resistance of steel materials in LiCl-KCl melts[J]. International Journal of Minerals, Metallurgy, and Materials: 2012, 19(10): 930-933.
[132] Shin H, Lee S, Jung H S, et al. Effect of ball size and powder loading on the milling efficiency of a laboratory-scale wet ball mill[J]. Ceramics International: 2013, 39(8): 8963-8968.
[133] Takacs L, McHenry J. Temperature of the milling balls in shaker and planetary mills[J]. Journal of materials science: 2006, 41: 5246-5249.
[134] Balakrishnan P, Ramesh R, Kumar T P. Safety mechanisms in lithium-ion batteries[J]. Journal of power sources: 2006, 155(2): 401-414.
[135] Kerman K, Luntz A, Viswanathan V, et al. Practical challenges hindering the development of solid state Li ion batteries[J]. Journal of The Electrochemical Society: 2017, 164(7): A1731.
[136] Verma P, Maire P, Novák P. A review of the features and analyses of the solid electrolyte interphase in Li-ion batteries[J]. Electrochimica Acta: 2010, 55(22): 6332-6341.
[137] Menzinger M, Wolfgang R. The meaning and use of the Arrhenius activation energy[J]. Angewandte Chemie International Edition in English: 1969, 8(6): 438-444.
[138] Li J V, Johnston S W, Yan Y, et al. Measuring temperature-dependent activation energy in thermally activated processes: A 2D Arrhenius plot method[J]. Review of scientific instruments: 2010, 81(3):
[139] Famprikis T, Canepa P, Dawson J A, et al. Fundamentals of inorganic solid-state electrolytes for batteries[J]. Nature materials: 2019, 18(12): 1278-1291.

[140] Gao J, Zhao Y-S, Shi S-Q, et al. Lithium-ion transport in inorganic solid state electrolyte[J]. Chinese Physics B: 2015, 25(1): 018211.
[141] Wolfenstine J. Rate-controlling species for creep of the solid state electrolyte: doped lanthanum gallate[J]. Solid State Ionics: 1999, 126(3-4): 293-298.
[142] Chen H-j, Cui Q, Tang Y, et al. Attapulgite based LiCl composite adsorbents for cooling and air conditioning applications[J]. Applied Thermal Engineering: 2008, 28(17-18): 2187-2193.
[143] Yang H, Zhao H, Dong H, et al. Preparation of In_2O_3 octahedrons by heating $InCl_3$ aqueous solution on the Si substrate[J]. Materials Research Bulletin: 2009, 44(5): 1148-1153.
[144] Das A, Shamirian A, Snee P T. Arsenic silylamide: An effective precursor for arsenide semiconductor nanocrystal synthesis[J]. Chemistry of Materials: 2016, 28(11): 4058-4064.
[145] Jalalian-Khakshour A, Phillips C, Jackson L, et al. Solid-state synthesis of NASICON ($Na_3Zr_2Si_2PO_{12}$) using nanoparticle precursors for optimisation of ionic conductivity[J]. Journal of materials science: 2020, 55(6): 2291-2302.
[146] Li X, Zhou Y, Tang J, et al. Optimizing $Li_{1.3}Al_{0.3}Ti_{1.7}(PO_4)_3$ Particle Sizes toward High Ionic Conductivity[J]. ACS Applied Materials & Interfaces: 2023, 15(30): 36289-36300.
[147] Froboese L, Van Der Sichel J F, Loellhoeffel T, et al. Effect of microstructure on the ionic conductivity of an all solid-state battery electrode[J]. Journal of The Electrochemical Society: 2019, 166(2): A318.
[148] Burmeister C F, Kwade A. Process engineering with planetary ball mills[J]. Chemical Society Reviews: 2013, 42(18): 7660-7667.
[149] Oleszak D, Shingu P H. Nanocrystalline metals prepared by low energy ball milling[J]. Journal of applied physics: 1996, 79(6): 2975-2980.
[150] Kamali N, Gniado K, McArdle P, et al. Application of ball milling for highly selective mechanochemical polymorph transformations[J]. Organic Process Research & Development: 2018, 22(7): 796-802.
[151] Gao X, Liu B, Hu B, et al. Solid-state lithium battery cathodes operating at low pressures[J]. Joule: 2022, 6(3): 636-646.
[152] Hikima K, Totani M, Obokata S, et al. Mechanical properties of sulfide-type solid electrolytes analyzed by indentation methods[J]. ACS Applied Energy Materials: 2022, 5(2): 2349-2355.
[153] Yan G, Malzbender J, Fu S, et al. Fracture behavior of solid electrolyte LATP material based on micro-pillar splitting method[J]. Journal of the European Ceramic Society: 2021, 41(10): 5240-5247.
[154] Ozdemir I, Ahrens S, Mücklich S, et al. Nanocrystalline Al–Al_2O_3p and SiCp composites produced by high-energy ball milling[J]. Journal of Materials Processing Technology: 2008, 205(1-3): 111-118.
[155] Zheng X, Fu E-D, Chen P, et al. Li_3InCl_6-coated $LiCoO_2$ for high-performance all solid-state batteries[J]. Applied Physics Letters: 2022, 121(3):
[156] Molaiyan P, Mailhiot S E, Voges K, et al. Investigation of the structure and ionic conductivity of a Li_3InCl_6 modified by dry room annealing for solid-state Li-ion battery applications[J]. Materials & Design: 2023, 227: 111690.

[157] Wang K, Ye Q, Zhang J, et al. Halide electrolyte Li_3InCl_6-based all-solid-state lithium batteries with slurry-coated $LiNi_{0.8}Co_{0.1}Mn_{0.1}O_2$ composite cathode: Effect of binders[J]. Frontiers in Materials: 2021, 8: 727617.
[158] Li W, Quirk J A, Li M, et al. Precise Tailoring of Lithium - Ion Transport for Ultralong - Cycling Dendrite - Free All - Solid - State Lithium Metal Batteries[J]. Advanced Materials: 2024, 36(13): 2302647.
[159] Luo X, Cai D, Wang X, et al. A novel ethanol-mediated synthesis of superionic halide electrolytes for high-voltage all-solid-state lithium–metal batteries[J]. ACS Applied Materials & Interfaces: 2022, 14(26): 29844-29855.
[160] Liu C, Miao C, He M, et al. Optimized layered ternary $LiNi_{0.5}Co_{0.2}Mn_{0.3}O_2$ cathode materials modified with ultrathin Li3InCl6 fast ion conductor layer for lithium-ion batteries[J]. Journal of Power Sources: 2023, 566: 232961.
[161] Deng Z, Jin Z, Chen D, et al. Bilayer halide electrolytes for all-inorganic solid-state lithium-metal batteries with excellent interfacial compatibility[J]. ACS Applied Materials & Interfaces: 2022, 14(43): 48619-48626.
[162] Xu J, Liu L, Yao N, et al. Liquid-involved synthesis and processing of sulfide-based solid electrolytes, electrodes, and all-solid-state batteries[J]. Materials Today Nano: 2019, 8: 100048.
[163] Wang C, Liang J, Luo J, et al. A universal wet-chemistry synthesis of solid-state halide electrolytes for all-solid-state lithium-metal batteries[J]. Science Advances: 2021, 7(37): eabh1896.
[164] Wang Y, Hoang B, Hoerauf J, et al. Hot and cold pressed LGPS solid electrolytes[J]. Journal of The Electrochemical Society: 2021, 168(1): 010533.
[165] Zhao E, Ma F, Guo Y, et al. Stable LATP/LAGP double-layer solid electrolyte prepared via a simple dry-pressing method for solid state lithium ion batteries[J]. RSC advances: 2016, 6(95): 92579-92585.
[166] Kotobuki M, Kanamura K, Sato Y, et al. Electrochemical properties of $Li_7La_3Zr_2O_{12}$ solid electrolyte prepared in argon atmosphere[J]. Journal of Power Sources: 2012, 199: 346-349.
[167] Wu X, Zhang L, Zhang X, et al. Ethyl cellulose nanodispersions as stabilizers for oil in water Pickering emulsions[J]. Scientific reports: 2017, 7(1): 1-10.
[168] Cao D, Li Q, Sun X, et al. Amphipathic Binder Integrating Ultrathin and Highly Ion - Conductive Sulfide Membrane for Cell - Level High - Energy - Density All - Solid - State Batteries[J]. Advanced Materials: 2021, 33(52): 2105505.
[169] Simon F J, Hanauer M, Richter F H, et al. Interphase formation of PEO20: LiTFSI–Li_6PS_5Cl composite electrolytes with lithium metal[J]. ACS Applied Materials & Interfaces: 2020, 12(10): 11713-11723.
[170] Duan Q, Wang S, Wang Q, et al. Simultaneous improvement on strength, modulus, and elongation of carbon nanotube films functionalized by hyperbranched polymers[J]. ACS applied materials & interfaces: 2019, 11(39): 36278-36285.
[171] Shen H, Yi E, Heywood S, et al. Scalable freeze-tape-casting fabrication and pore structure analysis of 3D LLZO solid-state electrolytes[J]. 2019, 12(3): 3494-3501.
[172] Lee C, Han S Y, Lewis J A, et al. Stack pressure measurements to probe the evolution of the lithium–solid-state electrolyte interface[J]. 2021, 6(9): 3261-3269.

[173] Zhu F, Islam M S, Zhou L, et al. Single-atom-layer traps in a solid electrolyte for lithium batteries[J]. 2020, 11(1): 1828.
[174] Hamann T, Zhang L, Gong Y, et al. The Effects of Constriction Factor and Geometric Tortuosity on Li - Ion Transport in Porous Solid - State Li - Ion Electrolytes[J]. Advanced Functional Materials: 2020, 30(14): 1910362.
[175] Wang X X, Chi X W, Li M L, et al. Metal–Organic Frameworks Derived Electrolytes Build Multiple Wetting Interfaces for Integrated Solid - State Lithium – Oxygen Battery[J]. Advanced Functional Materials: 2022: 2113235.
[176] Zhao H, Deng N, Kang W, et al. Highly multiscale structural Poly (vinylidene fluoridehexafluoropropylene)/poly-m-phenyleneisophthalamide separator with enhanced interface compatibility and uniform lithium-ion flux distribution for dendrite-proof lithium-metal batteries[J]. Energy Storage Materials: 2020, 26: 334-348.
[177] Elashmawi I. Effect of LiCl filler on the structure and morphology of PVDF films[J]. Materials Chemistry and Physics: 2008, 107(1): 96-100.
[178] Li N, Li X, Zhang T, et al. Host–guest composite materials of LiCl/NaY with wide range of humidity sensitivity[J]. Materials Letters: 2004, 58(10): 1535-1539.
[179] Trivedi M K, Branton A, Trivedi D, et al. Characterization of physicochemical and thermal properties of biofield treated ethyl cellulose and methyl cellulose[J]. International Journal of Biomedical Materials Research: 2015, 3(6): 83-91.
[180] Khichar K K, Dangi S B, Dhayal V, et al. Structural, optical, and surface morphological studies of ethyl cellulose/graphene oxide nanocomposites[J]. Polymer Composites: 2020, 41(7): 2792-2802.
[181] Briggs D, Beamson G. XPS studies of the oxygen 1s and 2s levels in a wide range of functional polymers[J]. Analytical chemistry: 1993, 65(11): 1517-1523.
[182] Chen X, Jia Z, Lv H, et al. Improved stability against moisture and lithium metal by doping F into Li_3InCl_6[J]. Journal of Power Sources: 2022, 545: 231939.
[183] Brown N M, Hewitt J A, Meenan B J. X-ray photoelectron spectroscopy and infra-red studies of X-ray-induced beam damage of cellulose, ethyl cellulose and ethyl-hydroxyethyl cellulose[J]. Surface and interface analysis: 1992, 18(3): 199-209.
[184] Shi J, Liu W, Jiang X, et al. Preparation of cellulose nanocrystal from tobacco-stem and its application in ethyl cellulose film as a reinforcing agent[J]. Cellulose: 2020, 27(3): 1393-1406.
[185] Sivkov D V, Petrova O V, Nekipelov S V, et al. Quantitative Characterization of Oxygen-Containing Groups on the Surface of Carbon Materials: XPS and NEXAFS Study[J]. Applied Sciences: 2022, 12(15): 7744.
[186] Pouya E S, Fatoorehchi H, Foroughi-Dahr M. Batch removal of Pb (II) ions from aqueous medium using gamma-Al2O3 nanoparticles/ethyl cellulose adsorbent fabricated via electrospinning method: An equilibrium isotherm and characterization study[J]. Polish Journal of Chemical Technology: 2018, 20(2):
[187] Naderi M. "Surface area: brunauer–emmett–teller (BET)," in *Progress in filtration and separation*: Elsevier, 2015, pp. 585-608.
[188] Wang Z, Tan R, Wang H, et al. A Metal–organic-framework-based electrolyte with nanowetted interfaces for high - energy - density solid - state lithium battery[J]. Advanced Materials: 2018, 30(2): 1704436.

[189] Hussain F, Zhu J, Xia H, et al. Theoretical Insights on the Comparison of Li-Ion Conductivity in Halide Superionic Conductors Li_3MCl_6, $Li2M_{2/3}Cl_4$, and $LiMCl_4$ (M= Y, Sc, Al, and Sm)[J]. The Journal of Physical Chemistry C: 2022, 126(31): 13105-13113.
[190] Li W, Liang J, Li M, et al. Unraveling the origin of moisture stability of halide solid-state electrolytes by in situ and operando synchrotron X-ray analytical techniques[J]. Chemistry of Materials: 2020, 32(16): 7019-7027.
[191] Pu X, Zhao D, Fu C, et al. Understanding and calibration of charge storage mechanism in cyclic voltammetry curves[J]. Angewandte Chemie International Edition: 2021, 60(39): 21310-21318.
[192] Kim T, Choi W, Shin H-C, et al. Applications of voltammetry in lithium ion battery research[J]. Journal of Electrochemical Science and Technology: 2020, 11(1): 14-25.
[193] Barai P, Higa K, Srinivasan V. Lithium dendrite growth mechanisms in polymer electrolytes and prevention strategies[J]. Physical Chemistry Chemical Physics: 2017, 19(31): 20493-20505.
[194] Quartarone E, Mustarelli P, Magistris A. PEO-based composite polymer electrolytes[J]. Solid State Ionics: 1998, 110(1-2): 1-14.
[195] Tan D H, Banerjee A, Chen Z, et al. From nanoscale interface characterization to sustainable energy storage using all-solid-state batteries[J]. Nature nanotechnology: 2020, 15(3): 170-180.
[196] Mei H-x, Piccardo P, Carraro G, et al. Thin-film Li_3InCl_6 electrolyte prepared by solution casting method for all-solid-state batteries[J]. Journal of Energy Storage: 2023, 72: 108244.
[197] Yang S, Liu Z, Liu Y, et al. Effect of molecular weight on conformational changes of PEO: an infrared spectroscopic analysis[J]. Journal of materials science: 2015, 50: 1544-1552.
[198] Epp J. "X-ray diffraction (XRD) techniques for materials characterization," in *Materials characterization using nondestructive evaluation (NDE) methods*: Elsevier, 2016, pp. 81-124.
[199] Pillai A M, Ghosh R, Dey A, et al. Crystalline and amorphous PEO based ceramic coatings on AA6061: Nanoindentation and corrosion studies[J]. Ceramics International: 2021, 47(10): 14707-14716.
[200] Appetecchi G, Henderson W, Villano P, et al. PEO-$LiN(SO_2CF_2CF_3)_2$ Polymer Electrolytes: I. XRD, DSC, and Ionic Conductivity Characterization[J]. Journal of the Electrochemical Society: 2001, 148(10): A1171.
[201] Muhammed D S, Brza M A, M. Nofal M, et al. Optical dielectric loss as a novel approach to specify the types of electron transition: XRD and UV-vis as a non-destructive techniques for structural and optical characterization of PEO based nanocomposites[J]. Materials: 2020, 13(13): 2979.
[202] Xue S, Teeters D, Crunkleton D W, et al. Ab initio calculations for crystalline PEO6: LiPF6 polymer electrolytes[J]. Computational Materials Science: 2019, 160: 173-179.
[203] Wang C, Yang Y, Liu X, et al. Suppression of lithium dendrite formation by using LAGP-PEO (LiTFSI) composite solid electrolyte and lithium metal anode modified by PEO (LiTFSI) in all-solid-state lithium batteries[J]. ACS applied materials & interfaces: 2017, 9(15): 13694-13702.

[204] Zagórski J, López del Amo J M, Cordill M J, et al. Garnet–polymer composite electrolytes: new insights on local Li-ion dynamics and electrodeposition stability with Li metal anodes[J]. ACS Applied Energy Materials: 2019, 2(3): 1734-1746.
[205] Zhou D, Zhang M, Sun F, et al. Performance and behavior of LLZO-based composite polymer electrolyte for lithium metal electrode with high capacity utilization[J]. Nano Energy: 2020, 77: 105196.
[206] Zhu L, Zhu P, Fang Q, et al. A novel solid PEO/LLTO-nanowires polymer composite electrolyte for solid-state lithium-ion battery[J]. Electrochimica Acta: 2018, 292: 718-726.
[207] Guo Q, Han Y, Wang H, et al. Flame retardant and stable $Li_{1.5}Al_{0.5}Ge_{1.5}$ \$(PO_4)_3$-supported ionic liquid gel polymer electrolytes for high safety rechargeable solid-state lithium metal batteries[J]. The Journal of Physical Chemistry C: 2018, 122(19): 10334-10342.
[208] Gorecki W, Jeannin M, Belorizky E, et al. Physical properties of solid polymer electrolyte PEO (LiTFSI) complexes[J]. Journal of Physics: Condensed Matter: 1995, 7(34): 6823.
[209] Przyłuski J, Such K, Wyciślik H, et al. PEO-based polymer blends as materials for solid electrolytes[J]. Synthetic metals: 1990, 35(1-2): 241-247.
[210] Reddy M J, Kumar J S, Rao U S, et al. Structural and ionic conductivity of PEO blend PEG solid polymer electrolyte[J]. Solid State Ionics: 2006, 177(3-4): 253-256.
[211] Li W, Quirk J A, Li M, et al. Precise Tailoring of Lithium-Ion Transport for Ultra-long-cycling Dendrite-free All-Solid-State Lithium Metal Batteries[J]. Advanced Materials: 2023: 2302647.
[212] Wu X, Whitacre J F. Reevaluating the stability of the PEO-based solid-state electrolytes for high voltage solid-state batteries[J]. Journal of Energy Storage: 2023, 63: 107052.
[213] Zhang Y, Feng W, Zhen Y, et al. Effects of lithium salts on PEO-based solid polymer electrolytes and their all-solid-state lithium-ion batteries[J]. Ionics: 2022, 28(6): 2751-2758.
[214] Nölle R, Beltrop K, Holtstiege F, et al. A reality check and tutorial on electrochemical characterization of battery cell materials: How to choose the appropriate cell setup[J]. Materials Today: 2020, 32: 131-146.
[215] Geise N R, Kasse R M, Nelson Weker J, et al. Quantification of efficiency in lithium metal negative electrodes via operando X-ray diffraction[J]. Chemistry of Materials: 2021, 33(18): 7537-7545.
[216] Martin L, Martinez H, Poinot D, et al. Comprehensive X-ray photoelectron spectroscopy study of the conversion reaction mechanism of CuO in lithiated thin film electrodes[J]. The Journal of Physical Chemistry C: 2013, 117(9): 4421-4430.
[217] Rjeb A, Letarte S, Tajounte L, et al. Polypropylene natural aging studied by X-ray photoelectron spectroscopy[J]. Journal of Electron Spectroscopy and Related Phenomena: 2000, 107(3): 221-230.
[218] Tatara R, Karayaylali P, Yu Y, et al. The effect of electrode-electrolyte interface on the electrochemical impedance spectra for positive electrode in Li-ion battery[J]. Journal of The Electrochemical Society: 2019, 166(3): A5090-A5098.

[219] Cao D, Sun X, Li Q, et al. Lithium dendrite in all-solid-state batteries: growth mechanisms, suppression strategies, and characterizations[J]. Matter: 2020, 3(1): 57-94.
[220] Ji X, Hou S, Wang P, et al. Solid - state electrolyte design for lithium dendrite suppression[J]. Advanced Materials: 2020, 32(46): 2002741.